The Past, Present, and Groundbreaking Future of OH Megamasers

by

Hayley Roberts

B.S., Illinois Wesleyan University, 2016

M.S., University of Colorado, 2018

A thesis submitted to the
Faculty of the Graduate School of the
University of Colorado in partial fulfillment
of the requirements for the degree of
Doctor of Philosophy
Department of Astrophysical & Planetary Sciences
2023

Committee Members:
Jeremy Darling, Chair
Julie Comerford
Meredith MacGregor
Andrew J. Baker
Zachory Berta-Thompson

Roberts, Hayley (Ph.D., Astrophysics)

The Past, Present, and Groundbreaking Future of OH Megamasers

Thesis directed by Prof. Jeremy Darling

OH megamasers (OHMs) are luminous masers found in (ultra-)luminous infrared galaxies ([U]LIRGs). OHMs are signposts of major gas-rich mergers associated with some of the most extreme star forming regions in our universe. In the four decades since their discovery, only 120 OHM hosts have been detected at limited redshifts despite numerous searches in an order of magnitude more galaxies. However, the dominant OH masing line, occurring at 1667 MHz, can spoof the 1420 MHz neutral hydrogen (H I) line in untargeted surveys. H I surveys on next-generation radio telescopes, such as the Square Kilometre Array (SKA) and its precursors, will detect unprecedented numbers of OHMs. This surge in detections will not only fundamentally change the landscape of the known OHM population, but will also unlock our ability to implement OHMs as tracers of major mergers and extreme star formation on cosmic scales. Here, I present predictions for the number of OHMs that will be detected by these surveys, as well as novel methods for identifying these interlopers using a k-Nearest Neighbors machine learning algorithm. Preliminary data from H I surveys on precursor SKA telescopes is used to vet and strengthen these methods, resulting in five new OHM detections of sources originally classified as H I emission. I also present two new OHM detections from SKA precursors that showcase this upcoming revolutionary science – whether it be high quality measurements of the OH masing lines or shattering the record for highest redshift OHM detection. I also reexamine the underlying conditions required to steer a major merger on the path to producing an OHM, demonstrating that our previous theories are too simplistic to describe the full population of OHMs hosts. Lastly, I present a comprehensive catalog of all known OHMs and their host galaxies, including their IR and radio properties. This catalog and the inspection of relations between OHMs and their hosts serve as a consolidated, unified resource in the era of new OHM detections.

Acknowledgements

Many, many people were involved in either making this work possible or supporting me along the way. First, I am endlessly grateful for the unwavering support and phenomenal mentorship from my advisor, Jeremy Darling, who allowed me to chase down all my side project ideas while providing the necessary guidance to make sure I never strayed too far. Additionally, I would like to thank my colleagues and collaborators who have gone above and beyond to share their ideas, data, and research while providing feedback on mine. I am excited to continue finding fun things together.

I'd also like to thank my friends and family who not only tolerated me during the writing of this thesis but throughout graduate school. If I wasn't required to keep this under one page, I could fill another thesis with all the shared moments and memories over the years that have been endlessly important to me. I am forever grateful for the joy, sanity, and support I've received. Without an ounce of exaggeration, I could not have done it without you all.

Finally, thank you to Travis. You are unfailingly patient, selfless, and supportive. To borrow a line from my vows, I am able to chase my dreams with the type of confidence that could only come from someone whose partner does the heavy lifting to make it all possible. From always making sure I've eaten an actual meal to brewing a fresh pot of coffee for each of the countless nights of observing, thank you for it all.

Contents

Chapter

Appendix

Tables

Table

Figures

Figure

Chapter 1

Introduction

Preface

My thesis work is focused on many aspects of OH megamasers (OHMs) and their host galaxies. This introductory chapter provides the necessary background and motivations for this work. In section 1.1, I introduce OHMs including a brief summary of their underlying physics and astrophysical context. Section 1.2 presents a history of previous searches for OHM hosts and a potential future of discovery using H I surveys. Lastly, I discuss the motivation behind finding OHMs and present an overview of the work presented in this dissertation in Section 1.3.

Like many works before this one, the summary of masers presented here benefited greatly from reviews by Lonsdale (2002), Lo (2005), and Darling (2005), as well as the textbooks by Elitzur (1992) and Gray (2012). These resources are invaluable and highly recommended if the reader seeks further reading.

1.1 An Introduction to OH Megamasers

1.1.1 A Brief History of Space Lasers

The term maser,[1] an acronym that means "microwave amplification by stimulated emission of radiation," was first used to describe a laboratory-built device that produced coherent radiation via stimulated emission (Gordon et al. 1955). Only a decade later, the first astrophysical maser

---

[1] Curiously, the term "maser" was coined *before* "laser," despite the former being almost completely omitted from popular usage (Schawlow & Townes 1958; Taylor 2007).

was detected in the Orion molecular cloud complex. The source and anomalous nature of the emission initially defied explanation, earning the label "mysterium" in Weaver et al. (1965). Follow-up observations (Weinreb et al. 1965) and theoretical modeling (Litvak et al. 1966; Perkins et al. 1966) suggested that this "mysterium" is actually maser-amplified OH (hydroxyl radical) emission. As noted in Elitzur (1992), Weaver commented years later, "I often wondered whether anyone could have come up with the right explanation had masers not been constructed in the laboratory a few years earlier."

Although galactic OH masers in star-forming regions were the first to be discovered, in the intervening years numerous other maser-producing molecules have been detected in a variety of contexts. These molecules include water (H_2O; Cheung et al. 1969), methanol (CH_3OH; Ball et al. 1970), silicon monoxide (SiO; Snyder & Buhl 1974), ammonia (NH_3; Mauersberger et al. 1986), carbon monosulfide (CS; Ginsburg et al. 2019) and more. Masers have been found within our own galaxy in various contexts such as stellar atmospheres, comets, supernovae, and planetary systems (see Chapter 6 of Gray 2012).

The first extragalactic OH maser emission was discovered in the nucleus of NGC 253 by Whiteoak & Gardner (1974). However, Baan et al. (1982) detected unparalleled extragalactic OH maser emission in Arp 220, a nearby merging system. This detection was dubbed a *mega*maser because the emission from this source is $\sim 10^6$ more luminous than their galactic counterparts with isotropic luminosities of $L_{\rm OH} > 10^1 L_\odot$. Following this came the detection of water (H_2O; Churchwell et al. 1977), formaldehyde (H_2CO; Baan et al. 1986), and methine (CH; Whiteoak et al. 1980) extragalactic megamasers (Baan 1993).

It was not even a century ago that the first detection of molecules in space was made (McKellar 1940), let alone found to be masing. These maser discoveries are rich in science – each deserving a much more careful treatment and explanation than can be offered in a thesis that only examines OH megamasers. As such, the textbooks mentioned in the preface (Elitzur 1992; Gray 2012) and the references within are phenomenal resources for fully exploring astrophysical masers.

In the next sections, I will discuss the necessary conditions for producing astrophysical masers, first for all masers and then for specific underlying physics of OH megamasers. As a note, throughout this work, the term OH megamaser (OHM) *only* refers to the powerful extragalactic masers.

1.1.2 Conditions for Astrophysical Maser Action

At the simplest level, the requirements for producing an astrophysical maser are population inversion sustained via some pumping mechanism and a masing medium to produce a large enough gain for detection. Population inversion occurs when there are more molecules in an excited state than in a lower energy state. This is contrary to what is seen in thermodynamic equilibrium where the level populations approach a Boltzmann distribution:

$$\frac{N_u}{N_l} = \frac{g_u}{g_l} e^{-\Delta E / k_B T_x}, \tag{1.1}$$

where N_u is the population of the upper level, N_l is the population of the lower level, g are the corresponding degeneracies for each level, ΔE is the energy difference between two states, k_B is the Boltzmann constant, and T_x is the excitation temperature (Elitzur 1992). Equation 1.1 will always be less than one for positive excitation temperatures, meaning the lower energy level will be more populated than the higher energy level ($N_u/N_l < 1$).

To produce an inverted population ($N_u/N_l < 1$), there must be a mechanism that excites these molecules to higher levels as systems tend to populate ground states – this is called the pump. Pumping mechanisms are classified as collisional, chemical or radiative. Both of these scenarios require spontaneous emission or an external source that radiates at the same energy as the maser transition to produce the stimulated emission, leading to amplification of radiation. This masing action can only occur in low density (at least when compared to terrestrial conditions) environments.

Now consider the relationship between the absorption coefficient (α_ν) in radiative transfer and population levels,

$$\alpha_\nu \propto \frac{\Delta E}{4\pi} \left(1 - \frac{N_u}{N_l} \right), \tag{1.2}$$

simplified from Rybicki & Lightman (1979). This coefficient usually represents the radiation attenuation, where higher absorption coefficient values represent more attenuation. However, for inverted populations ($N_u/N_l < 1$), this coefficient actually becomes negative, which means that the radiation is *amplified.* The degree of amplification is based on the path length, L, through the medium, which will increase the intensity by a factor of $\exp(-\alpha_\nu \mathrm{d}L)$. On astronomical scales and with this amplification factor, reaching the necessary velocity-coherent path lengths to detect maser emission becomes, perhaps, not as difficult as initially thought.

This very generic overview applies to all masers discussed in the previous section and a much more detailed formulation can be found in Elitzur (1992) and Willett (2011). However, the exact details that allow for these conditions to occur vary for each molecule and scenario. In the next section, I discuss the masing levels and the physical context that allows for this masing action for OHMs.

1.1.3 OH Maser Action

OH is a diatomic molecule that has surprisingly complicated energy levels. This is due to it being a radical (i.e. having an unfilled electron shell) and containing a hydrogen atom whose nuclear spin can couple to unpaired electrons. In spectroscopic notation ($^{2\mathrm{s}+1}\Lambda_\Omega$), the unpaired electron yields an angular orbital momentum of one, resulting in a Π configuration, and has a spin of $s = 1/2$, corresponding to a notation of $^2\Pi$. The projected total electron angular momentum is the vector sum of these two quantities, resulting in two possible values, $\Omega = 1 \pm 1/2 = 1/2, 3/2$. This spin-orbit coupling results in two rotational energy ladders, as shown in Figure 1.1 from Lockett & Elitzur (2008). Each ladder is split into energy levels of $J = N + \Omega$ where N is the angular momentum quantum number $N = 1, 2, 3, ...$, where J is the total angular momentum, beginning with the ground state in either ladder. These energy levels are further split from Λ-doubling, a weak coupling of the electronic angular momentum to the rotation of the molecule. This results in each energy level being split into odd ($-$) and even ($+$) parity. The final perturbation comes from hyperfine splitting (F) due to angular-momentum coupling between the spin of the unpaired electron and the spin of the proton in the hydrogen nucleus. This is calculated as the vector sum between the angular momentum (J) and the nuclear spin ($I = 1/2$), which splits each Λ-doubled level once more.[2]

Figure 1.1 shows the lowest 24 energy levels as described above. Allowed transitions for these levels follow the typical dipole selection rules. This requires a parity change and $\Delta F = 0, \pm 1$ (excluding the forbidden $F = 0 \rightarrow 0$). These transitions are shown for the four lowest levels in Figure 1.1 as vertical lines between levels. There are two main lines at 1665 and 1667 MHz (F-conserving) and two satellite lines at 1612 and 1720 MHz (F-changing). While all four of these lines can potentially produce masers, rarely are they all found in observations, suggesting a complicated pumping process. In local thermodynamic equilibrium (LTE), the line strengths are 1:5:9:1 for the 1612, 1665, 1667, and 1720 MHz lines, respectively. The implicit requirement that masers *not* be in LTE results in strong variations of observed line strengths from these values.

1.1.4 Properties of OH Megamaser Emission and Their Hosts

OHMs produce isotropic line luminosities of $L_{\mathrm{OH}} \geq 10\,L_{\odot}$ with line widths ranging from 10 to 1000 $\mathrm{km\,s^{-1}}$. Those with line luminosities of $L_{\mathrm{OH}} \geq 10^4\,L_{\odot}$ are referred to as OH *giga*masers but the distinction is arbitrary. The most luminous OHM discovered to date has an OH luminosity of $L_{\mathrm{OH}} = 10^{4.2}\,L_{\odot}$ (Darling & Giovanelli 2001). On the other end, sources with line luminosities of $L_{\mathrm{OH}} < 10^1\,L_{\odot}$ are referred to as OH *kilo*masers and these are thought to be a distinct population from OHMs with potentially differing underlying processes. Some examples of OHM emission from Darling & Giovanelli (2002a) are shown in Figure 1.2. Often, only the 1667 MHz line is detected in OHMs. While some detections have been made of the 1665 MHz line, the broad line widths in these systems often make this detection impossible. Detection of the 1612 and 1720 MHz satellite lines in OHMs is extremely rare, having only been detected in six OHMs (McBride et al. 2013; Hess et al. 2021).

As a note, throughout this work and the literature as well, all quoted OH luminosities are assumed to be isotropic – i.e. the luminosity is distributed uniformly in all directions, and there

---

[2] Omitted from this summary is the additional complications from Zeeman splitting; however, a formulation of this is presented in Section 5.5.3 of Gray (2012) if the reader wants further reading.

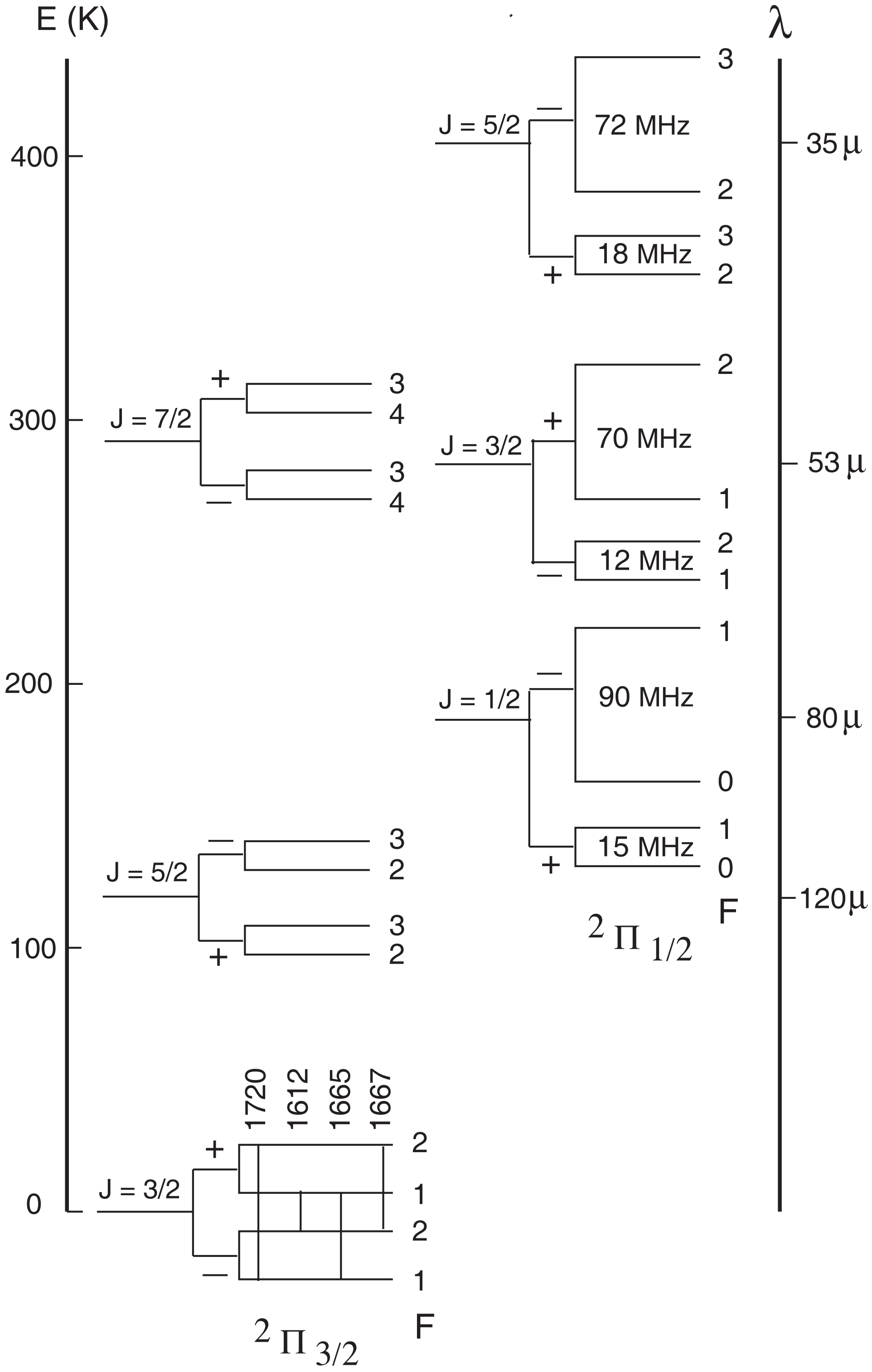

Figure 1.1 Diagram of the lowest 24 hyperfine OH energy levels from Lockett & Elitzur (2008). Relative sizes of the energy level splittings are not to scale.

is no preferential direction for the emission of radiation. This is certainly not the case for OHMs, for reasons discussed further below. However, it is not possible to determine the total luminosity accounting for the geometry and beaming of the masing region without making multiple detailed assumptions. Therefore, assuming an apparent isotropic luminosity allows for easier comparison of many OHMs and is a useful quantity for comparing the relative strengths of different sources.

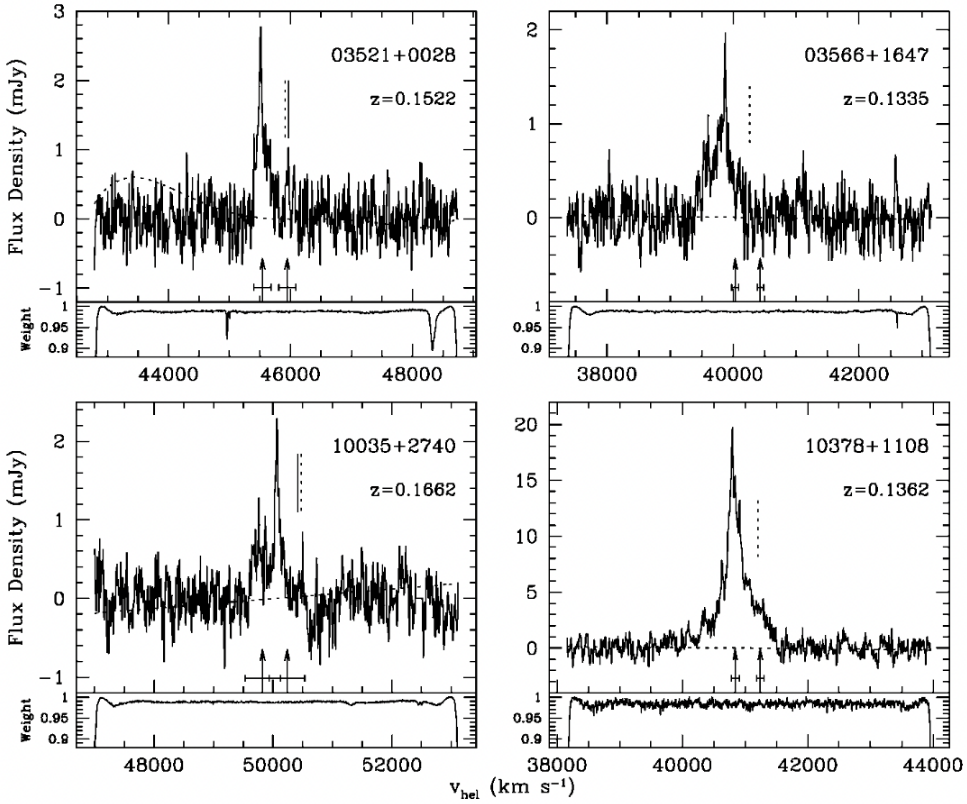

Figure 1.2 Examples of OH emission in four OHMs found in Darling & Giovanelli (2002a). Arrows indicate the expected velocity of the 1667 MHz (left) and 1665 MHz (right) lines based on the optical redshift.

The standard OHM model has undergone many revisions in the four decades since their initial discovery. Current OH maser models show that OH maser emission is a combination of both compact, saturated and diffuse, unsaturated regions (Diamond et al. 1999; Darling & Giovanelli 2002a). This combination of emissions is achieved via multiple parsec-scale clouds with high velocity dispersions ($\sim$20 $\mathrm{km\,s^{-1}}$) that are distributed within a ring structure with a radius on the order of $\sim$tens of parsecs, as demonstrated through VLBI observations (Pihlström et al. 2001) and modeling

(Parra et al. 2005). The overall structure of this region is the source of the diffuse emission and the compact bright emission is realized through overlapping clouds. The main masing lines are pumped by intense far-infrared (IR) radiation, primarily via 53 and 35 μm transitions (Lockett & Elitzur 2008).

OHMs have been found exclusively in the nuclear regions of (ultra-)luminous infrared galaxies ([U]LIRGs), which are defined as having IR luminosities of $L_{\rm IR} \geq 10^{11} L_\odot$ for LIRGs and $L_{\rm IR} \geq 10^{12} L_\odot$ for ULIRGs (Sanders & Mirabel 1996). The primary source of IR radiation in (U)LIRGs is dust heated by star formation and/or active galactic nuclei (AGN) triggered by a major galaxy merger. This is thought to be the source of the strong far-IR radiation required to pump OHMs. Despite this, only ∼20% of galaxies selected by their IR colors actually host OHMs (Darling & Giovanelli 2002a; Lo 2005). Further, while 50-95% of non-masing (U)LIRGs host AGN, only 10-25% of OHM hosts indicate AGN activity (Willett et al. 2011a). The distinction between masing and non-masing (U)LIRGs is still an open question, but primary theories pinpoint the dense molecular gas content of the host galaxies as the delineator. By comparing dense gas fractions ($L_{\rm HCN}/L_{\rm CO}$, where HCN traces *dense* gas and CO traces *total* gas) in masing and non-masing (U)LIRGs, Darling (2007) shows that those hosting masers have markedly higher dense gas fractions.

1.2 The Search for OH Megamasers

In the 40 years since their discovery, only 120 OHM hosts have been discovered (Section 6) with the longstanding record holder for highest redshift (IRAS 14070+0525) being discovered by Baan et al. (1992a) at a redshift of $z = 0.265$. This redshift limit has been surprisingly steadfast. Since OHMs are produced by major galaxy mergers which become more common at higher redshifts up to a redshift of $z \sim 2$, the expectation is that OHMs should also become more common but this has not yet been realized in observations. Despite their extreme nature, the criteria necessary for consistently identifying OHM host galaxies has eluded those hunting for new OHMs, resulting in searches being plagued by low detection rates (e.g., Staveley-Smith et al. 1987; Dickey et al. 1990; Baan et al. 1992b; Darling & Giovanelli 2000, 2001, 2002a; Willett 2012; Suess et al. 2016; Roberts

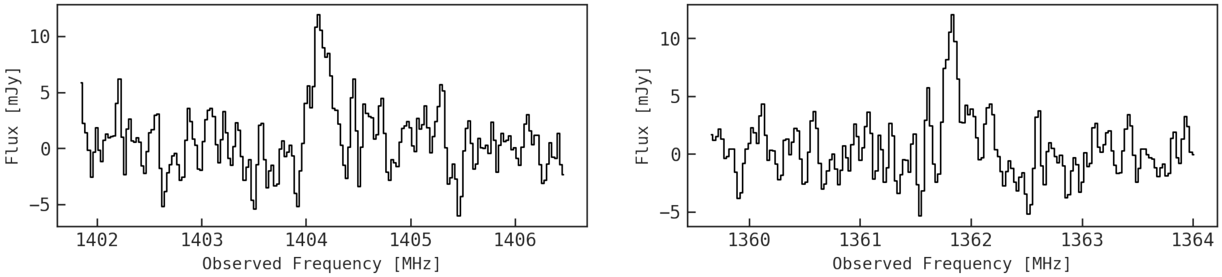

Figure 1.3 Example spectra of OH and H I sources – the left panel shows an OH masing line from an OHM host ($\nu_{\mathrm{OH,rest}} = 1667$ MHz, $z = 0.188$) and the right panel shows an H I emission line from a non-masing starforming galaxy ($\nu_{\mathrm{HI,rest}} = 1420$ MHz, $z = 0.043$).

et al. in prep.). Significant efforts have been made to isolate the conditions or properties that can be used to identify OHM host galaxies. However, in a way somewhat reminiscent of the search for dark matter, more has been understood about what is *not* associated with OHMs than with what is associated with them. While OH luminosity (L_{OH}) shows good correlation with IR luminosity (L_{IR}), ∼80% of (U)LIRGs show no OHM activity (Darling & Giovanelli 2002a; Lo 2005). While 50-95% of non-masing (U)LIRGs show evidence of active galactic nuclei (AGN), only 10-20% of OHMs indicate AGN activity (Willett et al. 2011b). When it seemed that OHMs may be a distinct class of (U)LIRGs, no optical nuclear distinction could be found between masing and non-masing (U)LIRGs (Darling & Giovanelli 2006). Existing OHMs have been extensively studied and there are still no clear markers of what conditions spur masing action nor what separates masing from non-masing (U)LIRGs.

Although targeted searches of OHMs have not proven to be fruitful, current and upcoming H I surveys on next-generation radio telescopes will usher in a new era of serendipitous OHM detections. First predicted by Briggs (1998), the 18 cm masing line from an OHM at z_{OH} can “spoof” the 21 cm H I emission line at a different redshift, z_{HI}, if $\nu_{\mathrm{HI}}/(1 + z_{\mathrm{HI}}) = \nu_{\mathrm{OH}}/(1 + z_{\mathrm{OH}})$ where $\nu_{\mathrm{HI}} = 1420.4$ MHz and $\nu_{\mathrm{OH}} = 1667.4$ MHz. The OH and H I emission lines have similar linewidths in their respective environments: H I in spiral galaxies and OH in major galaxy mergers. For many sources, distinguishing between these lines requires an independent measurement of the galaxy’s spectroscopic redshift to determine the rest wavelength for an observed emission line,

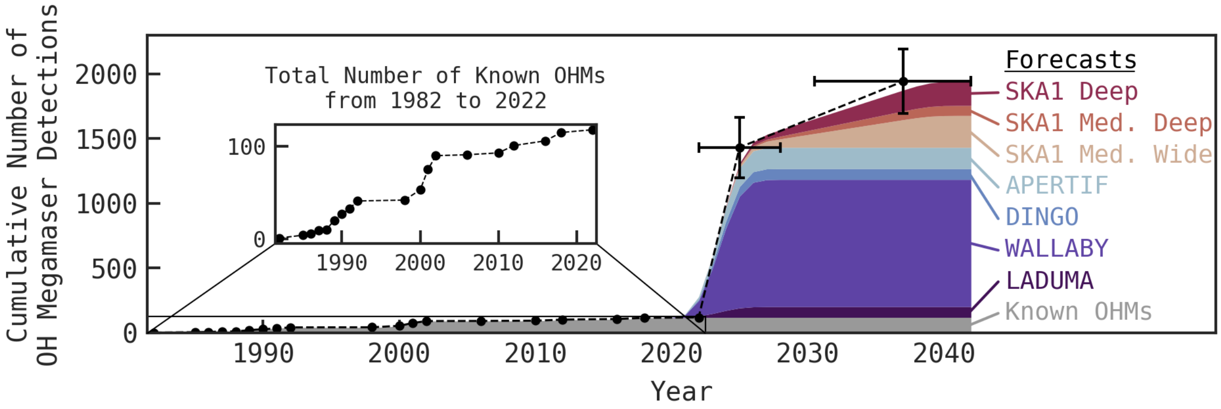

Figure 1.4 The cumulative number of OHMs detected up to 2023 and forecasts, broken down by current and upcoming H I survey contributions. The two markers with error bars are using projections from Roberts et al. (2021) (also in Chapter 2) and the errors in year are estimated using projected dates of survey completion considering typical telescope delays, particularly in the case of the SKA1, whose first light was recently predicted to be in 2027.

as demonstrated in Figure 1.3. Since OHMs are created by major mergers, they are relatively uncommon at low redshifts. However, we are on the cusp of the next generation of H I surveys that will observe out to $z \sim 2$, such as those on the first phase of the Square Kilometre Array (SKA) and its precursors. With the increase of redshift comes an increase of mergers and subsequently OHMs. Briggs (1998) predicts that by $z \sim 1$, 50% of objects observed by H I surveys will be OHM hosts. This method of detecting OHMs offers a promising way of expanding our sample of known sources and is discussed at length in Chapter 2, which includes predictions for the number of new detections that will be discovered. This is demonstrated in Figure 1.4, which shown the number of OHMs that have been discovered by year (black line) in comparison to the forecasted detections with these H I surveys. Chapter 4 presents two detections of OHMs from next-generation H I surveys that demonstrate just how powerful these new detections will be, including the first OHM to break the record for highest redshift in *thirty years*.

1.3 Overview of This Dissertation

In this chapter, I presented a concise summary of 40 years of OHM discovery and science. However, this is just a small preview of the science these unique sources can offer. The OHM emission line is detectable at cosmic distances, making these sources powerful tracers of extreme star formation (Lockett & Elitzur 2008), high molecular gas density (Willett et al. 2011a), and strong far-IR radiation (Baan et al. 1989). Though currently rare and known only at limited redshifts, understanding these sources will eventually allow us to study what role these properties play in galaxy evolution, particularly star formation feedback and black hole accretion. OHMs have been used as in-situ magnetometers via observations of Zeeman splitting (Robishaw et al. 2008; McBride et al. 2014). Further, as OHMs are found in late-stage major galaxy mergers, they can independently constrain the major merger rate (Chapter 2). Their extraordinary properties and correlation with galaxy mergers make OHMs an invaluable tool for understanding galaxy evolution. The goal of the rest of this thesis is to lay the necessary groundwork to realize this future of OHM science.

As implied by the title of this thesis, the work presented in this dissertation covers a broad timescale, spanning the early days of OHM discovery to a future of unprecedented detection rates. In Chapter 2, I present forecasts for the number of OHMs that will be found during this era of discovery and methods for uncovering them in H I surveys. These methods are tested, updated, and used to identify five new OHMs in Chapter 3. Chapter 4 highlights two recent OHM detections that showcase the types of discoveries that will soon become common occurrence. In preparation for this future of discovery, Chapter 5 reconsiders what distinguishes OHM hosts from non-masing (U)LIRGs and demonstrates that the dense gas hypothesis is incomplete. Chapter 6 presents a compiled catalog of all known OHMs and reexamines some commonly cited relationships between OHMs and their host galaxies. Finally, Chapter 7 summarizes the work presented in this thesis.

Chapter 2

OH Megamasers in H I Surveys: Forecasts and a Machine Learning Approach to Separating Disks from Mergers

Abstract

OH megamasers (OHMs) are rare, luminous masers found in gas-rich major galaxy mergers. In untargeted neutral hydrogen (H I) emission-line surveys, spectroscopic redshifts are necessary to differentiate the $\lambda_{\text{rest}} = 18$ cm masing lines produced by OHMs from H I 21 cm lines. Next generation H I surveys will detect an unprecedented number of galaxies, most of which will not have spectroscopic redshifts. We present predictions for the numbers of OHMs that will be detected and the potential "contamination" they will impose on H I surveys. We examine Looking at the Distant Universe with the MeerKAT Array (LADUMA), a single-pointing deep-field survey reaching redshift $z_{\text{HI}} = 1.45$, as well as potential future surveys with the Square Kilometre Array (SKA) that would observe large portions of the sky out to redshift $z_{\text{HI}} = 1.37$. We predict that LADUMA will potentially double the number of known OHMs, creating an expected contamination of 1.0% of the survey's H I sample. Future SKA H I surveys are expected to see up to 7.2% OH contamination. To mitigate this contamination, we present methods to distinguish H I and OHM host populations without spectroscopic redshifts using near- to mid-IR photometry and a k-Nearest Neighbors algorithm. Using our methods, nearly 99% of OHMs out to redshift $z_{\text{OH}} \sim 1.0$ can be correctly identified. At redshifts out to $z_{\text{OH}} \sim 2.0$, 97% of OHMs can be identified. The discovery of these high-redshift OHMs will be valuable for understanding the connection between extreme star formation and galaxy evolution.

This chapter was originally published as a paper in the April 2021 issue of *The Astrophysical Journal* (Volume 911, Issue 1, id.38), and is reproduced here.

2.1 Introduction

OH megamasers (OHMs) are luminous 18 cm masers found in (ultra-)luminous infrared galaxies ([U]LIRGs) produced predominantly by major galaxy mergers. The dominant masing lines occur at 1667 and 1665 MHz in the ground state of OH. These masing lines have isotropic luminosities between $10^1 - 10^4 L_\odot$ and line widths ranging from 10 to 1000 km s^{-1} due to Doppler broadening (Darling 2005). This rare phenomenon has only been discovered in roughly 110 galaxies out to redshift $z = 0.264$ (Darling & Giovanelli 2002b).

OHMs are associated with high molecular gas density, $n(\mathrm{H_2}) \sim 10^4$ cm^{-3}, and strong far-IR radiation, making them markers for some of the most extreme star formation observed in our local universe (Darling 2007; Lockett & Elitzur 2008). These galaxies can provide significant information about how extreme star formation relates to galaxy evolution, particularly once discovered at higher redshifts. As products of gas-rich major mergers, OHMs can also provide an independent measure of the galaxy merger rate at a specific evolutionary stage. Further, the masing lines present in OHMs can be utilized as Zeeman magnetometers, providing in-situ measurements of magnetic fields in nearby galaxies (Robishaw et al. 2008; McBride et al. 2014). OHMs are useful astronomical tools for understanding many aspects of galaxy evolution.

However, in untargeted emission-line surveys for neutral hydrogen (H I), an OH emission line at z_{OH} can "spoof" a 21 cm H I line at z_{HI} if $\nu_{\mathrm{HI}}/(1 + z_{\mathrm{HI}}) = \nu_{\mathrm{OH}}/(1 + z_{\mathrm{OH}})$ (Briggs 1998) where $\nu_{\mathrm{HI}} = 1420.4$ MHz and $\nu_{\mathrm{OH}} = 1667.4$ MHz. For example, restframe H I corresponds to OH at a redshift of $z_{\mathrm{OH}} = 0.174$, while H I at redshift $z_{\mathrm{HI}} = 0.1$ would correspond to OH at a redshift of $z_{\mathrm{OH}} = 0.291$. These two lines have similar linewidths in their respective environments: H I in spiral galaxies and OH in major galaxy mergers. Distinguishing between these lines often requires knowledge of a galaxy's spectroscopic redshift to determine the rest wavelength for an observed emission line (e.g., Hess et al. 2021). For galaxies that do not have spectroscopic redshifts, disentangling H I from OH is not straightforward. This ambiguity particularly becomes a problem for high-redshift untargeted line surveys, which will not have prior spectroscopic redshifts for many of their detected galaxies.

Despite the versatility and capacity of OHMs to serve as tools for studying galaxy evolution, line confusion in H I surveys can serve as a source of contamination for the survey's main goals. Nonetheless, next-generation H I surveys, such as those with the Square Kilometre Array (SKA) and its precursors, will be able to detect many new OHMs at redshifts never before reached. Finding these unique galaxies in the pool of H I disk detections will enable an exciting new era in OHM science.

LADUMA (Looking at the Distant Universe with MeerKAT Array; Blyth et al. 2016) is a survey with the MeerKAT radio interferometer, a precursor instrument for the SKA, that will be susceptible to OH/H I confusion. LADUMA will be the deepest neutral hydrogen survey to date and is expected to detect H I out to redshifts $z_{\mathrm{HI}} = 1.45$. LADUMA's main science goals are related to studying the neutral atomic gas content of galaxies, meaning that OHM detections will contaminate its H I samples. At low redshift, spectroscopic redshifts are generally known, so the contamination rate should be small. At greater distances where fewer spectroscopic redshifts are currently known and OHM prevalence increases due to the elevated merger rate, the contamination rate threatens to be higher.

This paper presents predictions for the numbers of OH megamasers that will be detected by LADUMA in Section 2.2 and by other H I surveys in Section 2.3. We then present methods for distinguishing OH from H I in LADUMA and other untargeted line surveys using near- to mid-IR photometry in Section 2.4. We discuss these results and their limitations in Section 2.5 and summarize our conclusions in Section 2.6. Throughout this work, we assume a flat ΛCDM cosmology with $H_0 = 70$ km s^{-1} Mpc^{-1}, $\Omega_m = 0.3$, and $\Omega_\Lambda = 0.7$.

2.2 OH Megamasers in LADUMA

In this section, we present our predictions for the number of OHMs that will be detected in LADUMA. A few inputs are needed to enable these predictions: an OH luminosity function, the volume of the survey, and the galaxy merger rate. The following subections will cover each of these. We then make use of this information to predict the number of OH megamasers and the resultant OHM contamination rate in other H I surveys.

2.2.1 The OH Luminosity Function

To create a prediction for the number of OHMs that will be found in the LADUMA survey, we need to integrate the OH luminosity function (OHLF) over the volume and luminosity limits of LADUMA. The OHLF presented in Darling & Giovanelli (2002a) was constructed from OHMs detected by Arecibo and is valid for $2.2 < \log(L_{\rm OH}/L_\odot) < 3.8$ and $0.1 < z_{\rm OH} < 0.23$. An obvious source of uncertainty is the extrapolation of the OHLF to cover redshifts out to $z_{\rm OH} = 1.876$ and luminosities as low as $1L_\odot$ for the LADUMA survey.

The OHLF is defined as the number of OHMs with luminosity ($L_{\rm OH}$) per unit comoving volume (Mpc^3) per logarithmic interval in $L_{\rm OH}$, and can be parameterized as

$$\Phi(L_{\rm OH}) = b\, L_{\rm OH}^{a}. \tag{2.1}$$

The values of a and b presented in Darling & Giovanelli (2002a) were determined using an error-weighted least-squares fit. We use a Markov chain Monte Carlo (MCMC) method to refit the OHLF using the data presented in Darling & Giovanelli (2002a) to account for the correlations between fit parameters. We use *emcee*, a Python package for implementing MCMC (Foreman-Mackey et al. 2013). The refit OHLF is

$$\Phi(L_{\rm OH}) = (3.17 \pm 0.58) \times 10^{-6}\ (L_{\rm OH}/L_\odot)^{-0.50\pm0.13}\mathrm{Mpc}^{-3}\ \mathrm{dex}^{-1}. \tag{2.2}$$

The samples from the MCMC allow us to create a representative sample of possible OHLF parameters for predictions of the number of OH megamasers that will be observed. This is the OHLF that will be used throughout this work. We later compare how the difference between the two OHLFs changes the number of OHMs predicted to be detected.

2.2.2 Volume of LADUMA Field

LADUMA will be observing an area encompassing the Extended Chandra Deep Field South (E-CDFS), covering 0.9 deg^2 at $z = 0$. The field of view of MeerKAT will increase with redshift due to the array's larger primary beam at lower frequencies. The total volume of the field can be calculated starting with the equation for comoving volume (equation 28 from Hogg 1999) shown in equation (2.3), where $E(z) = \sqrt{\Omega_M(1+z)^3 + \Omega_\Lambda}$, $D_H = c/H_0$, and D_A is the angular diameter distance:

$$dV_c = D_H \frac{(1+z)^2 D_A^2}{E(z)}\, d\Omega\, dz. \tag{2.3}$$

To account for an increasing field of view at higher redshifts, we write $d\Omega$ in equation (2.3) in terms of the redshift-dependent field of view of a telescope with primary beam diameter $1.22\, c\,(1+z)/(\nu_0\, D)$, where D is the diameter of a single dish (for MeerKAT, $D = 13.5$ m) and ν_0 is the rest frequency of the line being observed. This diameter yields a redshift-dependent solid angle:

$$\Omega = \pi \left[\frac{1.22}{2}\frac{c\ (1+z)}{\nu_0\ D}\right]^2. \tag{2.4}$$

Integrating equation (2.3) over $d\Omega$ and substituting in equation (2.4) yields the differential volume for the LADUMA field:

$$dV = \pi \left(\frac{1.22}{2}\right)^2 \left(\frac{D_A}{\nu_0\ D}\right)^2 \frac{D_H\ (1+z)^4}{\sqrt{\Omega_m(1+z)^3 + \Omega_\Lambda}}\ dz. \tag{2.5}$$

Integrating equation (2.5) over the redshift limits of the LADUMA survey for detecting OH ($z_{\mathrm{OH}} = 0.174 - 1.876$), we obtain a total volume of $V = 0.045$ Gpc^3.

2.2.3 Sensitivity of LADUMA

The luminosity sensitivity for integrating the OHLF changes with redshift and with MeerKAT band (either the UHF or L band). The sensitivity is calculated using equation (2.6), where ΔS_ν is

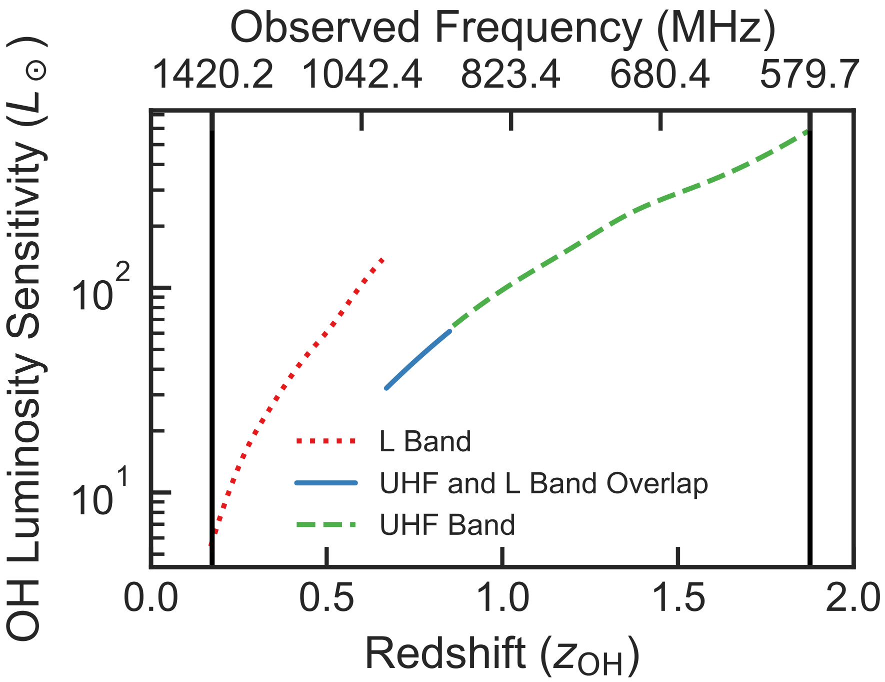

Figure 2.1 Isotropic 5σ luminosity sensitivity $L_{\rm OH}$ as a function of redshift and observed frequency. The vertical black lines show the low- and high-redshift limits of OH detection for LADUMA. The three different curves come from the two bands LADUMA will use, UHF and L bands, and the frequency range where they overlap.

the interferometric sensitivity, SEFD is the system equivalent flux density as reported by MeerKAT[1], $\eta_{\rm corr}$ is the correlator efficiency, $N_{\rm ant}$ is the number of antennas, $N_{\rm pol}$ is the number of polarizations observed, $\Delta\nu$ is the bandwidth, and Δt is the integration time:

$$\Delta S_\nu = \frac{\rm SEFD}{\eta_{\rm corr}\sqrt{N_{\rm ant}(N_{\rm ant}-1)N_{\rm pol}\Delta\nu\Delta t}}. \tag{2.6}$$

We assume that $\eta_{\rm corr} = 1$, all $N_{\rm ant} = 64$ antennas will be operating, and $N_{\rm pol} = 2$. The assumed integration times are 333 hours for the L band and 3091 hours for the UHF band, with 3424 hours for the frequency range where the receivers overlap. We also assume a velocity width of $\Delta V = 150$ km s^{-1}, the width of the average OH line at $z = 0$, converted to hertz using $\Delta\nu/(\nu_{\rm OH}/(1+z)) = \Delta V/c$. As LADUMA will be applying Briggs weighting to obtain a well-behaved synthesized beam, an extra noise penalty of 1.45 is included in sensitivity calculations. We also include the effects of

---

[1] MeerKAT SEFD values can be accessed via the SARAO MeerKAT specifications page.

primary beam attenuation away from the phase center, assuming two-dimensional Gaussian beams with half-power points defined as $0.5 \times 1.22\,\lambda/D$.

Using the sensitivity at each redshift, we calculate the 5σ luminosity limit as $L_{\rm min} = 4\pi D_L^2\, 5\, \Delta S_\nu\, \Delta\nu$ where D_L is the luminosity distance. Figure 2.1 shows how the luminosity sensitivity changes with redshift for LADUMA.

2.2.4 Dependence on the Major Merger Rate

An important element in the calculation of the number of OHMs is the galaxy merger rate, since OHMs arise in merging galaxies. This consideration leads us to introduce a factor of $(1+z)^\gamma$ in equation (2.7), where γ is determined by the galaxy merger rate (in the sense of merging events per comoving volume) and will be referred to as the *merger rate evolution coefficient*. Previous studies, based on both observations and simulations, have used different conventions for defining and parameterizing a “merger rate,” and drawn different conclusions that depend on type of merger, redshift, mass, and many other factors (e.g., Lotz et al. 2011; Rodriguez-Gomez et al. 2015; Mundy et al. 2017; Mantha et al. 2018; Duncan et al. 2019; O’Leary et al. 2021, and references therein). The relevant merger rate for OHMs is one corresponding to gas-rich major mergers, whose evolution remains poorly constrained. Therefore, we select an intermediate estimate for this merger rate evolution coefficient of $\gamma \sim 2.2$ (Rodriguez-Gomez et al. 2015; Mundy et al. 2017), which will be assumed when not stated otherwise. In Section 2.2.5, we present OHM calculations for a conservatively large range of possible γ values, $0.0 \leq \gamma \leq 3.0$, which is slightly larger than the range suggested by recent studies ($0.5 \lesssim \gamma \lesssim 2.8$) (Mundy et al. 2017; Ferreira et al. 2020).

OHMs present a unique and independent way to measure the galaxy merger rate. Once we have a secure sample of OHMs, we will be able to provide an estimated γ for gas-rich major mergers. As more H I surveys take data, this method will be a robust way for tracing the cosmic history of major mergers.

2.2.5 MCMC Calculation of N(OH)

Using the MCMC fit samples for the OHLF discussed in Section 2.2.1, we can integrate over volume, luminosity, and merger rate to get a prediction of the number of OH megamasers to be detected at the 5σ level in LADUMA as shown in equation (2.7):

$$N = \int_{L_{\rm min}}^{L_{\rm max}} \int_{0}^{V_{\rm total}} \Phi(L_{\rm OH})\ (1+z)^{\gamma}\ dV\ d\log L_{\rm OH}. \tag{2.7}$$

Figure 2.2 shows a distribution of possible values for the number of OHMs using 10,000 samples from the MCMC fit to the OHLF, assuming that $\gamma = 2.2$. The median value is 82.99, and the associated 16th and 84th percentiles are 66.49 and 103.89. The 16th and 84th percentiles are commonly associated with -1σ and $+1\sigma$ limits (for a Gaussian distribution) respectively, and they will be referred to as such for the remainder of this paper. The mean of the distribution is 85.32. The number of OH megamasers we expect to detect with LADUMA is therefore 83^{+21}_{-17}. This total would nearly double the number of known OHMs.

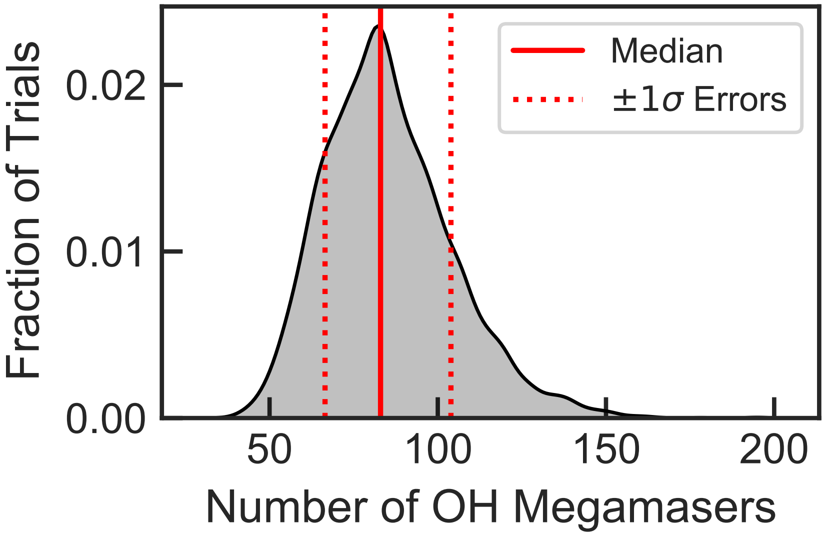

Figure 2.2 Kernel density estimation of the predicted number of OHMs to be found by LADUMA, assuming $\gamma = 2.2$, using 10,000 samples from the MCMC fit to the OHLF parameters. The expected number of OHM detections is 83^{+21}_{-17}.

As discussed in Section 2.2.4, the exact value of the merger rate evolution parameter γ is poorly constrained. Figure 2.3 presents the above calculation for values of γ ranging from 0.0 to 3.0. If γ is assumed to be 0.0, and the merger rate does not increase with redshift, then it is expected that LADUMA would detect 15^{+5}_{-3} OHMs.

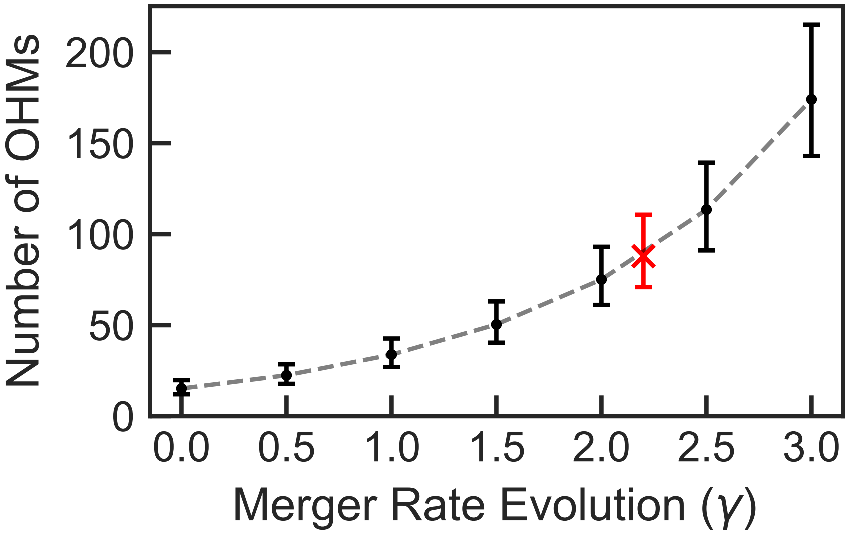

Figure 2.3 Number of OHM detections in LADUMA versus merger rate evolution parameter γ. The fiducial $\gamma = 2.2$ is denoted by a red X marker.

We can compare the impact of the OHLF presented in this work to the OHLF in Darling & Giovanelli (2002a) by calculating the numbers of OHMs implied by the two. Figure 2.4 shows how the number of OHMs varies for the two OHLFs. When $\gamma = 2.2$, the MCMC approach adopted here implies a factor of 1.4 fewer detections. In general, the larger uncertainties from calculations with the OHLF in Darling & Giovanelli (2002a) are due to the larger uncertainties in that paper's OHLF parameters.

2.3 OH Contamination in Other H I Surveys

In this section, we generalize the above calculations for H I surveys underway or planned at other radio telescope arrays, particularly the Australian Square Kilometre Array Pathfinder

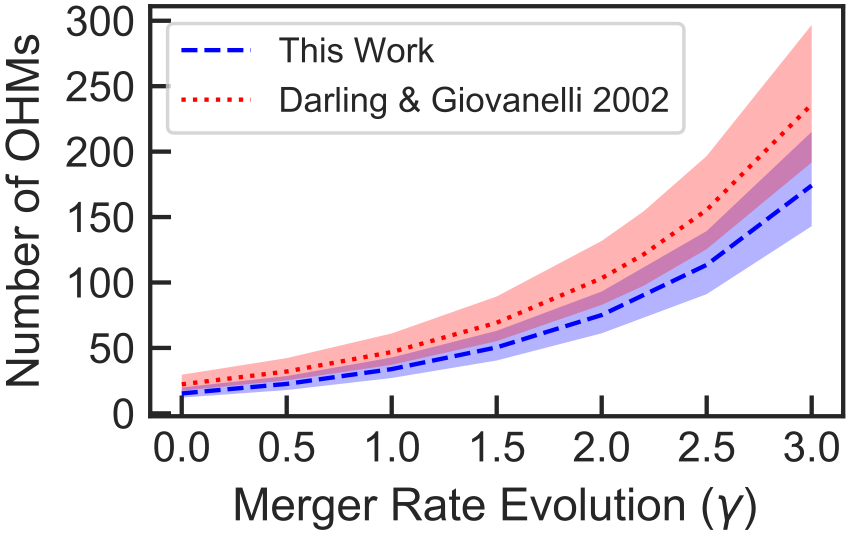

Figure 2.4 Comparison of OHM detection rate in LADUMA versus merger rate evolution coefficient for the OHLFs presented in this work and in Darling & Giovanelli (2002a). The dashed and dotted lines show the median values, and the shaded areas represent ±1σ uncertainties.

(ASKAP), the Very Large Array (VLA), the APERture Tile In Focus (APERTIF) facility, and Phase I of the SKA. The VLA and ASKAP have H I surveys underway or planned. At the VLA, the COSMOS H I Large Extragalactic Survey (CHILES), a single-pointing survey, is currently analyzing data (Fernández et al. 2016). WALLABY (Widefield ASKAP L-band Legacy All-sky blind surveY) is in the process of observing pilot fields with ASKAP alongside DINGO (Deep Investigation of Neutral Gas Origins; Duffy et al. 2012). DINGO will have two tiers, Deep and Ultra Deep. For our analysis, we consider only DINGO-Deep. APERTIF is also currently collecting data on the Westerbork Synthesis Radio Telescope (WSRT) and will execute multiple surveys at different depths. We consider the Medium Deep Survey (MDS) as described in the APERTIF Survey Plan. The SKA is a future telescope that will come in two phases, with the first (SKA1) covering ∼10% of the total collecting area of the second (SKA2; Abdalla et al. 2015). Due to the uncertainties in the schedule for SKA2, we consider only possible mid-frequency SKA1 surveys for this analysis.

The calculation of numbers of OHMs for these H I surveys uses equation (2.7) above. For each survey, we calculate $L_{\rm min}$ as a function of redshift using the reported sensitivity and we calculate the

Table 2.1. H I Survey Parameters for N(OH) Calculation

Survey	Redshift Range ($z_{\rm HI}$)	Sky Area (deg^2)	5σ Sensitivity (μJy)
LADUMA	0.0–1.45	0.90[a]	48[b]
CHILES	0.0–0.45	0.32[a]	350
WALLABY	0.0–0.26	27,500	5,000
DINGO-Deep	0.0–0.26	150	156
APERTIF MDS	0.0–0.26	450	1250
SKA1 Medium wide	0.0–0.29	400	247[b]
SKA1 Medium deep	0.0–0.50	20	52[b]
SKA1 Deep	0.35–1.37	1[a]	13[b]
SKA1 All-sky	0.0–0.50	20,000	525[b]

[a] Single-pointing survey comoving volume calculations include an expanding field of view at higher redshifts and lower observing frequencies.

[b] LADUMA and SKA1 have published frequency-dependent sensitivities, which we employ for calculations in this paper. The values presented here are the mean sensitivities across the entire range of the observed frequencies.

References. — CHILES (Fernández et al. 2013), WALLABY & DINGO-Deep (Duffy et al. 2012), APERTIF (Apertif Survey Plan), SKA1 (Braun et al. 2019; Staveley-Smith & Oosterloo 2015) volume using redshift ranges and sky coverage. All assumptions made about the survey or telescope for these calculations are presented in Table 2.1. The sensitivity column assumes a velocity width of 150 km s^{-1} as done for the LADUMA calculations. Concepts for the SKA1 surveys come from Staveley-Smith & Oosterloo (2015). Each of the three fiducial surveys (medium wide, medium deep, and deep) assumes a total observing time of 1,000 hours, while the all-sky commensal survey assumes an observing time of 10,000 hours. Staveley-Smith & Oosterloo (2015) note that angular resolutions finer than 10" are only accessible to the SKA for high column densities — a limitation that especially applies to the SKA1 Deep survey, whose nominal angular resolution is 2". We have not modeled the effects of resolution on the detectability of OHMs, but we note that at high resolutions, there could be a bias in favor of detecting (more compact) OHMs relative to (more extended) H I emitters.[2]

For surveys featuring single pointings, we have calculated comoving volumes assuming that sky area increases $\propto (1 + z_{\mathrm{H\,I}})^2$ due to the increasing size of the primary beam at lower frequencies. This calculation applies to CHILES, LADUMA, and a hypothetical SKA1 Deep survey and is noted in Table 2.1. For surveys covering larger sky areas through the use of multiple pointings across contiguous patches, sky area will be higher at $z_{\mathrm{H\,I}} > 0$ than at $z_{\mathrm{H\,I}} = 0$, but the change will be less dramatic because only the pointings that lie at the edges of the contiguous patches will contribute. Because this effect will be small in a fractional sense (smaller for larger sky areas), and will depend on the detailed distribution of patch sizes, we do not correct for it. We also choose to omit primary beam attenuation when predicting OHM contamination of other H I surveys, since we cite values for the numbers of H I detections that do not include this consideration (Staveley-Smith & Oosterloo 2015).

Table 2.2 presents the number of OHMs predicted to be detected in each survey for merger rate evolution coefficient $\gamma = 2.2$. Table 2.2 also presents the number of H I sources each survey

---

[2] This paper's predictions ignore the effects of radio frequency interference, which can vary for different sites and different array configurations. Here too, it may in practice be systematically easier to recover more compact OHMs than more extended H I emitters in frequency ranges where RFI precludes the use of short-baseline data.

Table 2.2. Predicted 5σ OHM and H I Detections for Untargeted H I Surveys

Survey	N(OH)	N(H I)	N(OH)/N(H I)
LADUMA	$8.3^{+2.1}_{-1.7} \times 10^1$	8×10^3	$1.03^{+0.26}_{-0.20}\%$
CHILES	$5.5^{+1.1}_{-0.9} \times 10^{-1}$	3×10^2	$0.18^{+0.04}_{-0.03}\%$
WALLABY	$8.9^{+2.5}_{-1.8} \times 10^2$	6×10^5	$0.15^{+0.04}_{-0.03}\%$
DINGO-Deep	$7.5^{+2.3}_{-1.7} \times 10^1$	5×10^4	$0.15^{+0.04}_{-0.03}\%$
APERTIF MDS	$2.6^{+0.6}_{-0.5} \times 10^2$	3×10^5	$0.09^{+0.02}_{-0.01}\%$
SKA1 Medium wide	$2.5^{+0.7}_{-0.6} \times 10^2$	3.4×10^4	$0.73^{+0.21}_{-0.17}\%$
SKA1 Medium deep	$7.7^{+3.2}_{-2.3} \times 10^1$	2.5×10^4	$0.31^{+0.13}_{-0.09}\%$
SKA1 Deep	$1.9^{+0.6}_{-0.5} \times 10^2$	2.6×10^3	$7.20^{+2.32}_{-1.81}\%$
SKA1 All-sky	$4.1^{+1.0}_{-0.8} \times 10^3$	5.5×10^5	$0.75^{+0.18}_{-0.14}\%$

Note. — N(OH) values assume merger rate evolution coefficient $\gamma = 2.2$.

expects to detect. The contamination column is the ratio of OHM detections to H I detections, which can be related to the fraction of an "H I sample" that will actually be OHMs mistaken for H I sources if spectroscopic redshifts are unavailable.

One noteworthy aspect from Table 2.2 is the much higher rate of contamination for LADUMA and the SKA1 Deep survey compared to the other surveys. These are distinctly different from the other H I surveys due the fact that they extend to significantly higher redshift. We therefore infer that H I detections dominate at low redshifts (i.e., $z_{\mathrm{HI}} \lesssim 1$) for all surveys. However, the OH detection density surpasses the H I detection density at redshifts above $z_{\mathrm{HI}} \sim 1$ — an effect that is pronounced for single-pointing surveys that have much larger relative fields of view at high versus low redshifts.

An earlier conclusion in the same vein was reached by Briggs (1998), who predicts that OHM contamination in H I surveys will increase with redshift. We explore how that contamination depends on redshift using both LADUMA and an expanded version of the SKA1 Deep survey for comparison. The SKA1 Deep survey presented in Staveley-Smith & Oosterloo (2015) only covers a frequency range of 600–1050 MHz that corresponds to only a portion of the full SKA1 mid-band (Braun et al. 2019). For the purpose of exploring OH contamination versus redshift, we assume a deep survey that exploits the full range of the mid-band and therefore covers a frequency range of 600–1420 MHz. Equation (2.7) is used to estimate how the number of OHMs varies with redshift. To estimate the number of H I detections per redshift interval, we use the following equation from Obreschkow et al. (2009):

$$\frac{dN/dz}{1\ \mathrm{deg}^2} = 10^{c_1}\ z^{c_2}\ e^{-c_3 z}, \tag{2.8}$$

where the c_i are parameters specific to each H I survey. LADUMA's values are interpolated from Obreschkow et al. (2009) for each redshift using sensitivities calculated from equation (2.6) as the limiting integrated flux, and assuming linewidths of 100 km s^{-1}, allowing us to determine H I detection rate versus redshift. We follow a similar method for the SKA1 Deep survey using sensitivity values presented in Braun et al. (2019). We calculate how number density for OH and H I varies with redshift, assuming redshift bins of $dz = 0.01$. Obreschkow et al. (2009) note that dN/dz will be $\geq 1\%$ underestimated for $z \leq z_c$ where z_c depends on the limiting flux. For both LADUMA and SKA1 Deep, on average, $z_c \sim 0.1$. Therefore, the numbers of H I detections are slightly underestimated for $z_{\rm HI} \leq 0.1$.

Figure 2.5 shows how the detection rate of OH and H I varies with redshift. H I detections dominate at low redshift for both surveys. At higher redshifts, the OH detection rate and OH fraction grow significantly. This comparison also demonstrates how the OHM contamination rate depends on survey parameters, as discussed in Section 2.3. For LADUMA, OHMs will not outnumber H I source at any redshift probed by the survey (i.e., for any $z_{\rm HI} \leq 1.45$); in comparison, SKA1 Deep's sensitivity as a function of frequency will yield a number of OH detections surpassing that of H I detections for $z_{\rm HI} \geq 1.25$.

Briggs (1998) first presented this issue of OH contamination in untargeted H I surveys. Results from that paper demonstrated that by redshift $\rm z_{HI} \sim 1.0$, OH detections would significantly outnumber H I detections for a much shallower survey ($5\sigma = 5$ mJy) than LADUMA or SKA1 Deep. The predicted transition from an H I -dominated to an OH-dominated sample is qualitatively consistent with our findings, although the precise redshift at which this happens depends on survey parameters. In general, the deeper a survey observes over a given frequency range, the more H I emitters it will detect relative to OHMs. LADUMA and SKA1 Deep are both deeper than the hypothetical Briggs (1998) survey, allowing them to detect more H I sources at higher redshifts and thus to push out the projected redshift at which OH detections outnumber H I detections. The fact that this transition occurs at a lower redshift ($z_{\rm H\,I} = 1.25$) for SKA1 than for LADUMA owes to the fact that LADUMA's sensitivity improves at higher redshifts (due to its distribution of observing time), in contrast to the SKA1 Deep sensitivity.

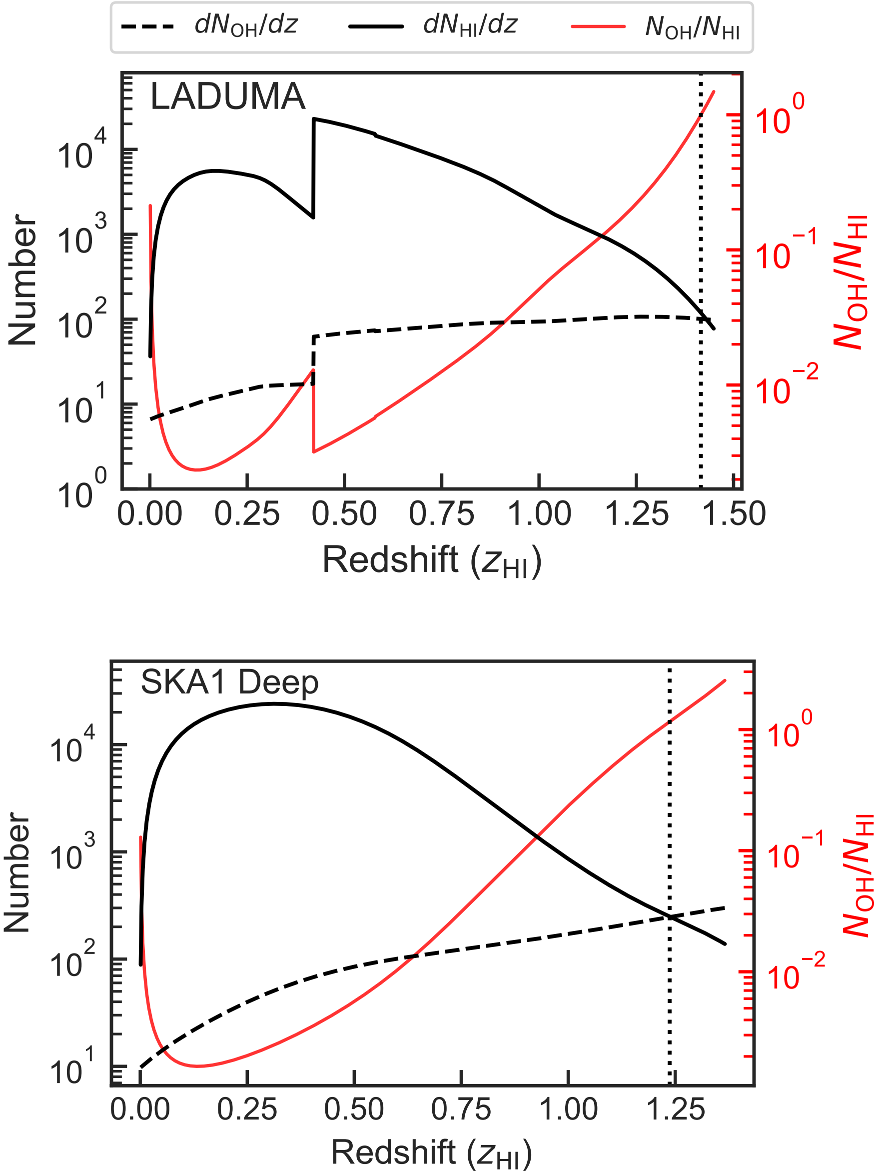

Figure 2.5 Projected numbers of OHMs and H I sources and the OHM fraction (N_{OH}/N_{HI}) vs redshift z_{HI} for LADUMA (above) and SKA1 Deep (below). Left axis shows numbers of objects (plotted in black); the dashed curve indicates how the number of OH detections changes with redshift, and the solid curve indicates the same for H I detections. Right axis shows the ratio of OHM detections to H I detections (plotted in red). The vertical dotted lines indicate the redshifts where the numbers of OH and H I detections are equal. The discontinuities in the LADUMA curves originate from the overlap between the L and UHF bands. All calculations assume galaxy merger rate evolution parameter $\gamma = 2.2$.

2.4 Identifying OH Megamasers in Untargeted H I Surveys

Distinguishing an OH from an H I line is currently only done using the optical spectroscopic redshift of an object to determine an observed line's rest wavelength. Next-generation H I surveys will observe orders of magnitude more objects than previous surveys, as shown in Table 2.3, most of which will not have spectroscopic redshifts available. For that reason, we explore machine learning as a way to distinguish OH from H I emission lines using ancillary data.

2.4.1 Creating OH and H I Models for Distinguishing Populations

2.4.1.1 Fitting OHM Host Galaxy SEDs

The limited number of OHMs creates serious limitations in understanding the OH population and how it differs from H I hosts. We therefore fit the spectral energy distributions (SEDs) of 111 OHMs using Multi-wavelength Analysis of Galaxy Physical Properties (MAGPHYS; da Cunha et al. 2008), a software package that fits galaxy SEDs using physical parameters of galaxies at the same redshifts and in the same photometric bands.

MAGPHYS fits SEDs from far-UV to far-IR, so we use photometry from that range for fitting OHM host SEDs. In total, we use photometry from eight sources: the *Galaxy Evolution Explorer* (*GALEX*; Martin et al. 2005), the Sloan Digital Sky Survey (SDSS; Stoughton et al. 2002), the Two Micron All-Sky Survey (2MASS; Skrutskie et al. 2006), the *Wide-field Infrared Survey Explorer* (*WISE*; Wright et al. 2010), the Infrared Array Camera (IRAC) and Multiband Infrared Photometer for *Spitzer* (MIPS) (both on *Spitzer*; Werner 2005), the *Infrared Space Observatory* (*ISO*; Kessler et al. 1996), and the *Infrared Astronomical Satellite* (*IRAS*; Beichman et al. 1988). In total, from these sources, we use up to 33 bands to fit OHM SEDs. We omit *WISE* band 1 (3.4 µm) if *Spitzer* IRAC band 1 (3.6 µm) exists for a given galaxy because the introduction of both causes poor fits, and IRAC tends to have smaller uncertainties than *WISE*. The same is done for *WISE* and IRAC band 2 (4.6 and 4.5 µm, respectively).

In Figure 2.6, we present examples of these SED fits. For comparison, we use the Atlas of

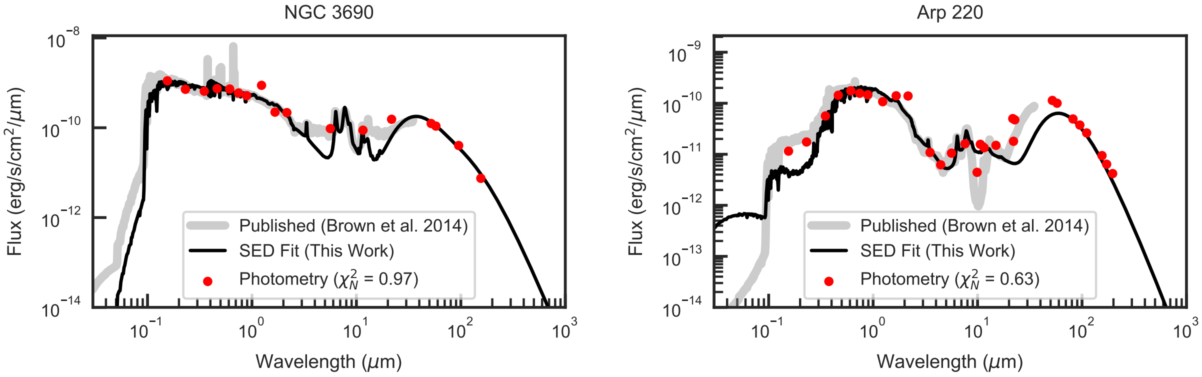

Figure 2.6 Examples of SED fits with MAGPHYS (black line). The published SED comes from Brown et al. (2014) and is shown as a thick grey line. Red dots denote the photometry used in a given fit.

Galaxy SEDs (Brown et al. 2014), which includes a total of seven OHM host galaxy SEDs. The fits we present are imperfect matches to the complete Brown et al. (2014) SEDs, and we emphasize that our SED fits were done with the limited scope of reproducing observations of OHMs in our particular wavelength regime of interest, UV to mid-IR. Our fits are limited in wavelength outside this range, particularly in the far-IR. Although far-IR photometry would provide very useful information, data are sparse and unavailable for our objects of interest, so we have chosen to omit far-IR photometry.

2.4.1.2 Emulating OHM Host Photometry

We use our SED fits to model OHM host galaxy observations for various missions and surveys as a function of redshift. We use PYPHOT,[3] a package for calculating an object's photometry from its SED. It calculates the photometry using a given filter's transmission curve, $T(\lambda)$, by calculating the photon number flux:

$$N_{\text{tot}} = \frac{1}{hc} \int_{\lambda} f_{\lambda}\ \lambda\ T(\lambda)\ d\lambda, \tag{2.9}$$

where f_λ is the flux density as shown above in Figure 2.6.

The greatest benefit of having SED fits is the ability to redshift them and mimic observations at higher redshifts. This scaling is done by adjusting the rest wavelength and the flux density by

---

[3] PYPHOT's documentation can be accessed at https://mfouesneau.github.io/docs/pyphot/.

the inverse square of the luminosity distance and a redshift factor ($\propto D_L^{-2}\ (1+z)^{-1}$) and then re-"observing" the OHM host. This method is used to create synthetic observations out to the desired redshifts.

2.4.1.3 Emulating H I Host Galaxy Photometry

For consistency, H I host galaxy photometry is created similarly. However, instead of fitting SEDs, we use 57 SEDs[4] published in the Atlas of Galaxy SEDs (Brown et al. 2014) that have previous H I detections, a population of mainly spiral galaxies. Since these sources are not drawn from a strictly H I -selected sample, they may not behave identically to samples from untargeted H I surveys, although we expect differences to be modest. These SEDs are also redshifted, and photometry is "measured" using PYPHOT.

2.4.2 Machine Learning to Distinguish OH from H I

To aid in determining if an emission line is an H I or OH detection, we use machine learning algorithms to determine the likelihood of the line's classification. We employ a k-Nearest Neighbors (k-NN) algorithm that classifies objects based on a plurality vote of their neighbors' classes, where neighbors are determined within some parameter space (Goldberger et al. 2005). k-NN classification is a non-parametric method and a *lazy learning* algorithm. Lazy learning means that the algorithm itself does not make assumptions or generalizations based on the training data, but instead uses those data to make direct decisions about the testing data. Algorithm "optimization" is purely done by our choices about the nearest-neighbor algorithm parameters used. The cost of using a lazy learning algorithm is the computation time in the testing phase. However, we are not testing on data sets large enough for slow speed to be problematic. This context makes the k-NN classification a robust and transparent method for our purposes.

---

[4] This number was originally 58 SEDs; however, after some examination, NGC 7674 seems to behave much more like an OHM in the near- to mid-IR like just a spiral galaxy, despite looking like a classic spiral morphologically. We attempted to do follow-up observations to determine if it potentially possessed both emission lines; however the OH line cannot be observed due to RFI. We therefore removed this galaxy from our H I SED sample.

The final classification parameters are *WISE* magnitudes and colors as well as the observed line frequency. Suess et al. (2016) demonstrate that *WISE* photometry can separate OHM and H I populations at low redshift. We also choose *WISE* because of its all-sky coverage, allowing it to be applicable to many different H I surveys. Section 2.4.2.1 discusses the use of *WISE* magnitudes and colors to distinguish H I and OH populations, as well as the limitations of using *WISE* and its similarities to IRAC. Section 2.4.2.2 presents similar exercises using IRAC data, which have significant coverage over the LADUMA field but are otherwise less broadly applicable for other H I surveys.

2.4.2.1 OH and H I Classification Using WISE

The analysis in Suess et al. (2016) is done with low-redshift ($z < 0.1$) objects and uses *WISE* bands W1, W2, W3, and W4 (3.4, 4.6, 12, 22 µm). W3 and W4 are very insensitive compared to W1 and W2; thus, this method is limited by both object brightness and redshift. We focus on using machine learning to sort using only W1 and W2 magnitudes, W1−W2 color, and the observed line frequency.

One of the cuts from Suess et al. (2016) is done in the color-magnitude space of W1 versus W1−W2 (or [3.4] versus [3.4]−[4.6]). We use this same parameter space for the k-NN algorithm. Examples of redshift evolution in this space are shown in Figure 2.7 for an OHM host and an H I source. These data are "measured" from their SEDs and show how OH-H I separability varies with redshift.

We use the 57 H I and 111 OHM host SEDs to test and train the k-NN algorithm. Each SED is redshifted to the maximum redshift detectable by LADUMA ($z_{\mathrm{HI}} = 1.45$ and $z_{\mathrm{OH}} = 1.876$), with *WISE* photometry being "measured" roughly every $dz = 0.01$. We then remove any data too faint to have a 5σ WISE detection.

k-NN algorithms require feature scaling or parameter normalization, since the algorithm is inherently built on the distances between a data point and its neighbors. Therefore, we normalize each parameter from 0 to 1. k-NN classification algorithms are dependent on a few parameters that

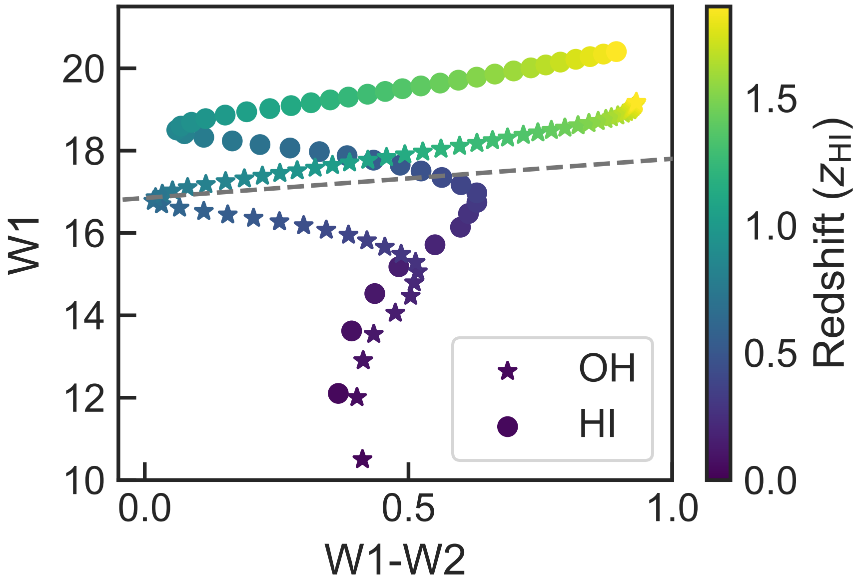

Figure 2.7 Predicted *WISE* magnitude versus color for an OHM host galaxy (stars) and an H I galaxy (circles). H I redshift is denoted by color with redshift increasing with lightness. The corresponding OH points lie at the same observed frequency but are at a higher actual redshift. The grey dashed line represents the detection limit of *WISE* (the region above the line is undetectable by *WISE* band W1).

can be optimized for a given case. Parameters that were varied and tested for our purposes include the number of neighbors that is included in the plurality vote on an object's classification (k), whether neighbors are weighted by their distances, and how distance between objects is calculated (p). The distance between points is defined by the Minkowski distance of order p:

$$D(X, Y) = \left(\sum_{i=1}^{n} |x_i - y_i|^p \right)^{\frac{1}{p}}, \tag{2.10}$$

where X and Y are two points in an n-dimensional parameter space. Euclidean distance is recovered for $p = 2$.

All algorithm optimization for this work is done by maximizing OH *recall*. In machine learning classification, two metrics that are often considered when optimizing are *precision* and *recall*, both of which scale from 0 to 1 (1 being the best score). *Precision* is the fraction of positive identifications that are correct. By optimizing precision, the number of false positives (or Type I errors) is minimized. *Recall*, conversely, is the fraction of positives that were correctly identified. When recall is optimized, the number of false negatives (or Type II errors) is minimized (Sammut & Webb 2011). These terms correspond to the familiar astronomical concepts of sample purity and completeness. In our case, a positive identification is the classification of a galaxy as an OHM host. We choose to optimize OH recall due to the rarity of OHMs and the desire to not miss any potential candidates. Although this approach increases the number of false positives, this algorithm does add information, and any positive identification it makes can motivate follow-up observations for confirmation.

The algorithm parameter exploration is shown in Figure 2.8. The x-axis shows a wide range of choices for the number of neighbors used, the lines plotted show a few choices for Minkowski distance, and the two panels show the difference between weighting and not weighting neighbors by distance. Each unique combination of parameters is tested using a five-fold cross-validation test. This process involves randomly sorting our data into two sets: training and testing data. The training data build the algorithm and the testing data determine how successful the algorithm is. This split was done five times, randomly splitting data each time, for each combination of parameters, and the final OH recall was determined by averaging the five individual OH recall values. In total, 2,000 k-NN algorithms were tested.

The results of these parameter tests give the highest OH recall for large numbers of neighbors ($k > 10^3$). Although an OH recall of 1 would be ideal, this result comes at the cost of very low precision and defeats the purpose of the k-NN method by classifying based on the value of an algorithmic parameter instead of position relative to neighbors. Large numbers of neighbors also make for very computationally expensive algorithms. One common approach is to select $k = \sqrt{N}$, where N is the number of data points, but for our data ($k \approx 140$), this choice of k is near the lowest value of OH recall. Another common approach is to select $k = 1$ or another low number. For small data sets, always assuming the nearest object has the same classification can introduce noise. However, with a sufficiently large data set, this trend is less problematic. Figure 2.8 indicates that a small k achieves a recall of over 0.98 for distance-weighted learning. We stress that there exists no optimal k for all purposes, since each k-NN optimization varies based on the properties of the

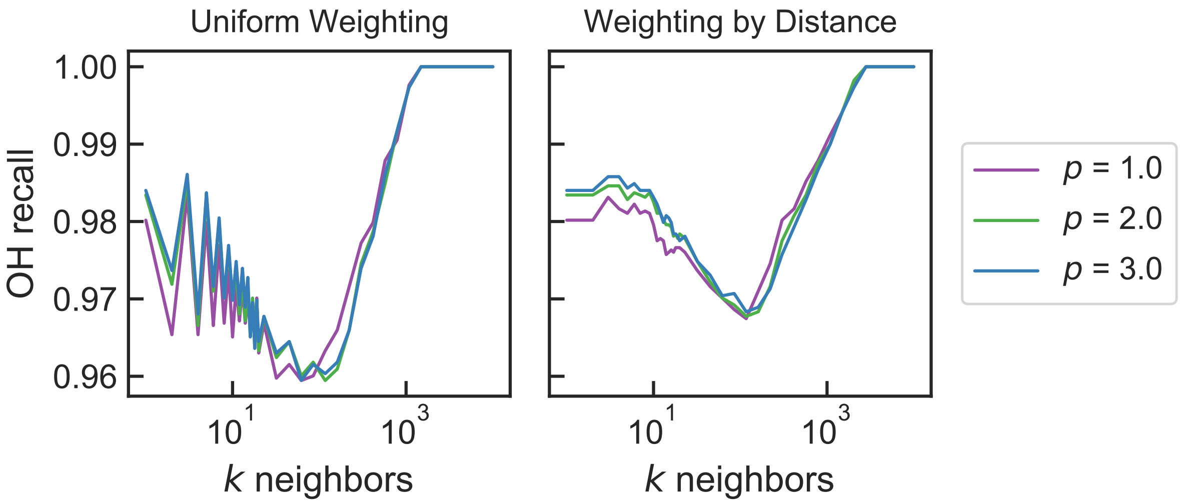

Figure 2.8 Parameter exploration for our k-Nearest Neighbors (k-NN) classification algorithm. We vary the number of neighbors considered in voting (x-axis), whether distance is weighted (left and right plots), and how distance is determined using the Minkowski metric (the lines plotted). Each test is done using five-fold cross-validation.

data (Altman 1992).

We choose our number of neighbors to be $k = 3$, based on the above considerations. Increasing a small amount above $k = 1$ also reduces noise while maximizing OH recall. For weighting and Minkowski metric, we choose to weigh votes by distance and use standard Euclidean distance ($p = 2$).

The final trained and tested k-NN algorithm results are shown in the top panel of Figure 2.9. The blue and red points show correctly identified OH and H I host galaxies respectively, and the black stars are misidentified objects. The incorrect identifications concentrate where OH and H I sources overlap the most at the same observed frequency, and indicate where there will be the most confusion. The final OH recall is **0.985** and the OH precision is **0.974**. In other words, for redshifts less than $z \sim 1.0$, we expect to identify 98.5% of OH lines in H I surveys, thereby mitigating the impact of contamination.

We repeat this process for another Suess et al. (2016) parameter space, W1−W2 versus W2−W3, as well as the observed line frequency. This alternative approach significantly limits the number of available detections because of the inclusion of the comparatively less sensitive W3 band. This approach however leads to a higher OH precision, since mid-IR data are relevant for distinguishing between these populations. The results of this test are shown in the bottom panel of Figure 2.9. Precision and recall from this test are compared to those for other tests in Table 2.3.

2.4.2.2 OH and H I Classification Using IRAC

As discussed previously, *WISE* is insensitive to galaxies at redshifts above $z \sim 1.0$. Although having significantly less sky coverage than *WISE*, *Spitzer*'s IRAC bands 1 and 2 are very similar to *WISE* bands 1 and 2 but are much more sensitive and can detect OHM and H I host galaxies over the full redshift ranges probed by both LADUMA and SKA1. We therefore perform an exercise similar to that in Section 2.4.2.1 using IRAC data. Throughout this paper, IRAC bands are referred to by their wavelengths in microns (e.g., IRAC [3.6] denotes the 3.6 μm band magnitude).

We use a parameter space analogous to the first test for the IRAC k-NN algorithm ([3.6] versus [3.6]−[4.5]). (As a reminder, *WISE* uses Vega-based magnitudes, whereas IRAC uses AB magnitudes.) Since IRAC is sensitive to the entire redshift range of our H I and OHM hosts, we do not perform any detection cuts. Results from this exercise are presented in Table 2.3 and visualized in Figure 2.10. Comparing to the analogous *WISE* space, this test has the same OH precision, but OH recall suffers slightly. However, achieving an OH recall of 0.979 is still a powerful tool when it comes to sorting OHM hosts from H I hosts, and the ability to probe to higher redshifts has strong appeal.

We also consider IRAC [3.6]−[4.5] versus [5.8]−[8.0]. Stern et al. (2005) suggest that cuts in this space can separate active galaxies from normal galaxies. We perform algorithm optimizations similar to those mentioned previously before training and testing. We present the final results in Table 2.3 and Figure 2.10. Despite having information from the [8.0] band, this test performs slightly worse than the previous tests in both OH recall and precision, indicating that the overlap between OHM and H I hosts is greater in this parameter space than in the previous alternatives.

Being able to probe the full redshift range of LADUMA is beneficial, but inevitably introduces more contamination, as indicated by the slightly reduced OH recall. However, it is worth noting

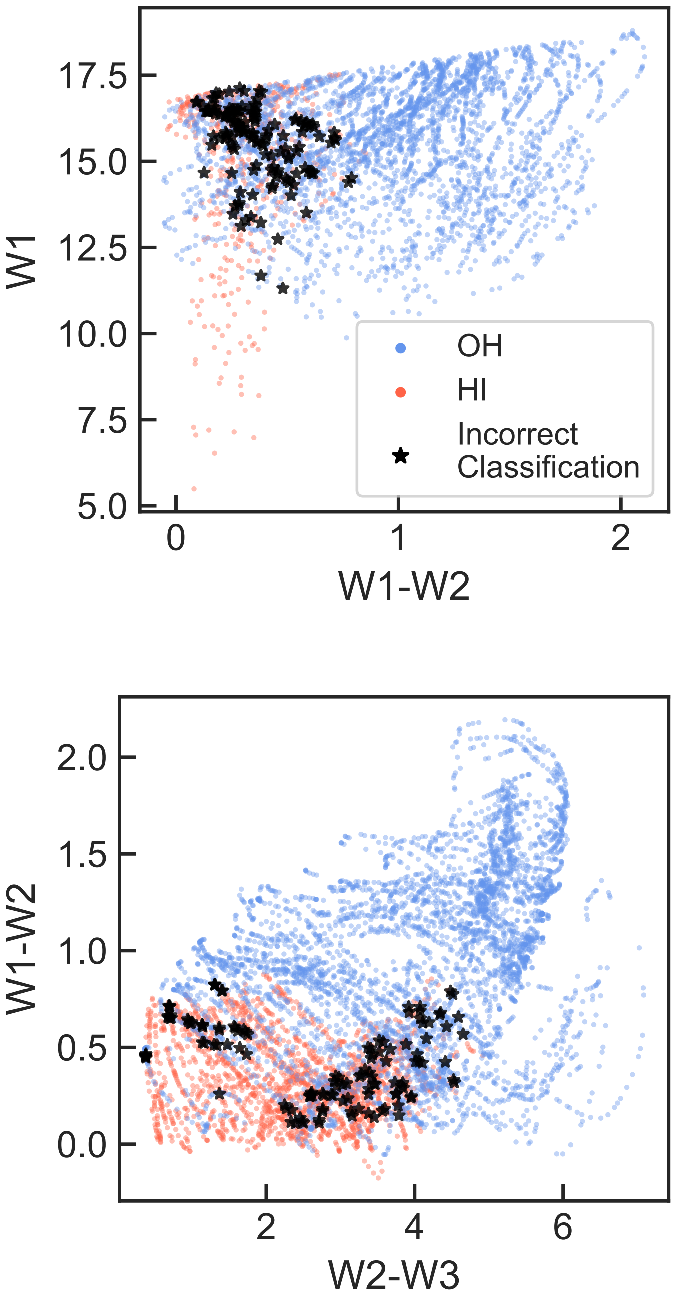

Figure 2.9 Final results from training and testing our *k*-NN algorithm using *WISE* W1 versus W1−W2 (above) and W1−W2 versus W2−W3 (below). Blue points indicate OH host testing points that were correctly identified, and red indicate the same for H I sources. Black stars show the misidentified objects, either OH misidentified as H I or vice versa (3.6% of objects in top panel, 1.9% of objects in bottom panel). Note that the OH and H I markers are partially transparent to show overlapping.

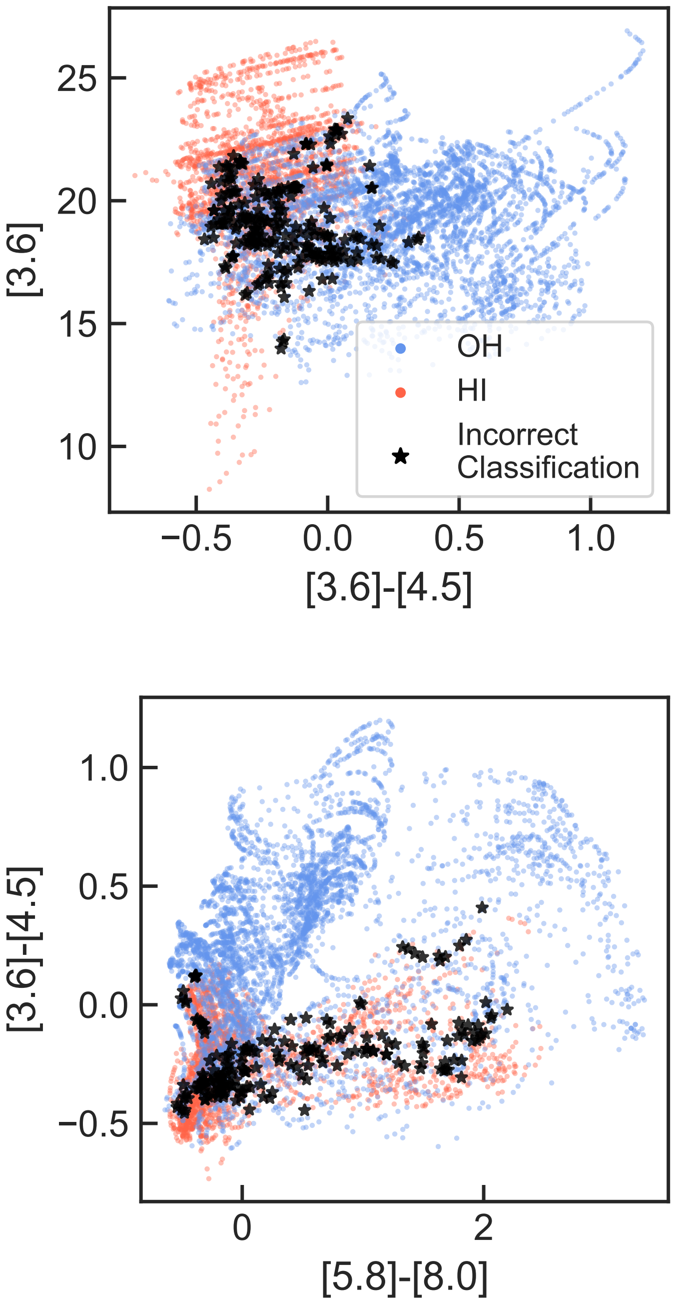

Figure 2.10 Final results from training and testing our k-NN algorithm using *Spitzer* IRAC [3.6] versus [3.6]−[4.5] (above) and [3.6]−[4.5] versus [5.8]−[8.0] (below). Blue points indicate OH host testing points that were correctly identified, and red indicate the same for H I sources. Black stars show misidentified objects (3.4% of objects in top panel, 2.9% of objects in bottom panel). Note that the OH and H I markers are partially transparent to show overlapping.

that despite being lower, these recall values still exceed 95%. These IRAC and *WISE* tests create

Table 2.3. Machine Learning Results for Distinguishing H I Emission Lines from OH Megamasers

Mission	Features	OH Recall	OH Precision
WISE	W1, W1−W2, ν	0.985	0.974
WISE	W1−W2, W2−W3, ν	0.987	0.985
IRAC	[3.6], [3.6]−[4.5], ν	0.979	0.972
IRAC	[3.6]−[4.5], [5.8]−[8.0], ν	0.982	0.976

Note. — The features column indicates what data were used to distinguish H I from OHM host galaxies. Each row includes the observed frequency (ν) of the line in question (OH or H I) to assist in separation of sources.

a new framework for the process of separating OH and H I host populations.

2.5 Discussion

The methods presented in this paper will be crucial to mitigating OHM contamination of H I emission-line surveys. *WISE* provides the all-sky coverage needed for upcoming surveys that will be covering large portions of the sky, while IRAC has the deep-field coverage needed for surveys such as LADUMA, which will be the deepest H I emission-line survey to date.

One of the biggest shortcomings of these methods and calculations is that they are based on known OHMs, which currently extend to a highest redshift of $z_{\rm OH} = 0.264$ (Darling & Giovanelli 2002b). This limitation has forced us to make some extrapolations to obtain predictions for higher-redshift surveys. This approach is unavoidable until we have higher-redshift data on both H I and OH populations. As more surveys are conducted, we will be able to update the OHLF and OH SED evolution as well as provide tighter constraints on these calculations and predictions.

As discussed in Section 2.1, H I and OH sources can be separated by spectroscopic redshift. It is therefore worth recognizing that some objects will be readily identifiable and that these objects will be crucial for helping classify those without redshifts. For LADUMA, the current largest source of spectroscopic redshifts is the PRIsm MUlti-Object Survey (PRIMUS), with over 32,000 redshifts in the field and in the relevant redshift range (Coil et al. 2011). PRIMUS only detects galaxies out to $z \sim 1.2$, meaning that some of the most potentially contaminated (i.e., highest) redshift ranges will have few spectroscopic redshifts available. Another source of spectroscopic redshifts soon to come online is the Wide-Area VISTA Extragalactic Survey (WAVES), which will have two campaigns, WAVES-Wide (large-sky, low-redshift) and WAVES-Deep (small-area, high-redshift) (Driver et al. 2019). WAVES-Deep will have several small patches, including one on the LADUMA field. Slated to target 45,000 objects, WAVES-Deep will also be crucial in identifying objects; however the current estimates only show detections out to redshift $z \sim 0.8$. For future all-sky untargeted H I surveys such as those on ASKAP or the SKA, WAVES-Wide aims to provide 880,000 spectroscopic redshifts out to redshift $z \sim 0.2$. Although we may have many redshifts for identifying objects as OH or H I sources, these redshifts are extremely limited where potential OH contamination is the greatest threat.

WISE and IRAC photometry were not the only data tested in Section 2.4 for the ability to separate OHM and H I hosts. We also tested other photometry for separability, focusing on data that have significant coverage in the LADUMA field. These include SDSS *ugr*, Johnson *UBV*, and *HST* ACS, WFC3, and NICMOS bands. Figure 2.11 shows how each of these bands correlates with OH/H I classification. For each band, a Pearson correlation test was done for three redshift ranges. Bands are grouped on the x-axis and then sorted by increasing wavelength. Figure 2.11 demonstrates the sorting value of bands in the near- to mid-IR. This distinction is due to the extreme star formation in OHM host galaxies, which is detected in the IR. Optical bands are poorer candidates for separation, since they are less sensitive to high star-formation rates in dusty, gas-rich systems.

2.6 Conclusions

We present predictions for the numbers of OH megamasers that will be detected in future untargeted H I surveys and explore how those numbers impact H I source confusion over a range of redshifts up to $z_{\rm HI} = 1.5$. To assist in untangling these populations, we also present methods for

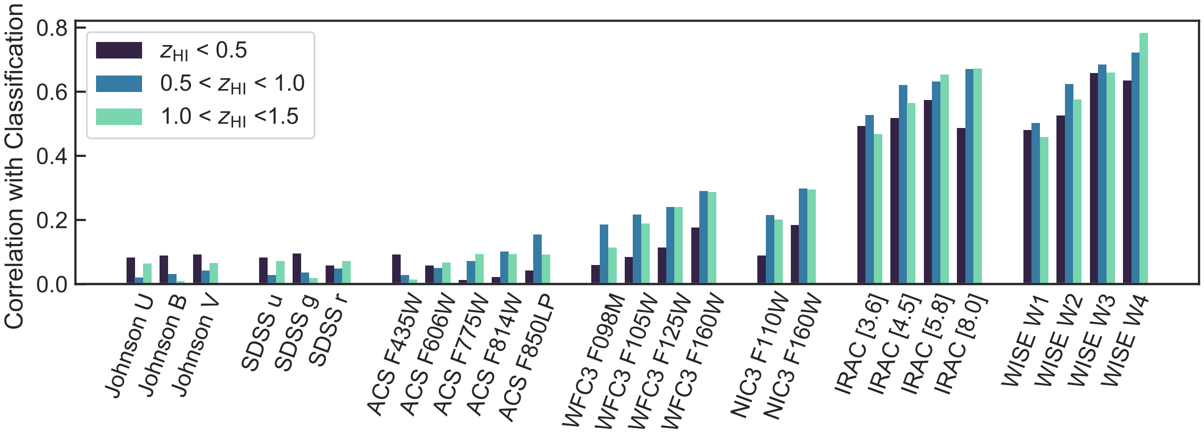

Figure 2.11 Correlation of band photometry with OH/H I classification using a Pearson correlation test. Bands on the x-axis are grouped by mission or type and then ordered by increasing wavelength. Each correlation is tested in three redshift ranges.

estimating the likelihood that a line has been identified as H I or OH. Below, we summarize our predictions and discuss the implications of this work for future H I surveys:

(1) LADUMA will likely triple the number of known OHMs: we predict 83^{+21}_{-17} new detections. Larger surveys with telescopes such as the SKA1 will detect thousands more OHMs.

(2) The contamination these OHM detections will impose on H I line surveys is highly dependent on redshift (and, secondarily, depth). In a line flux-limited survey, OHMs are more abundant at higher redshift, while H I sources become sparser. For these high-redshift surveys, OH detections will outnumber H I detections near redshift $z_{\rm HI} \sim 1.0$.

(3) Near- and mid-IR observations can assist in separating H I from OHM emission lines, which we demonstrate using a k-Nearest Neighbors machine learning algorithm. We will be able to identify nearly 99% of OH lines for redshifts less than $z \sim 1.0$ and 96% of lines at higher redshifts.

Although OHM host galaxies represent a potential contamination for untargeted H I line surveys, these rare and interesting objects can be important scientific tools. As discussed in Section 2.2.4, OHM density can also provide an independent measurement on the major merger rate evolution paramater, γ, since OHMs serve as tracers of major galaxy mergers. These galaxies are signposts of the most extreme star formation in our universe, signaling where the most massive starbursts are happening (Briggs 1998), and can even offer a way to measure in-situ magnetic fields using Zeeman splitting (Robishaw et al. 2008; McBride et al. 2014). The methods presented in this paper and follow-up observations will begin uncovering these galaxies and allowing us to characterize them at higher redshifts and potentially create better methods for mitigating contamination in H I surveys.

Acknowledgements

This work has been supported by the National Science Foundation through grant AST-1814648 (to HR and JD) and AST-1814421 (to AB). This research has made use of the NASA/IPAC Extragalactic Database (NED), which is funded by the National Aeronautics and Space Administration and operated by the California Institute of Technology. We thank Sarah Blyth, Natasha Maddox, and Aaron Stemo for helpful insights and conversations. We also thank the anonymous referee for their thorough and helpful comments which improved the presentation of this paper.

Chapter 3

Identification of OH Megamasers in Existing and Recent H I Catalogs: New Detections and Updates to Flagging Methods

Abstract

OH megamasers (OHMs) are extragalactic masers produced in major gas-rich galaxy mergers. Despite significant efforts, only 120 OHMs have been identified since their discovery in 1982 and any uniquely distinguishing features of the OHM host galaxy population have eluded detection. As radio astronomy enters a new era marked by next-generation telescopes and comprehensive 21 cm H I surveys, Square Kilometre Array (SKA) precursors will be able to serendipitously detect the 18 cm OH masing line, increasing the number of known OHMs by an order of magnitude. However, without independent spectroscopic redshifts, these sources can masquerade as H I emitters at a lower redshift than the true OHM host. Roberts et al. (2021) presented methods for identifying these interloping OHMs in H I surveys using near- to mid-IR photometry and the observed frequency of the line. Here, we test these methods using existing data from Arecibo L-Band Feed Array Survey (ALFALFA) and a preliminary catalog using brand new data from Apertif, a phased-array feed for the Westerbork Synthesis Radio Telescope (WSRT). We observed 142 optical objects (107 from ALFALFA and 35 from APERTIF) associated with 120 radio emission line sources using the Dual Imaging Spectrograph (DIS) on the 3.5m telescope at Apache Point Observatory (APO). The results of this in-depth test of these methods led to an updated OHM flagging algorithm, as well as the identification of five new OHMs previously believed to be H I sources in ALFALFA.

This chapter is in preparation and will be submitted for publication in ApJ in 2023.

3.1 Introduction

OH megamasers (OHMs) are rare, luminous 18 cm masers found in (ultra-)luminous infrared galaxies ([U]LIRGs), produced in major gas-rich mergers and are associated with extreme star formation rates (Darling 2007). Despite extensive searches, only about 110 OHM hosts have been found in the 40 years since their initial discovery (e.g. Staveley-Smith et al. 1987; Darling & Giovanelli 2002a; Willett 2012). Most of these searches have targeted IR luminous galaxies, however $\sim$ 80% of (U)LIRGs show no masing activity Willett et al. (2011a). This causes many of these searches to result in low identification rates of OHM hosts. Current ongoing efforts to better understand the requirements for a galaxy to produce an OHM are hindered by the small number of known OHMs, frustrating many efforts the isolate the underlying physical conditions of their host galaxies.

Briggs (1998) predicted that, the 18 cm OH line could "spoof" the 21 neutral hydrogen (H I) in untargeted surveys, leading to a unique type of contamination. This can happen undetected when there is no independent redshift of a galaxy, allowing an OHM host to appear to be at a redshift of z_{HI} when the actual redshift is $z_{\mathrm{OH}} = \left(\nu_{\mathrm{OH},0}\left(1+z_{\mathrm{HI}}\right)/\nu_{\mathrm{HI},0}\right) - 1$, where $\nu_{\mathrm{OH},0}$ is the rest frequency of OH (1667 MHz) and $\nu_{\mathrm{HI},0}$ is the rest frequency of H I (1420 MHz). Suess et al. (2016) first demonstrated this possibility by finding five OHMs masquerading as H I sources in the 40% data release of the Arecibo Legacy Fast Arecibo L-Band Feed Array Survey (ALFALFA; Haynes et al. 2018). Roberts et al. (2021) showed that future H I surveys on the Square Kilometre Array (SKA) and its precursors will detect thousands of new OHMs. At high redshifts ($z \gtrapprox 1.5$), the number of OHM detections will actually outnumber H I detections.

While these upcoming new detections will undoubtedly be helpful for further inspection to determine what differentiates OHM hosts from non-masing (U)LIRGs, identification of these sources in H I surveys is expected to be a challenge in itself. These upcoming surveys will be detecting thousands to *hundreds of thousands* of H I galaxies. While some of these galaxies will have existing spectroscopic optical redshifts to allow for effective identification of potential OHMs, many will not.

Roberts et al. (2021) also presented new machine learning methods that can flag potential OHM hosts based on near- to mid-IR photometry when no independent redshift exists.

In this paper, we test these methods on two H I surveys: the full ALFALFA survey (Haynes et al. 2018) and a preliminary catalog using brand new data from Apertif Wide-area Extragalactic Survey (AWES; van Cappellen et al. 2022). This allows these methods to be tested on both legacy data with a large number of sources as well as novel data with premier sensitivity. To carry out the tests of these algorithms, we obtained spectroscopic redshifts from the 3.5m telescope at Apache Point Observatory (APO). These redshifts were used to determine the rest frequency for the observed radio emission line in each galaxy. The results from these verification tests and observations led to revisions in the OHM flagging algorithms presented here, as well as the identification of five new OHMs in ALFALFA. Throughout this work, we assume a flat ΛCDM cosmology with $H_0 = 70$ km s^{-1} Mpc^{-1}, $\Omega_m = 0.3$, and $\Omega_\Lambda = 0.7$.

3.2 Source Selection & Algorithm Revisions

In order to search for previously unidentified OHMs, we applied the algorithm presented in Roberts et al. (2021) to two different H I catalogs, ALFALFA (Haynes et al. 2018) and a preliminary catalog from AWES using Apertif – a phased-array feed for the Westerbork Synthesis Radio Telescope (WSRT; van Cappellen et al. 2022). The ALFALFA catalog consists of ∼31,500 extragalactic H I sources out to redshift $z_{\mathrm{HI}} < 0.06$ (or, if confused with OH, $0.174 < z_{\mathrm{OH}} < 0.244$). ALFALFA's nearly 7,000 deg^2 of sky coverage includes two large areas that cover declinations of 0 to +36 degrees. The preliminary Apertif catalog, constructed using the first 4.5 months of Apertif observations, consists of $\sim$ 1,200 H I sources up to redshift $z_{\mathrm{HI}} < 0.066$ ($0.174 < z_{\mathrm{OH}} < 0.251$), covering declinations of >27 degrees.

Both catalogs were cleaned of sources that had existing spectroscopic redshifts confirming that they were H I sources and then crossmatched with the AllWISE catalog to obtain photometry in the WISE bands W1, W2, and W3 (3.4, 4.6, and 12 μm, respectively). For the ALFALFA catalog, we used a crossmatch radius of 10" from the optical counterpart listed in their catalog. Due to

Arecibo's large L-band beam size, some of these optical counterparts are found to be incorrectly identified, and for those sources we later investigated WISE crossmatches in a radius of 30" from the beam center of each detection. For the Apertif catalog, we crossmatch each of the detected lines to the AllWISE catalog with a search radius of 10" due to the smaller beam size. Roberts et al. (2021) presents two algorithms for flagging potential OHMs using WISE photometry: one that requires data from the W1 and W2 bands (W1-W2 algorithm) and one that requires data from the W1, W2, and W3 bands (W1-W2-W3 algorithm). The first algorithm was applied to the sources in the crossmatched catalogs with SNR > 5 for bands W1 and W2. The second algorithm was applied to sources with SNR > 5 for bands W1, W2, and W3. We apply the algorithms to their respective catalogs and for each source, this outputs the percentage likelihood that it is a misidentified OHM. We chose our starting sample catalog as those that have a 90% likelihood or higher of being an OHM. The process of this selection is illustrated in Figure 3.1.

Using one of the original algorithms from Roberts et al. (2021), as opposed to the new algorithms presented above, we identified a sample of 295 potential OHMs from the ALFALFA catalog. Although OHMs masquerade as sources H I in untargeted catalogs, a 1% contamination rate for a large nearby survey would be much too high. These methods have high false positive rates – this is due to the fact that we have a limited number of known OHMs, so it is unlikely that we could capture the full range of their diversity using the known sample, and these methods were designed to not miss any potential OHMs, so the high false positive rate is a trade-off for the low false negative rate.

Once we had these initial catalogs, we performed a visual inspection of the sources flagged as potential OHMs for both the ALFALFA and Apertif catalogs using optical images from both the Sloan Digitial Sky Survey (SDSS; Stoughton et al. 2002) and the first data release from the Panoramic Survey Telescope and Rapid Response System (Pan-STARRS; Chambers et al. 2016). These images are useful for inspecting the morphology of our starting catalog; OHMs are found in major galaxy mergers, so sources with undisturbed morphology are unlikely to house OHMs and can quickly be ruled out. These initial catalogs generated from the original algorithms from Roberts

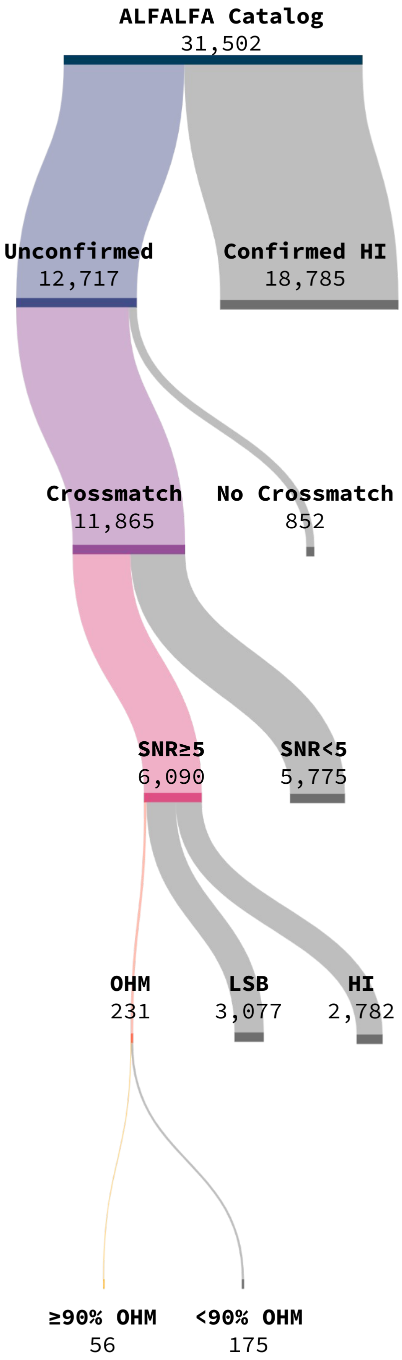

Figure 3.1 Sankey diagram showing an example of how sources previously identified as H I sources were selected for inspection to determine if they are misidentified OHMs. This diagram shows an example using the ALFALFA survey as input catalog and the results from the updated W1-W2-W3 algorithm that categorizes sources as “typical” brightness H I sources (H I), low surface brightness H I sources (LSB), or potential OHMs. From the potential OHM category, we primarily selected sources that have been classified with 90% or greater likelihood of being an OHM.

et al. (2021) included some good examples of potential mergers or disturbed galaxies, but an initial downfall that was quickly identified was the inclusion of low surface brightness (LSB) galaxies in the sample that was flagged as potential OHMs. LSB galaxies are a common but difficult-to-identify class of galaxies that have central surface brightnesses fainter than the night sky by at least one magnitude (Impey & Bothun 1997). They are often defined by their B-band surface brightness being fainter than a certain threshold $\mu_B \geq \sim 22 - 23$ mag arcsec^{-2}. In optical images, they are markedly differentiated from OHM hosts because they are faint and diffuse. However, despite having low star formation rates, they are gas-rich and much more easily detectable by their H I emission than by their optical properties (Du et al. 2015). Although the exact reason the original methods from Roberts et al. (2021) were inadvertently flagging LSB galaxies is unclear, it is likely due to a number of reasons, including that LSB galaxies are incredibly abundant – they may account for up to *half* of all local galaxies (Hodges-Kluck et al. 2020) – and that they have markedly lower star formation rates than the typical H I emitter.

Although LSB galaxies are interesting in their own right, the methods from Roberts et al. (2021) were updated to properly account for and omit these sources in the OHM flagging algorithms. This was done by first creating a catalog of LSB galaxies with SDSS spectroscopic redshifts in ALFALFA using SDSS DR16 g- and r-band photometry to calculate the surface brightness of each galaxy using the formulation presented in Du et al. (2015):

$$\mu_0 = m + 2.5 \log_{10}(2\pi r^2 q) - 10 \log_{10}(1 + z) \tag{3.1}$$

$$\mu_0(B) = \mu_0(g) + 0.47(\mu_0(g) - \mu_0(r)) + 0.17 \tag{3.2}$$

where m refers to the apparent magnitude of the relevant band, r is the on-sky radius of the galaxy, q is the axis ratio, and z is the SDSS spectroscopic redshift. For the on-sky radius of the galaxy, we used the Petrosian radius fit to the r-band image in the SDSS pipeline and for the axis ratio, we calculated it using the de Vaucouleurs ellipticity, $\varepsilon_{\mathrm{dV}}$, fit to the r-band image where $q = 1 - \varepsilon_{\mathrm{dV}}$. Since we used the Petrosian radius, we also used the Petrosian magnitude to calculate the individual surface brightnesses for the g- and r-bands as well. For all the values used from the SDSS catalog, we require a SNR of 10 for each to rule out any poor fits, but we still expect these surface brightness values to be an approximation due to using pipeline-fit parameters. However, this should not be of major concern since the purpose is to roughly flag galaxies with low surface brightness (star formation) and separately identify those from the higher star formation H I and OHM hosts. A histogram of the B-band surface brightness values is shown in Figure 3.2. To select the sources that are considered LSB galaxies, we imposed a generous cut of $\mu_0(B) \geq 23.5$ mag arcsec^{-2} to ensure that we are well within the LSB galaxy parameter space.

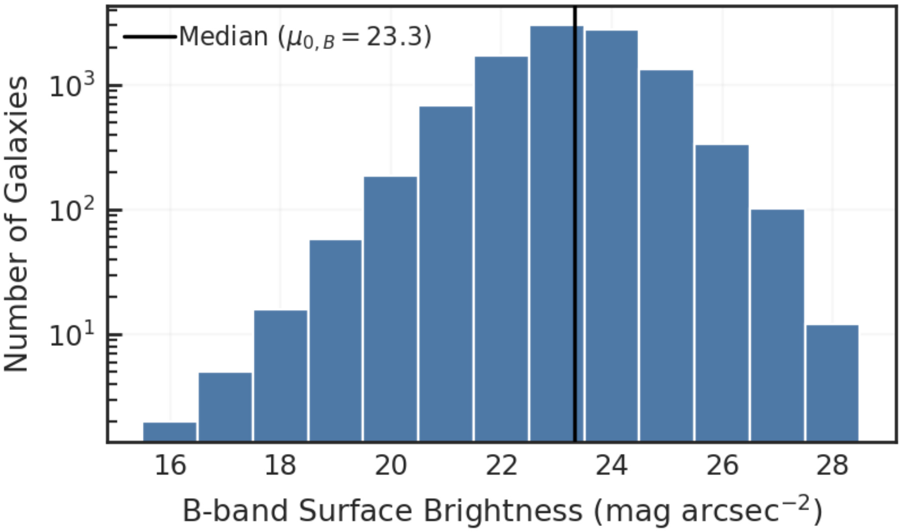

Figure 3.2 Histogram of fit B-band surface brightnesses for the sample of ALFALFA galaxies that could be fit. The median value is marked with a vertical solid line.

Now that we had a sample of non-LSB H I emitters, LSB H I emitters, and OHM hosts, we followed a nearly identical process to that described in Roberts et al. 2021 to recreate the W1-W2 and W1-W2-W3 algorithms to flag potential OH sources in untargeted H I surveys. However, this time, instead of assigning sources one of just two classifications, we now assign them one of three. To do this, we employ a one-vs-all (OVA) classification scheme (Rifkin & Klautau 2004) – this works by iterating through all classes and then fitting that class against all sources not in that class. This differs from a one-vs-one (OVO) classification scheme, which constructs classifiers for each pair of classifiers. We chose the OVA classification scheme because it is simple to interpret, each source is assigned a likelihood of belonging to each class, and it is computationally efficient. We also ran tests fitting with both classification schemes and the OVA classification scheme yielded a higher OH recall (i.e., less false negatives). The obvious issue with either of these schemes is that these sources are not just one classification: The LSB galaxies are, in fact, H I emitters, and OHMs can also produce H I emission lines. However, this simplification of splitting these into three discrete groups is helpful in creating a weighting scheme to determine sources that are potential OHMs. Future work in this area will certainly require a much more careful examination of how to classify these sources, but that will be made much more feasible with the discovery of more OHMs with more diverse properties.

These adapted algorithms were applied to the ALFALFA-WISE and Apertif-WISE catalogs to flag potential OHMs, as previously described with the original algorithms, which yielded 275 sources flagged as high-confidence OHMs for the W1-W2 algorithm and 56 sources for the W1-W2-W3 algorithm. Figure 3.1 shows how, starting from the original ALFALFA catalog, we selected down to this sample for the W1-W2-W3. Our starting sample for observation was pulled from these two pools; however, since these observations took place over 13 months, when sources were found to be an OHM or H I source, we fed those data back into the algorithms with the correct labels, which improves but potentially changes the classification assigned to a given source. Therefore, some sources were added or removed from the observing pool at different times as more information was added. All observed sources were, at some time, classified as high-likelihood OHMs but not necessarily *always* classified as high-likelihood OHMs. This iterative process allows this method to adapt and improve as more OHMs are discovered or even if we find more examples of where OHMs are not found.

3.3 Observations & Data Reduction

To determine whether a given source was a misidentified OHM rather than an H I emitter, we observed our candidates to independently determine their spectroscopic redshift using optical emission lines. This was done using the Dual Imaging Spectrograph (DIS) on the 3.5m telescope at Apache Point Observatory (APO) over 12 half-nights from December 2020 to December 2021. DIS is a medium-dispersion spectrograph with separate red and blue channels. Our setup consisted of the R300/B400 gratings in the red and blue channels, respectively, with central wavelengths of 7500/4400 Å and approximate dispersions of Å pixel^{-1} spanning over 2000 pixels each. The corresponding resolving power for is R$\sim$3250 for the red channel and R$\sim$2400 for the blue channel.

Each night, we calibrated our data with bias frames, flat frames taken using a bright quartz lamp, and two wavelength calibrators: a Helium-Neon-Argon (HeNeAr) lamp for coarse calibration and then night sky lines for finer calibration. This calibration yielded uncertainties of $\lesssim 0.73$ Å and $\lesssim 0.35$ Å for the red and blue sides, respectively, but varied each night based on CCD fringing or observing conditions. As we only aimed to determine the redshift of each source, no flux calibrations were taken, and therefore we only report observed wavelengths of lines but not their fluxes. For each potential OHM, we took one to four five-minute exposures, depending on the brightness of each source. Some objects were revisited on multiple nights due to intermittent clouds or poor atmospheric stability.

Data reduction was done using the IRAF 'longslit' package – an overview of this process for a given night of observations is as follows with the corresponding `iraf` task in parentheses:

(1) Create master bias and flat images using biases and flats taken at the beginning or end of the night. (`zerocombine`, `flatcombine`, `response`)

(2) Trim, debias, and flatten the science images using the master flat and bias images. (`ccdproc`)

(3) Wavelength calibrate the science images using HeNeAr images. (`identify`, `reidentify`, `fitcoords`,`transform`)

(4) For each object, average all their science images. (`imcombine`)

(5) Wavelength calibrate the averaged science images using the skylines visible in the science images. The skylines we used for calibrations were selected to be in a source-free section of the image. (`identify`, `reidentify`, `fitcoords`, `transform`)

(6) Remove skylines. (`background`)

(7) Extract the spectrum from each combined science image, identify emission lines, and fit a Gaussian to each. (`splot`)

Although our main objective was to identify Hα (6563 Å) in each spectrum, the typical spectrum had three to five emission lines, such as those of the [NII] doublet (6549 and 6583 Å) or the [SII] doublet (6717 and 6731 Å). Figure 3.3 shows an example spectrum with all five of these lines and our fits to each for one of our objects. For some objects, the Hβ (4861 Å) and two [OIII] lines (4959 and 5007 Å) could be found on the blue side, but due to significant fringing and reduced sensitivity in the blue channel optics, we do not rely on these measurements for redshift calculation. The measured RMS noise for each target was calculated from source-free regions of the spectrum and we required SNR$\geq$ 5 for the Hα emission line, but the typical values were SNR$\geq$ 20.

The presented optical redshifts are calculated only on the basis of the Hα emission because it has significantly higher SNR and smaller measurement errors. Other emission lines were used to confirm agreement with Hα, but due to blending and being much fainter, the [NII] and [SII] lines had much higher uncertainties and inflated the uncertainty on the redshift measurement. For a small number of sources, only the Hα line is detected, and, for these sources, we present only optical redshift measurements if it is in good agreement with the presumed H I or OH redshift. Hα measurement uncertainties range from 0.001 to 0.12 Å with a median value of $\sim$ 0.016 Å. Adding the maximum calibration uncertainty (0.73 Å for the red side of the spectrum) in quadrature with the maximum measurement uncertainty (0.12Å) yields a maximum uncertainty of 0.74 Å, corresponding to a maximum redshift uncertainty of 1.1×10^{-4}. While many of our optical redshift measurements have errors much lower than this, we adopted this as the uncertainty for all our measured optical redshifts.

3.4 Results & Analysis

Each source we observed yielded one of four results:

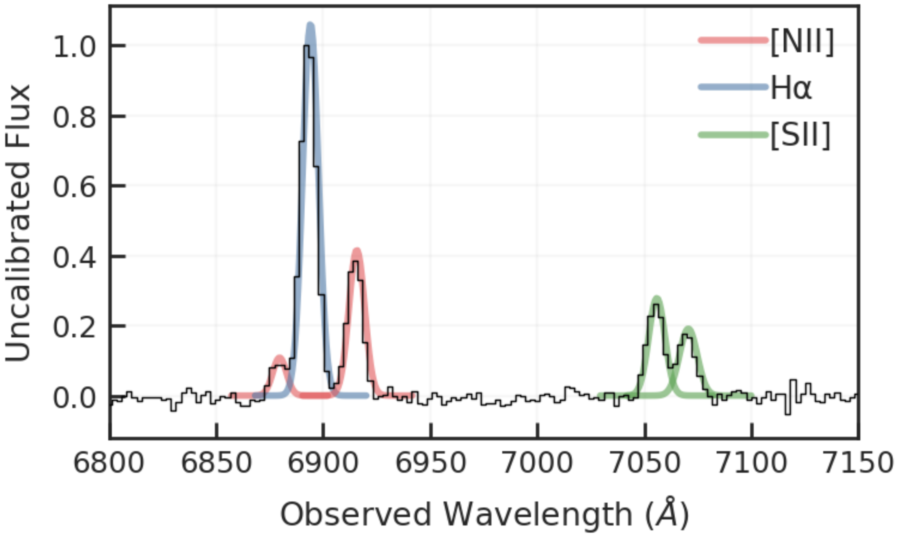

Figure 3.3 The observed optical spectrum (black) of AGC 720264, demonstrating what the typical red-channel spectrum looks like for our selected targets. The fits to each line are also shown as the thicker, colored lines.

1. The source was correctly identified as an H I *emitter.* This determination was made when the measured optical redshift coincided within uncertainty with the redshift calculated by assuming that the detected radio spectral line is H I ($z_{\rm HI}$).

2. The source was incorrectly identified and the reported spectral line is actually OH. This determination was made when the optical redshift matched within uncertainty to the redshift calculated by assuming that the detected radio spectral line is OH ($z_{\rm OH}$). These sources are new OHM discoveries that had masqueraded as H I sources. Converting from $z_{\rm HI}$ to $z_{\rm OH}$ is done using the following equation, where the H I rest frequency ($\nu_{\rm HI,0}$) is 1420.405752 MHz and the OH rest frequency ($\nu_{\rm OH,0}$) is 1667.35903 MHz:

$$z_{\rm OH} = \frac{\nu_{\rm OH,0}}{\nu_{\rm HI,0}}(1 + z_{\rm HI}) - 1. \tag{3.3}$$

3. The source's optical redshift did not match either the H I *or the OH redshift.* These cases are likely the result of false positive radio spectral line detection, or the optical counterpart to the radio line has not yet been identified.

4. The optical source did not produce identifiable emission lines Some sources, even after long integration times, did not produce identifiable optical emission lines that could be used to determine the redshift. It is possible that some of these sources are incorrectly identified optical components that had a higher redshift than could be measured by our observing setup and thus actually belong to group 3 above, but a more specific determination could not be made.

The results of our observation campaign are presented in Appendix A with individual line measurements presented in Table A.3. In total, we observed 142 optical objects associated with 120 radio emission line sources. Of these optical sources, 35 were associated with radio emission lines from Apertif and 107 were associated with lines from ALFALFA.

3.4.1 H I Confirmations & Ambiguous Sources

Our observations confirmed 78 H I sources – 25 from Apertif and 53 from ALFALFA. These sources are presented in Table A.1 along with the corresponding optical positions associated with the matching redshift. For sources from the ALFALFA catalog, the AGC number is provided. Optical positions were determined using SDSS DR9 images, as well as telescope-pointing images while observing.

Table A.2 presents the optical sources that were observed where no determination could be made, either because they lacked optical emission lines to determine a redshift or because their optical redshift matched neither the expected OH nor H I redshift. Since multiple optical sources could correspond with the radio emission line due to large beam sizes, these 60 optical sources correspond to 46 radio sources. Broken down by survey, 10 optical sources were observed corresponding to 8 radio emission lines from Apertif, and 50 optical sources were observed corresponding to 38 radio emission lines from ALFALFA. In total, 17 optical sources were found to have redshifts that did not correspond to the expected H I or OH redshift. For another 43 sources, no redshift could be measured from their spectrum.

3.4.2 OH Detections

Our observations yielded four OHM detections, all found in the ALFALFA catalog. We originally planned on observing AGC 193884; however, an optical redshift had already been obtained by SDSS that confirms that it hosts an OHM. We present the confirmation of five new OHMs and their properties in Table 3.1. As all five are from the ALFALFA catalog, the flux and line width are from Haynes et al. (2018) are used to calculate the OH luminosity using the following equation:

$$L_{\rm OH} = 4\pi D_L^2 \, \frac{\nu_{\rm OH,0}}{c\,(1+z)} \, F, \tag{3.4}$$

where $\nu_{\rm OH,0}$ is the rest frequency of the OH line (1667.35903 MHz), D_L is the luminosity distance and F is the line flux in Jy km s^{-1}.

Haynes et al. (2018) presents 9 confirmed OHM detections – some confirmed using SDSS redshifts and some previously identified by Suess et al. (2016), Morganti et al. (2006), and Darling & Giovanelli (2002a) – and 10 OHM candidates, that require confirmation. We observed three of the OHM candidates that they presented and confirm that one of them was an OHM (AGC 249507 – see Table 3.1). For the other two OHM candidates we observed, AGC 749309 and 219835, the optical source of these emission lines could not be identified, and they remain ambiguous hosts. Together with the 9 confirmed OHMs from Haynes et al. (2018), this brings the total number of OHM detections in ALFALFA to 16.

The number of OHMs predicted to be found in ALFALFA has varied: Giovanelli et al. (2005) predicted that ALFALFA would detect a few dozen OHMs, while Suess et al. (2016) extrapolated the number of OHMs detected in the ALFALFA 40% data release to predict that roughly 15 total new OHMs would be detected throughout the ALFALFA survey.

Now with complete ALFALFA survey parameters, we can integrate over the updated Markov chain Monte Carlo (MCMC) fit to the OH luminosity function (OHLF) from Roberts et al. (2021) to calculate the number of OHMs predicted to be detected by ALFALFA. We use the ALFALFA survey parameters from Haynes et al. (2018): we use a frequency range of 1435-1350 MHz[1] ($z_{\rm OH}$=0.162–0.235), 5σ survey sensitivity of 0.72 Jy km s^{-1} for W_{50} = 200 km s^{-1}, and sky coverage of almost 7,000 deg^2 to obtain a predicted total number of OHM detections of $N_{\rm OH} = 35.8^{+6.6}_{-6.5}$. The difference between the predicted value and the discovered number can be explained by further impacts of RFI, possible mismatches of radio emission to optical sources, and other potentially missed OHM sources.

We cannot calculate the expected number of OHM detections in the preliminary Apertif catalog using this method, as the observations are only partially complete. However, we can use the expected OH contamination rate for Apertif of $0.09^{+0.02}_{-0.01}$% from Roberts et al. (2021) and apply it to our catalog of ∼1,200 sources. This gives an expected number of OHM detections for the preliminary catalog of $1.08^{+0.24}_{-0.12}$ detections. With the detection of IRAS 10597+5926, presented in Hess et al. (2021), our result of finding no more OH sources in the preliminary catalog is consistent with the expected contamination rate.

---

[1] The full frequency coverage of ALFALFA is 1435-1335 MHz. However, as noted in Haynes et al. (2018), ALFALFA suffers from significant radio frequency interference below 1350 MHz and volume completeness studies should only be restricted to those corresponding to radio frequencies > 1350 MHz.

Table 3.1. OH line properties of new OHM confirmations

AGC	Optical Position (J2000)	$z_{\rm opt}$	OH Line Flux (Jy km s^{-1})	Line Width (km s^{-1})	log $L_{\rm OH}$ (L$_\odot$)
102299	003924.7+260414.4	0.20310	0.57	59	2.91
116345	011604.0+110136.6	0.20509	1.36	206	3.30
193884	093238.3+161157.0	0.19095[a]	1.96	387	3.39
249507[b]	140340.3+295456.0	0.17862	1.65	216	3.26
322050	221306.3+011627.0	0.18435	2.46	373	3.46

[a] This redshift was provided by SDSS.

[b] This source was first theorized to be an OHM in Haynes et al. (2018) but had not yet been confirmed.

Note. — Flux and line width values are from Haynes et al. (2018) and are used to calculate OH luminosity.

3.5 Conclusion

In this work, we tested the OHM flagging methods presented in Roberts et al. (2021) on both existing H I survey data from ALFALFA and new survey data from AWES. Through these tests, we identified an initial shortcoming of these methods is their tendency to flag LSB galaxies as potential OHMs. These methods were updated to flag potential OHM hosts, accounting for the large number of LSB galaxies in H I survey data. For these potential OHM hosts flagged in H I surveys, we obtain longslit optical spectra in order to determine the rest frequency of the radio emission line detected in each source. In total, we obtained 142 optical spectra, confirming H I emission in 78 galaxies. For 60 of these spectra, the results were ambiguous, where either a redshift was unable to be determined or the measured redshift did not match the inferred redshift from the H I or OH line. Lastly, we were able to identify five new OHMs previously thought to be H I sources in ALFALFA data. These sources verify the ability of our algorithms to successfully identify potential OHM hosts that were interloping in H I survey data.

These methods will continue to become more accurate as new OHMs are identified. As discussed in this chapter, these methods are able to easily adapt to new sources that are fed into it. For a fraction of the new OHMs that will be detected in next-generation H I surveys, existing optical redshifts will be crucial for fast OHM identification and then used to further strengthen these algorithms for sources without existing redshifts. The future of OHM science will be driven by these detections in H I surveys.

Acknowledgements

This work has been supported by the National Science Foundation through grant AST-1814648, as well as the National Radio Astronomy Observatory. This research has made use of the NASA/IPAC Extragalactic Database (NED), which is funded by the National Aeronautics and Space Administration and operated by the California Institute of Technology.

Chapter 4

A Glimpse at the Future of OH Megamaser Discoveries

Preface

Chapter 2, reproduced from Roberts et al. (2021), introduced new forecasts for the number of OHMs that will be discovered by next-generation H I surveys and presented methods for flagging these potential interlopers. Chapter 3 presented results from testing these methods that validated their ability to uncover OHMs masquerading as H I sources by finding five new OHMs in ALFALFA. However, the predictions of Chapter 2 foretold of a brand new OHM discovery space populated by an order of magnitude new sources at redshifts never before seen in the field. The H I surveys that will usher in this future of discovery are currently underway, and some are still in very preliminary stages. Still, this has not prevented some early groundbreaking discoveries. In this chapter, I present two of these detections that preview the soon-burgeoning field of OHM science. These detections highlight how the increased sensitivity and bandwidth of these surveys will allow for detailed, high quality measurements as shown in Section 4.1 as well as record-breaking detections of OHMs at unprecedented redshifts as shown in Section 4.2.

Section 4.1 is a brief summary of a paper originally published in the March 2021 issue of *Astronomy & Astrophysics* (Volume 647, id.A193) as Hess et al. (2021) of which I am the second author. My contributions included the predictions for the number of OHM and OH satellite line detections, assistance in analysis of the IR properties of the host galaxy, and other background information about OHMs and their hosts. Section 4.2 is a brief summary of a paper originally published in the May 2022 issue of Astrophysical Journal Letters (Volume 931, Issue 1, id.L7) as Glowacki et al. (2022), where I was a co-author as well. My contributions include creation of Figures 4.1 and 4.2, discussion of how this detection fares in our OHM flagging methods, and other information on the broader context of this OHM detection. Both papers are summarized here to highlight this exciting future of OHM science, however full details can be found in the full print versions of each paper.

4.1 The Future of High Quality OH Megamaser Detections

Hess et al. (2021) presented the serendipitous detection of the two main OH maser lines in IRAS 10597+5926 at $z_{\odot} = 0.19612$ in the untargeted Apertif Wide-area Extragalactic Survey (AWES) on the Westerbork Synthesis Radio Telescope. While this source was first identified as an OHM by Willett (2012), the detection by Apertif was able to place an upper limit on the 1612 MHz satellite line, making this one of the only a handful of OHMs with satellite line constraints.

In addition, we presented predictions for the number of OHMs and satellite OH lines that will be detected with AWES for a number of potential survey plans, showing that $\sim 1-7$ more satellite line detections are expected for AWES alone. Furthermore, current and future H I surveys on SKA precursors will also be sensitive to these satellite lines, drastically increasing the number of OHMs with satellite line detections. These measurements will be helpful for constraining the gas content of OHMs – an important step towards the goal of understanding these unusual host galaxies.

4.2 The Future of Record-Breaking OH Megamaser Detections

As discussed in Chapter 2, LADUMA (Looking at the Distant Universe with the MeerKAT Array) is a deep H I survey on the MeerKAT Array, an SKA precursor. We reported the first untargeted detection of an OHM at $z > 0.5$, LADUMA J033046.20−275518.1 (nicknamed “Nkalakatha”) in Glowacki et al. (2022). LADUMA J033046.20−275518.1 has an optical redshift of $z = 0.52$, which shattered the record for highest redshift OHM. The previous record holder for nearly 30 years was IRAS 17208−0014 at a redshift of $z = 0.265$ (Baan et al. 1992a). The full details of this detection can be found in the full print version of this paper.

In Glowacki et al. (2022), we also investigated how this detection compares to the OHM flagging methods in Chapter 2. Figure 4.1 shows this source overlaid on the predicted distribution of OH and H I source WISE magnitudes and colors at the relevant redshift ($z_{\rm OH} \sim 0.52$). In the left panel, this source lies within confidence intervals for both OH and H I, however it is in a much higher confidence interval for OH than H I. In the right panel, this source is completely omitted from the H I confidence interval. Despite these OHM flagging methods being based on a limited OHM population, these results indicate that they are still able to successfully flag potential OHM hosts.

Lastly, we discussed how this source compares with other known OHMs. Figure 4.2 shows this source (green star) compared to other known OHMs, including IRAS 10597+5926 (purple plus), the source discussed in the previous section. Further discussion of this plot can be found in the full text version of this paper and an updated version with more information is presented in Chapter 6.

4.3 Conclusion

This chapter introduces two OHM detections that highlight the changing landscape of OHM science. However, these are only the beginning. Current and future H I surveys will detect OHMs that will continually break redshift records and provide more information on their respective host galaxies than ever before. These detections will be crucial for both understanding the underlying OHM population and implementing OHMs as tracers of major galaxy mergers and extreme star formation.

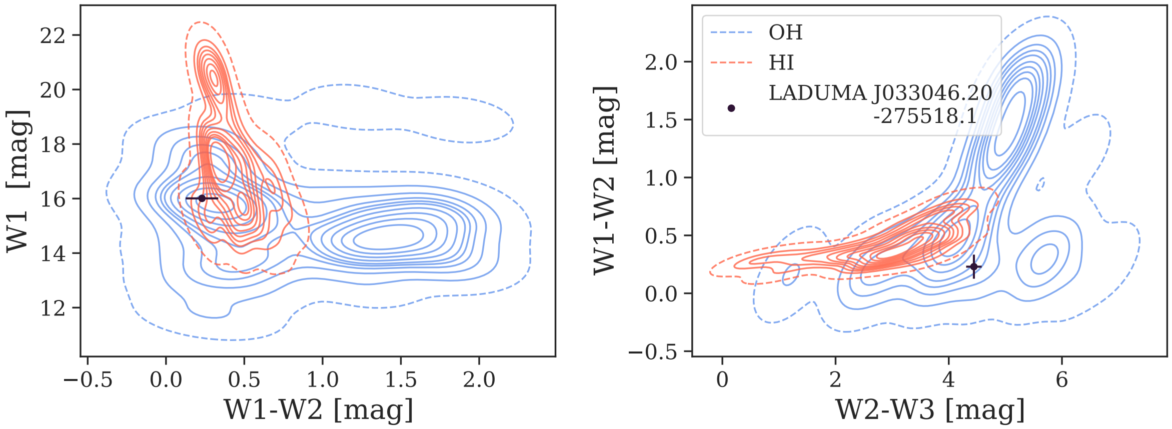

Figure 4.1 Predicted distributions of gas-rich mergers traced by OH at $z_{\mathrm{OH}} \sim 0.52$ (blue), and H I-rich disk galaxies at $z_{\mathrm{H\,I}} \sim 0.30$ (red), in WISE color-magnitude and color-color space, generated using algorithms presented in Roberts et al. (2021). Contours enclose the upper 99% (dashed), 90%, 80%,... 20%, and 10% of the Gaussian kernel density estimates for the respective galaxy distributions. In the left panel, both OH and H I identifications are supported for LADUMA J033046.20−275518.1, while in the right panel, OH is clearly preferred. Figure originally from Glowacki et al. (2022).

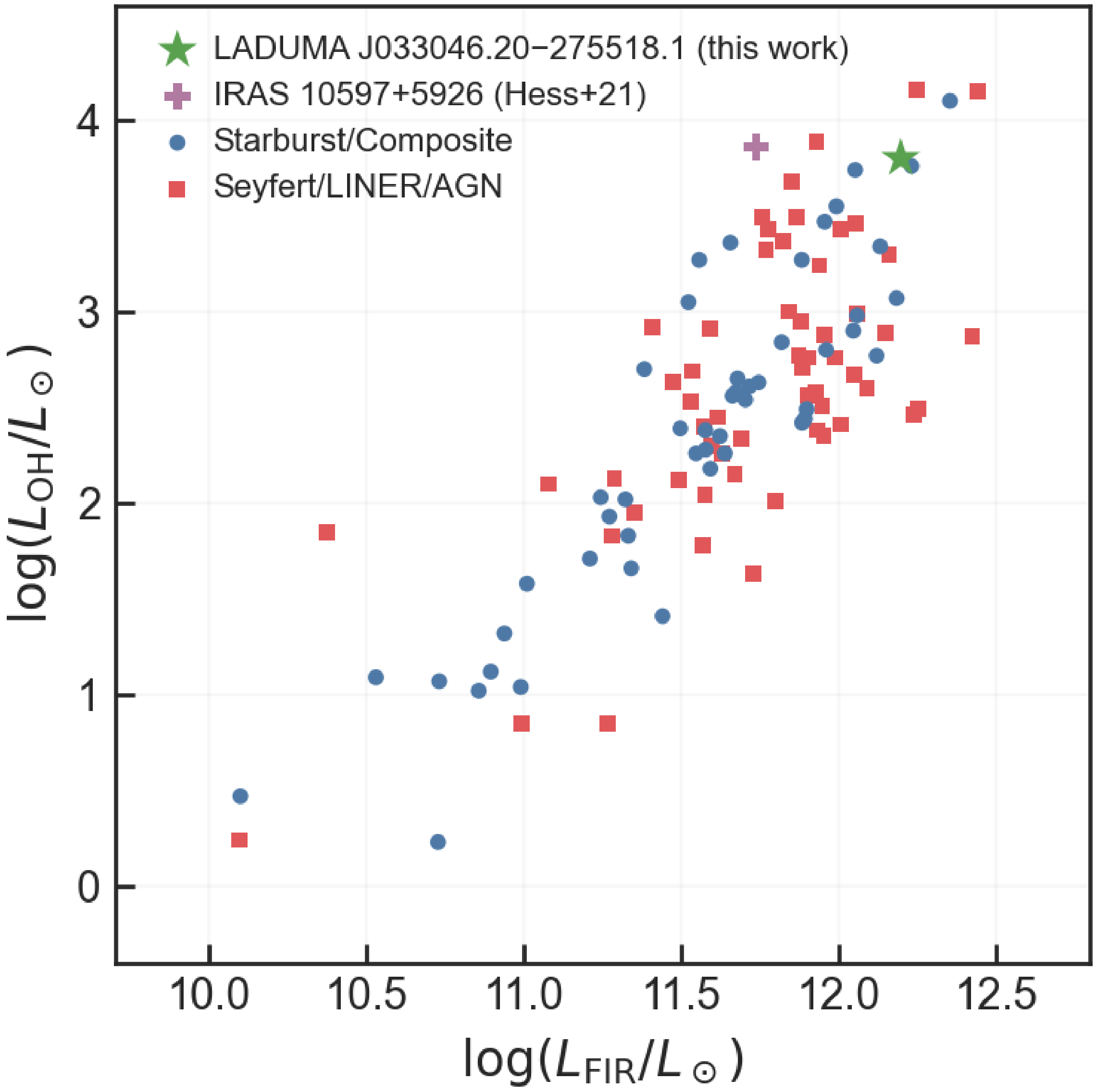

Figure 4.2 L_{OH} vs. L_{FIR} for known OHMs (Roberts et al. 2023, in preparation; also see Chapter 6). LADUMA J033046.20−275518.1 (green star) is one of the most luminous OHMs on both axes. Figure originally from Glowacki et al. (2022).

Chapter 5

What are the Ingredients of an OH Megamaser?

Preface

The rapidly approaching future of OHM discoveries is exciting and will facilitate a new era of science unlocked by these science-rich sources. However, enabling the full potential of OHMs requires understanding what drives a major merger to produce an OHM. Darling (2007) proposed the dense gas trigger hypothesis, which showed that OHM hosts tend to have markedly higher dense gas fractions than their non-masing counterparts. Here, we take a closer look at this hypothesis with a sample size that is three times larger than the original sample from Darling (2007), and demonstrate that this hypothesis fails to separate OHMs and non-masing (U)LIRGs in a diversified population. Further, we discuss other tests of the dense gas fraction hypothesis and present challenges in current methods for measuring dense gas in OHM hosts.

This work is still in progress and observations are still underway. In this chapter, I present the progress that has been made on understanding the underlying physical conditions of OHMs, but the implications of this work and the data are still coming into focus. Any conclusions stated in or drawn from this chapter should be considered preliminary.

5.1 Introduction

OH megamasers (OHMs) are 18 cm masers produced by major galaxy mergers with isotropic line luminosities of $L_{\rm OH} \geq 10\,L_\odot$. OHMs with line luminosities of $L_{\rm OH} \geq 10^4\,L_\odot$ are referred to as OH *giga*masers (but the distinction is arbitrary). These are rare phenomena that, up to today, have been found in only ∼120 galaxies and predominantly at redshifts less than $z = 0.265$. OHM host galaxies are (ultra-)luminous infrared galaxies ([U]LIRGs) and are markers of some of the most extreme star formation in our universe (Lockett & Elitzur 2008) with OH maser emission being indicative of potential molecular outflows (Gowardhan et al. 2018). Though currently rare and known only at limited redshifts, understanding these sources will eventually allow us to study what role extreme star formation plays in galaxy evolution, particularly as we enter the next era of radio astronomy with the Square Kilometre Array (SKA) and its precursors which will be uncovering hundreds (even *thousands*, Roberts et al. 2021) more OHMs. This is demonstrated by the incredibly recent discovery of the new, highest redshift OHM (Glowacki et al. 2022) at a redshift of $z = 0.52$, breaking the previous record of $z = 0.265$ which held the title as the most distant OHM since 1992. Furthermore, as OHMs are found in late-stage major galaxy mergers, they can independently constrain the major merger rate. They have also been used as in-situ magnetometers via observations of Zeeman splitting (Robishaw et al. 2008; McBride et al. 2014). These intense properties and correlation with galaxy mergers make OHMs valuable tracers of extreme star formation and galaxy evolution.

However, despite OHM hosts being (U)LIRGs, ∼80% of (U)LIRGs show no OHM activity. What distinguishes masing from non-masing (U)LIRGs is still an open question. Theoretical modeling of OHM formation by Parra et al. (2005) showed that OHM structure arises from overlapping low opacity clouds that amplify unsaturated emission. Darling (2007) examined $L_{\mathrm{HCN}}/L_{\mathrm{CO}}$ – a proxy for dense gas fraction where L_{HCN} traces *dense* molecular gas while L_{CO} traces *total* molecular gas (Gao & Solomon 2004a) – for non-masing and masing (U)LIRGs and showed that OHM hosts possess high dense molecular gas fractions compared to their non-masing counterparts. Further, they determined that the clouds responsible for OHM emission must be significantly denser than the mean of the system. This suggests that what steers a major merger on the path of becoming a future OHM host is a high initial gas content being funneled to the center of the system. This is consistent with studies of compact obscured nuclei (CONs) which have been found in a few OHM hosts and whose population shares several traits with the OHM host population, such as strong silicate absorption at 10μm (Falstad et al. 2021; Willett et al. 2011a). However, this dense gas trigger hypothesis has not been tested since Darling (2007) and never on a spatially resolved scale.

Understanding the physical condition and gas content of OHMs is particularly relevant now as many new radio surveys are underway on SKA precursors – surveys which have the ability to detect OHMs (Briggs 1998; Suess et al. 2016) and will do so at an unprecedented rate due to increased sensitivity, redshift limits, and survey coverage (Roberts et al. 2021; Hess et al. 2021; Glowacki et al. 2022). If we wish to employ these newly discovered OHMs as tracers of major mergers and extreme star formation, we need to first understand the physical processes that drive them.

5.2 A Closer Look at the Dense Gas Fraction in OHM Hosts

Identifying the physical mechanism that drives OHM formation in only a small percentage of (U)LIRGs and major galaxy mergers has been an important question in the pursuit to understand OHMs and their broader role in galaxy evolution (e.g. Lo 2005; Parra et al. 2005; Darling 2007; and references therein). Darling (2007) investigated the dense gas fraction in eight OHM hosts and 53 non-masing (U)LIRGs by comparing infrared (IR) luminosity ($L_{\rm IR}$) to the ratio of HCN (1-0) to ^{12}CO (1-0) line luminosities ($L_{\rm HCN}/L_{\rm CO}$; a proxy for dense gas fraction) where $L_{\rm HCN}$ traces *dense* molecular gas while $L_{\rm CO}$ traces *total* molecular gas (Gao & Solomon 2004b). The results from this analysis showed that OHM hosts possess high molecular dense gas fractions compared to their non-masing counterparts (Figure 5.1).

5.2.1 A Test Case: New Observations of IRAS 10597+5926

To further test this hypothesis, we observed IRAS 10597+5926, shown as the green star in Figure 5.3, an OHM host recently detected in the Apertif Wide-area Extragalactic Survey (Hess et al. 2021), with the 30m telescope at IRAM to constrain the dense gas fraction by measuring HCN (1-0) and ^{12}CO (1-0) line luminosities. IRAS 10597+5926 presented a unique opportunity to examine how this dense gas fraction hypothesis applies to OHM hosts that vary from those examined in Darling (2007) since it is at a much higher redshift than the previous sample and hosts

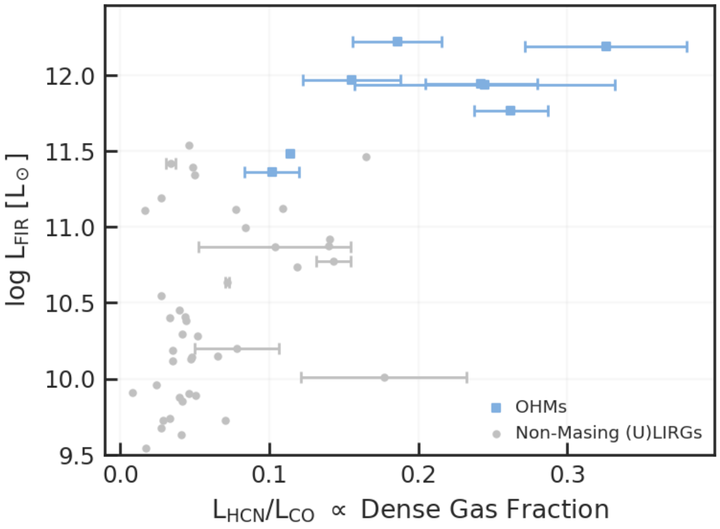

Figure 5.1 Far-IR luminosity versus dense gas fraction ($L_{\mathrm{HCN}}/L_{\mathrm{CO}}$) for the original sources used in Darling (2007). Blue markers indicate OHM hosts and gray markers indicate non-masing (U)LIRGs.

the fourth most luminous OHM ever discovered.

The goal of these observations was to detect and measure HCN (1-0), HCO+ (1-0), ^{12}CO (1-0), and ^{13}CO (1-0) in order to calculate the dense gas fraction of IRAS 10597+5926 and compare to data presented in Darling (2007). We used a wobble observing strategy and obtained a total of 3.38 hours of on-source observing for all four lines using the EMIR (Eight MIxer Receiver) frontend – the bands and their corresponding lines are shown in Table 5.1. The data is comprised of 80 polarized spectra taken over the night, each consisting of roughly 300 seconds on-source observing in two polarizations (horizontal and vertical) – i.e. 40 unpolarized spectra when averaged together. Each of these were averaged together and then baselined using a fourth-order Chebyshev polynomial due to the variation of the atmosphere throughout the night. For the LO band, five of the 40 spectra were removed due to poor quality at this step. The combined spectra for each band were then smoothed using a Gaussian smoothing over 75 channels ($\Delta\nu$ = 14.625 MHz). Gaussian profiles were fit to the HCN (1-0) and ^{12}CO (1-0) lines.

The ^{12}CO (1-0) line is detected in the UO band with an integrated SNR of 11.6 (peak SNR is 7.0), shown in the top panel of Figure 5.2. The observed line center from the fit yields a redshift of

Table 5.1 IRAM band information for observations of IRAS 10597+5926. All bands have a spectral resolution of 0.195 MHz corresponding to 20,737 channels.

Band	**Frequency Range**	**Lines in Band**
LO	73.32–77.37 GHz	HCN (1-0), HCO+ (1-0)
LI	77.05–81.10 GHz	–
UI	89.00–93.05 GHz	^{13}CO (1-0)
UO	92.73–96.78 GHz	^{12}CO (1-0)

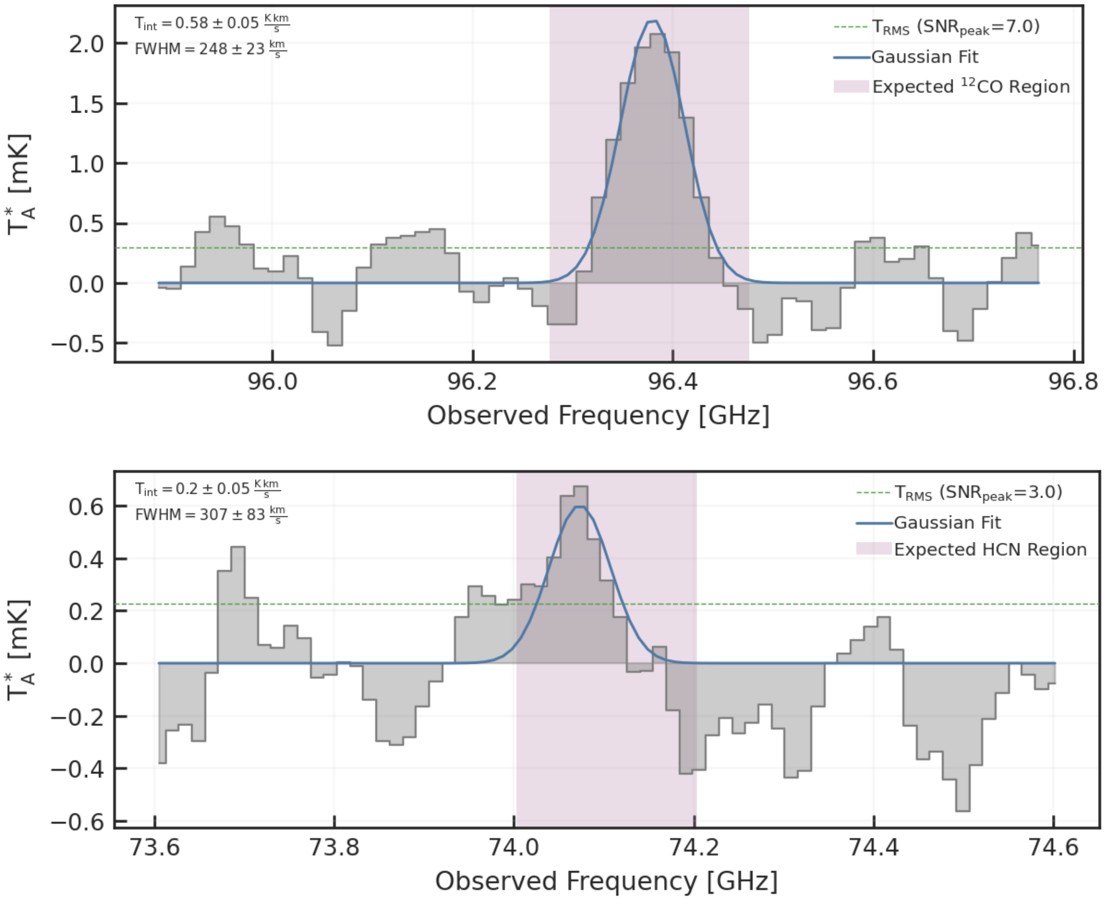

Figure 5.2 ^{12}CO (1-0) (top) and HCN (1-0) (bottom) measurements in IRAS 10597+5926 from the IRAM 30m telescope. The spectrum is shown in grey, the Gaussian fits is shown as the blue line, the RMS level is shown as the green dashed line, and the purple region shows where the line is expected based on redshift.

$z = 0.196024 \pm 0.000006$ which agrees well with the Apertif measured value of $z = 0.19612$ (0.05% difference).

The HCN (1-0) line, shown in the bottom panel of Figure 5.2, is tentatively detected with an integrated SNR of 4.0 (peak SNR is 3.0). The LO band spectrum suffered from significant atmospheric variation throughout the night and increased the expected noise of the band. The fit for this line was bounded within the standard deviation of the ^{12}CO line since the fits tended to be poor when this was not done. Also, these lines are usually observed to have the same widths so this helps exclude the noise on the lower frequency side of the line. The observed line center indicates a redshift of $z = 0.196544 \pm 0.000024$ which slightly offset from the expected value from Apertif but still in decent agreement (0.2% difference).

The HCO+ (1-0) line appears to be lost to a particularly noisy region of the LO band. The UI band shows no indication of the ^{13}CO (1-0) line. This is unsurprising since mergers are expected to have less ^{13}CO than non-merging galaxies (Casoli et al. 1992) but we had attempted a serendipitous detection anyway. We had predicted the ratio of peak temperatures of the ^{12}CO line to the ^{13}CO line to be ~ 11 (Paglione et al. 2001) which yields a peak line temperature for ^{13}CO of ~ 0.2 mK based on our observations. The $\mathrm{T_{rms}}$ of the UI band is 0.22 mK so this line is certainly lost to noise.

Table 5.2 Fit parameters for each line observed in IRAS 10597+5926 with the IRAM 30m telescope.

Parameter	**^{12}CO (1-0)**	**HCN (1-0)**
$\mathrm{T_{int}}$	0.58 ± 0.05 K km/s	0.20 ± 0.05 K km/s
Line Center	96.379 ± 0.003 GHz	74.073 ± 0.009 GHz
Inferred Redshift	0.196024 ± 0.000006	0.196544 ± 0.000024
FWHM	246 ± 24 GHz	304 ± 81 GHz
$\mathrm{T_{rms}}$	0.30 mK	0.23 mK
$\mathrm{T_{rms,theoretical}}$	0.28 mK	0.28 mK

From the main beam temperature, we calculate line luminosity in K km s^{-1} pc^2, denoted by L, from equation (2) from Solomon et al. (1997):

$$L = 23.5\ \Omega_b\ D_L^2\ T_{\mathrm{mb}}\ (1+z)^{-3}, \tag{5.1}$$

where Ω_b is the solid angle of the telescope calculated via

$$\Omega_b = \frac{\pi}{4\ln 2}\theta^2 \approx \frac{\pi}{4\ln 2}\left(\frac{2460''}{\nu\ [\mathrm{GHz}]}\right)^2, \tag{5.2}$$

where the beam size approximation comes from the IRAM wiki.[1] Using these equations and inte-

---

[1] https://publicwiki.iram.es/Iram30mEfficiencies

grated temperature values from Table 5.2, we get the following line luminosity values:

$$L_{\mathrm{HCN}} = (3.55 \pm 0.88) \times 10^9 \text{ K km s}^{-1} \text{ pc}^2$$

$$L_{\mathrm{CO}} = (6.33 \pm 0.57) \times 10^9 \text{ K km s}^{-1} \text{ pc}^2$$

These values seem consistent with those in Gao & Solomon (2004b) and Darling (2007). Calculating dense gas fraction from these values yields:

$$\frac{L_{\mathrm{HCN}}}{L_{\mathrm{CO}}} = 0.56 \pm 0.15$$

This value is over *double* the highest dense gas fraction examined in Darling (2007). These results may seem suspect, but a closer look at the OHM sample in Darling (2007) demonstrates that we have not yet fully explored the OHM parameter space. IRAS 10597+5926 is at a redshift of $z = 0.19612$ and has an OH luminosity of $L_{\mathrm{OH}} = 10^{3.90\pm0.03}\, L_\odot$ (Hess et al. 2021), whereas the sample of eight OHMs in Darling (2007) only reaches redshift $z = 0.064$ and has a maximum OH luminosity of $L_{\mathrm{OH}} = 10^{3.11}\, L_\odot$.

5.2.2 The Full Diversity of the OHM Population

To attempt to fill in these gaps, we did a literature search of HCN (1-0) and ^{12}CO (1-0) measurements of OHM hosts and calculated the dense gas fraction of sources that had both measurements. This expanded our sample from the original eight OHM hosts in Darling (2007) to a total of 21 OHM hosts. New HCN (1-0) measurements were obtained from Baan et al. (2008), Evans et al. (2006), Gao & Solomon (2004b), García-Burillo et al. (2012), Privon et al. (2015), and Solomon et al. (1992). ^{12}CO (1-0) measurements were obtained from Aalto et al. (2002), Baan et al. (2008), Chung et al. (2009), Evans et al. (2006), Gao & Solomon (2004b), García-Burillo et al. (2012), Herrero-Illana et al. (2019), Horellou et al. (1995), and Solomon et al. (1997). New and updated non-masing (U)LIRGs were also included from Baan et al. (2008), Privon et al. (2015), and Herrero-Illana et al. (2019). All luminosities were scaled to a common ΛCDM cosmology with $H_0 = 70$ km s^{-1} Mpc^{-1} and error bars were included when given. Figure 5.3 shows this expanded

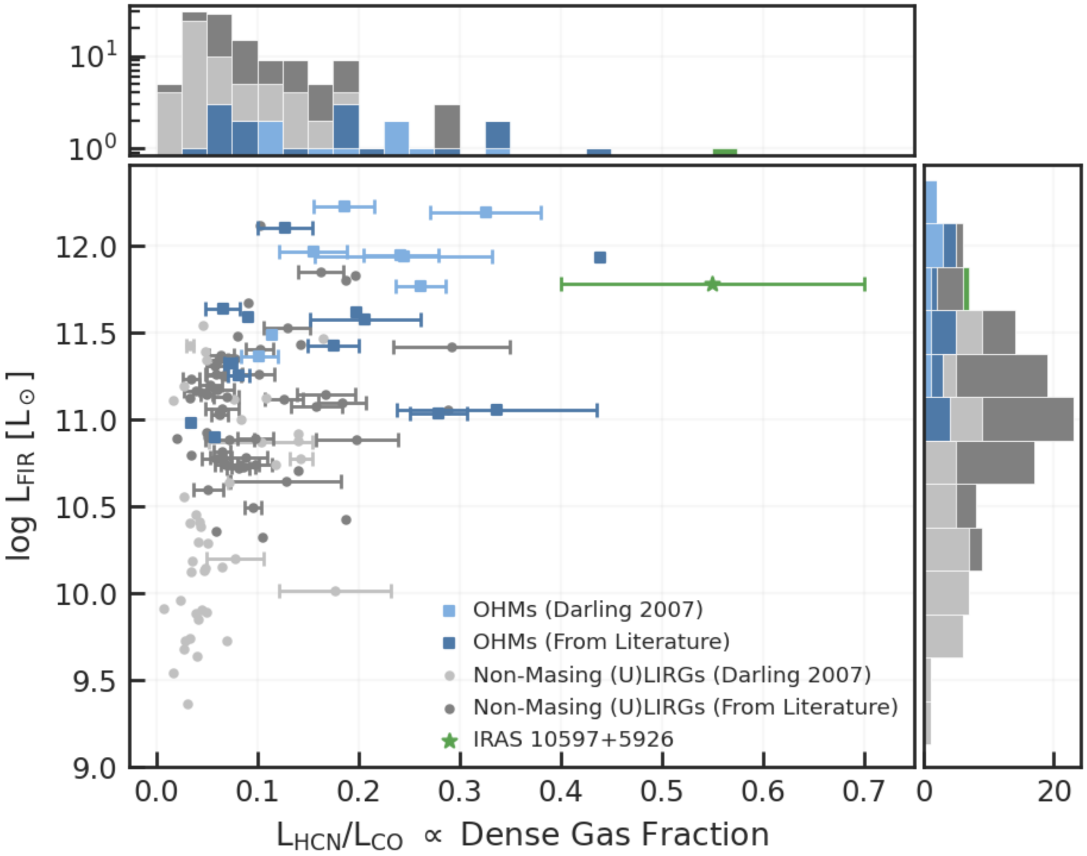

Figure 5.3 Far-IR luminosity versus dense gas fraction ($L_{\mathrm{HCN}}/L_{\mathrm{CO}}$) for an expanded sample of sources. Blue markers indicate OHM hosts and gray markers indicate non-masing (U)LIRGs. Lighter shades of either represent sources original from Darling (2007) and darker shades are those added from the literature. Some sources that are below the threshold for LIRG classification are included for comparison as well.

sample in far-IR luminosity versus dense gas fraction space. Despite this new sample being nearly three times larger than the previous, these data can only demonstrate correlation, not causation. A KS-test on the dense gas fraction values for the OHMs and non-masing (U)LIRGs indicates that these are two separate distributions (p-value=0.0007). However, the subsets of sources that have dense gas fraction measurements are not uniform and many of the dense gas measurements shown in Figure 5.3 are for (U)LIRGs with redshifts of $z \leq 0.01$ where the minimum redshift of the OHM host is $z = 0.0104$. If we limit both samples to a common parameter space ($z \geq 0.01$ and log $L_{\mathrm{FIR}} \geq 10.8$), the probability of rejecting the null hypothesis decreases significantly (p-value=0.038).

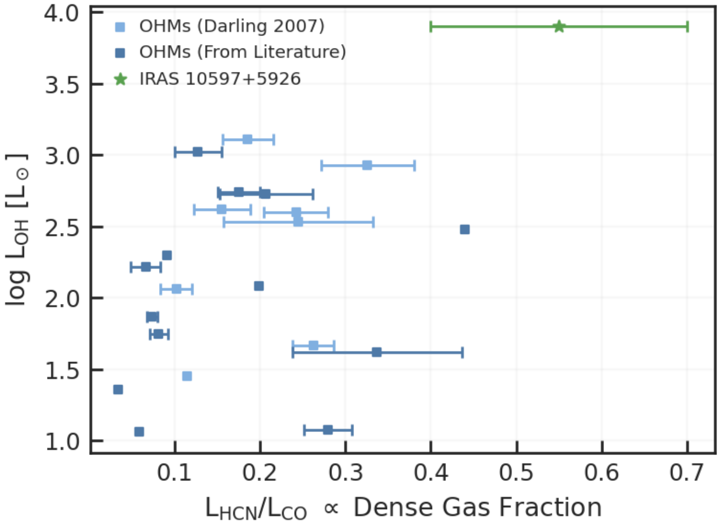

Figure 5.4 OH luminosity versus dense gas fraction for OHMs studied in Darling (2007) and those with data from the literature. Correlation tests indicate there are no correlation between these values (R=0.24, p-value=0.28).

Further, if OHMs are produced galaxies with higher dense gas fractions, then there are two different ways this should manifest in the data. If there is a dense gas fraction threshold where, above which, the requirement is met to create an OHM, then Figure 5.3 should depict this threshold in the histogram in the top panel, but no clear differentiation exists. Or, if OH masing is dependent on the dense gas fraction in a galaxy, then the OH luminosity would be correlated with $L_{\mathrm{HCN}}/L_{\mathrm{CO}}$. Figure 5.4 demonstrates that there is no relationship between $L_{\mathrm{HCN}}/L_{\mathrm{CO}}$and OH luminosity. Measuring the correlation coefficient between these parameters returns a value of R=0.24 with a p-value of 0.28, indicating no correlation.

Despite this new sample being nearly three times larger than the previous one, our redshift limit only increased to $z = 0.078$ and no OHMs with OH luminosities higher than $L_{\mathrm{OH}} = 10^{3.11}\,L_\odot$ have HCN (1-0) measurements. Besides our preliminary detection of HCN (1-0) in IRAS 10597+5926, this means that the physical conditions of OHM hosts at redshifts greater than $z \approx 0.08$ or with OH luminosities higher than $L_{\mathrm{OH}} \gtrsim 10^3\,L_\odot$ (see Figure 5.5) are truly unexplored. Figure 5.6 shows far-IR luminosity versus redshift much larger sample of (U)LIRGs, including masing, non-masing, and unknown hosts. This full sample illustrates how limited the existing dense gas data

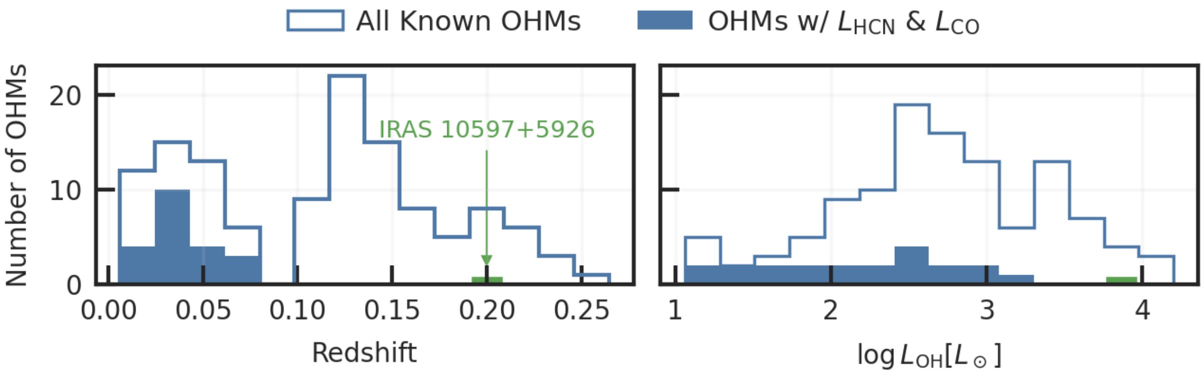

Figure 5.5 Histograms demonstrating the dearth of L_{HCN} and L_{CO} data for a diverse sample of OHMs. Unfilled histograms represent all OHMs while filled histograms represent only those with dense gas fraction measurements. The redshift histogram omits the recent OHM detection by LADUMA at $z = 0.52$. IRAS 10597+5926 is indicated by the green bar.

is for not just OHMs, but (U)LIRGs in general. The remarkably high dense gas fraction in IRAS 10597+5926 has a large uncertainty, but it may be a clue about the physical conditions in the most luminous OHMs. If we intend to use OHMs to understand the most extreme regions of our universe and their impact on galaxy evolution, we first need to understand the physical conditions in the full diversity of OHM hosts. This is especially important because current and future surveys will detect the most luminous OHMs at unprecedented redshifts (Roberts et al. 2021). This is demonstrated by the record-breaking OHM host recently detected by LADUMA at a redshift of $z = 0.52$ (Glowacki et al. 2022), of which efforts are currently underway to measure its dense gas contents.

Addressing the lack of data for high-redshift and most luminous OHMs is a significant challenge. For the OHMs at these higher redshifts ($z = 0.1 - 0.25$), HCN (1-0) is redshifted to a frequency range (~75-80 GHz) that is only accessibly by a very limited number of telescopes, such as the IRAM 30m and GBT. Further, these measurements are expensive – requiring long integration times in narrow atmospheric transmission windows. We have been awarded time on the GBT and IRAM 30m to fill in this parameter space, but it is only for a handful of sources and will not be sufficient to separate OHMs and non-masing (U)LIRGs. As we wait for these observations to conclude, other tests for the dense gas fraction hypothesis should be considered.

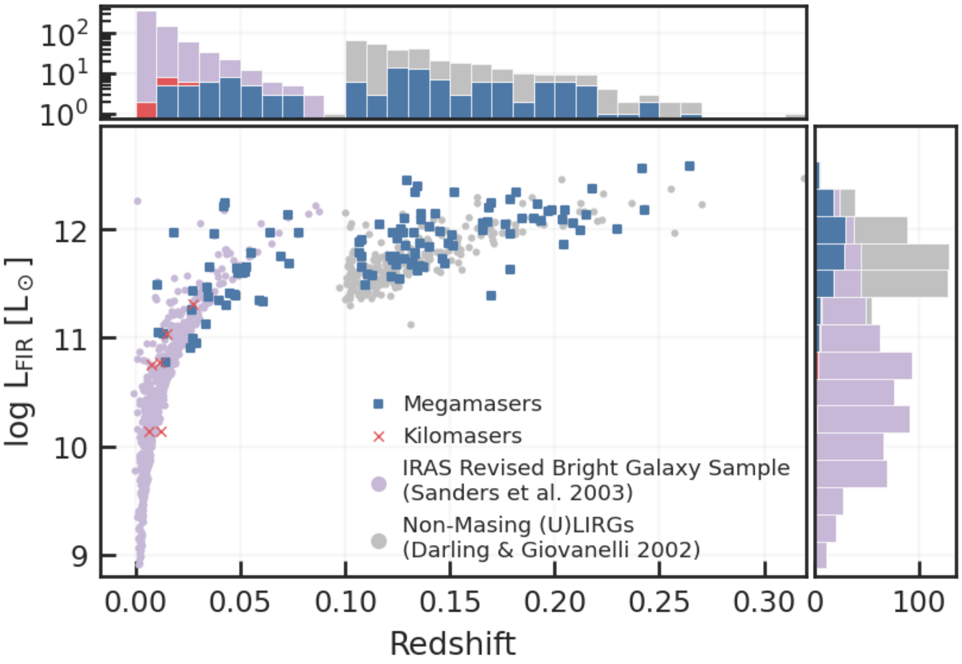

Figure 5.6 Far-IR luminosity versus redshift for OHMs (blue squares), kilomasers (red x's), the non-masing (U)LIRG sample from Darling & Giovanelli (2002a) (grey circles), and the IRAS Revised Bright Galaxy Sample (Sanders et al. 2003; IRAS RBGS, purple circles). The RBGS galaxies are shown for comparison, but not necessarily all sources have been confirmed to not host OHMs. This figure omits the recent OHM detection by LADUMA at $z = 0.52$.

5.2.3 Spatial Dense Gas Fraction

To understand the underlying physics that drives the production of OHMs, we have to find a way to directly connect the dense gas fraction to OH maser emission. One possible way of accomplishing this is using ALMA, which has both the required spatial resolution and spectral range to do this. In conjunction with existing OH maser maps, this would allow us to investigate if OH masing regions and high dense gas fraction regions are spatially coincident. The physical mechanism behind OHMs has long been theorized about, but now, we present the first direct test of our understanding.

Archival ALMA data allows us to illustrate this concept for one of the most well-known OHMs, Arp 220. To create a dense gas fraction map, we use HCN (1-0) emission data from ALMA Program 2015.1.00702.S and ^{12}CO (1-0) emission data from ALMA Program 2015.1.00113.S. As

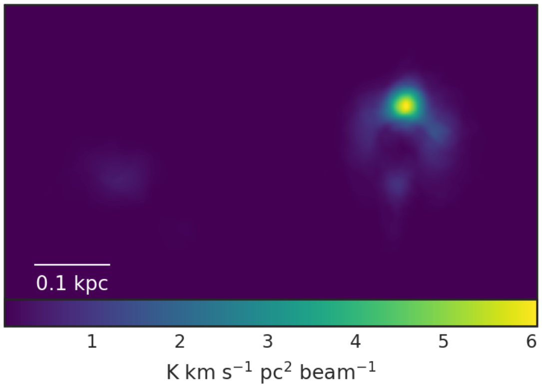

Figure 5.7 HCN (1-0) line luminosity map for Arp 220 using data from ALMA Program 2015.1.00702.S.

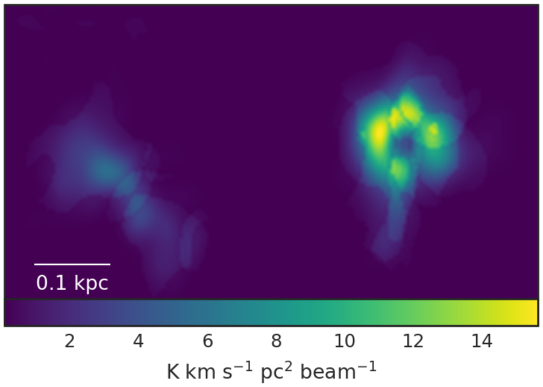

Figure 5.8 ^{12}CO (1-0) line luminosity map for Arp 220 using data from ALMA Program 2015.1.00113.S.

these are two separate programs and observing frequencies, the beam size is different between the two data cubes so we first convolve the cubes to the smallest common beam size and then regrid to match so that the beams and pixels are identical. Next, we take the zeroth moment of each cube in order to get maps of the integrated flux. We convert these integrated flux maps using equation (3) from Solomon et al. (1997). The L_{HCN} and L_{CO} maps are shown in Figure 5.7 and Figure 5.8, respectively. These maps are spatial representations of the integrated flux measurements used for dense gas fraction calculations.

Now that we have line luminosity maps, we simply take the ratio of the two images to reveal the dense gas fraction map, shown in Figure 5.9. The overlaid white contour lines correspond to OH maser emission from Rovilos et al. (2003). Here we see that the high dense gas fraction and OH masing regions are somewhat coincident but perhaps no more coincident than the two nuclei in the major merger, both of which host masing regions – which is not the case for all OHMs. While informative, a sample size of one is not representative of a population. To begin forming a better understanding of the physical mechanisms behind nearby OHMs, it is imperative to perform this test on more OHMs and on those with varying properties.

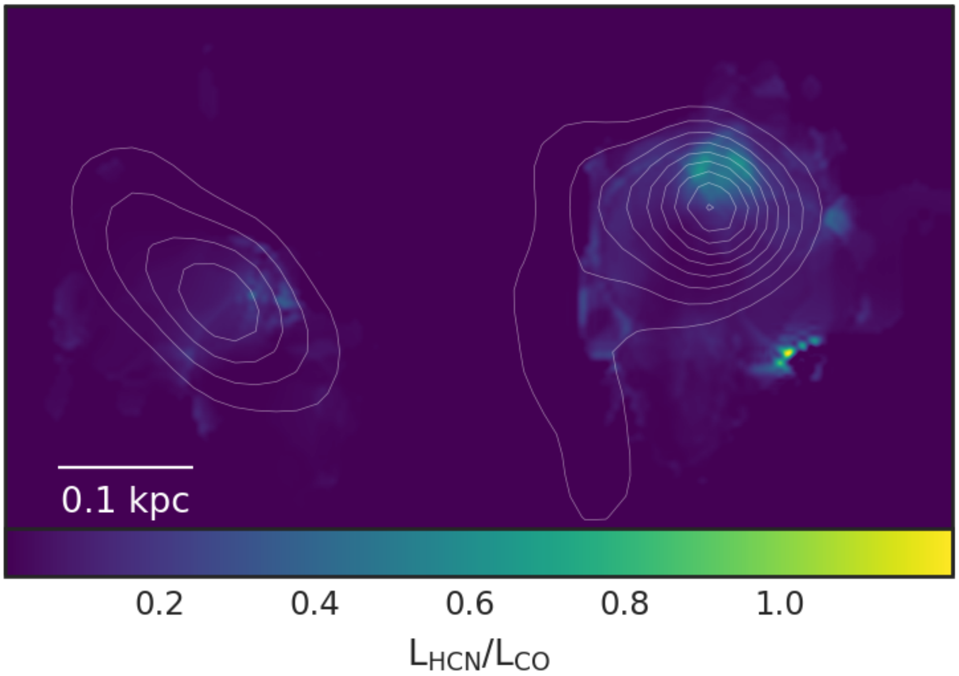

Figure 5.9 $L_{\rm HCN}/L_{\rm CO}$ map of Arp 220 using line luminosity maps shown in Figures 5.7 and 5.8. The contour lines show OH maser emission from Rovilos et al. (2003). The beam size for the contours is 84.7×67.3 $\rm pc^2$.

5.2.4 Complications & Future Considerations

While more work is still needed for the spatially resolved case, the reassessment of the dense gas fraction on an unresolved scale suggests that this hypothesis can be refuted. However, recent studies have shown that the HCN (1-0) content in galaxies *may* be inflated due to AGN activity, but not consistently (Privon et al. 2015; Gallagher et al. 2018) – casting doubt on the reliability of HCN (1-0) as a dense gas tracer in galaxies with high star formation rates. These issues can likely be alleviated by using other dense gas tracers (Shirley 2015) or higher J-transition (Imanishi et al. 2023). These considerations require careful treatment in OHMs, which are homes to numerous intertwined processes (i.e. star formation, obscured nuclei, mergers, etc.) and frequently found at higher redshifts than previously studied (U)LIRGs (see Figure 5.3).

5.3 Conclusions

Unlocking the secret behind OHM formation has numerous challenges, including limited sample size, diversity within the population, expensive observations, and others previously discussed. The work presented in this chapter has outlined some promising paths for beginning to make sense of these complicated processes. Furthermore, while this is necessary to understand the context of high-redshift OHM discoveries, upcoming surveys will also detect a substantial number of nearby OHMs, particularly in the southern sky from ASKAP surveys (Roberts et al. 2021). This is especially exciting, as ALMA is currently undergoing upgrades to increase instantaneous bandwidth and sensitivity in all bands, allowing faster mapping of dense gas tracers in OHM hosts. These next-generation telescopes, in addition to careful treatment of dense gas measurements, will greatly assist in validating the dense gas fraction hypothesis or identifying other mechanisms required for OHM formation.

Acknowledgements

This work has been supported by the National Science Foundation through grant AST-1814648, as well as the National Radio Astronomy Observatory. This research has made use of the NASA/IPAC Extragalactic Database (NED), which is funded by the National Aeronautics and Space Administration and operated by the California Institute of Technology.

Chapter 6

An Updated Census of OH Megamasers and Their Host Galaxies

Abstract

We present an updated and standardized catalog of all 120 known OH megamasers (OHMs) detected to date. This catalog includes information about the OHMs as well as properties of their host galaxies. Using these data, we present updated relationships between the masers and their host galaxies, demonstrating that some historical distinctions may be arbitrary.

This chapter is in preparation and will be submitted for publication in ApJ in 2023.

6.1 Introduction

Just over four decades ago, the first OH megamaser (OHM) was discovered in Arp 220, a nearby ultra-luminous infrared galaxy (Baan et al. 1982). Since then, more OHMs have been found in (ultra-)luminous infrared galaxies ([U]LIRGs) produced by major galaxy mergers, often associated with extreme star formation rates (Darling & Giovanelli 2002a). The 1667 MHz masing lines produced in the nuclear regions of these galaxies have isotropic OH luminosities of $L_{\rm OH} \geq 10^1 L_\odot$ with line widths of 50–1000+ $\rm km\,s^{-1}$. Sources with luminosities of $L_{\rm OH} < 10^1 L_\odot$ are typically referred to as OH *kilo*masers and are thought to be a distinct class from OHMs.

In the years since their initial discovery, there have been numerous searches for new OHM hosts (e.g., Staveley-Smith et al. 1987; Dickey et al. 1990; Baan et al. 1992b; Darling & Giovanelli 2002a; Willett 2012). These searches have predominately been carried out in IR-luminous galaxies and have tended to yield very low detection rates, a symptom of our incomplete knowledge of what is required for a galaxy to produce an OHM. At the time of publication, 120 OHM hosts have been identified after searches in an order-of-magnitude more galaxies.

These low detection rates will soon be alleviated by new OHM discoveries with upcoming 21 cm neutral hydrogen (H I) surveys that will serendipitously detect the 18 cm OH line. In the most conservative estimates, this will result in an increase in the number of known OHM hosts by an order of magnitude (Roberts et al. 2021). The ability for H I surveys to detect OHMs has already been highlighted by recent detections from Apertif (Hess et al. 2021) and LADUMA (Looking at the Distant Universe with the MeerKAT Array; Glowacki et al. 2022). The latter of these detections shattered the long-standing record for highest redshift OHM host with the discovery of an OHM host at a redshift of $z = 0.52$. The next highest redshift OHM host is at a redshift of $z = 0.265$ and was discovered thirty years prior (Baan et al. 1992b).

In this exciting time before the number of OHM hosts increases drastically, we present a comprehensive catalog of the known 120 OHMs and their host galaxies, as well as 6 OH kilomasers. Other studies have presented partial catalogs, however these have tended to be incomplete, not properly accounted for differing cosmologies among detection papers, or included problematic sources. Here we strive to present a base catalog that properly accounts for these issues. We also include commonly cited properties of the OHM host galaxies, such as optical classification, IR photometry, and radio continuum. Lastly, we reconsider some often studied relationships between OHMs and their host galaxies. Throughout this work, we assume a flat ΛCDM cosmology with $H_0 = 70$ km s^{-1} Mpc^{-1}, $\Omega_m = 0.3$, and $\Omega_\Lambda = 0.7$.

6.2 An Updated OHM Catalog

We present an updated catalog of all 120 known OHMs detected to date. This catalog, presented in Appendix B – see Table 6.1 for column descriptions, is based on an extensive search of the literature and includes the most recent OHM discoveries, as well as the new sources presented in this paper. All sources and their associated components in other catalogs presented here were crossmatched using `astroquery`[1] (Ginsburg & Goddi 2019) and then each component was visually inspected to ensure proper identification.

All luminosities presented in this paper were converted from the original cosmology used in each study to the cosmology used in this paper to ensure consistency. This catalog also includes six known OH kilomasers, but these sources are omitted when calculating OHM population properties. Furthermore, sources that do not have existing OH spectra in the literature are noted in Table B.1. Although these sources cannot be verified, they are assumed to be valid based on consistent measurements in the literature. However, a few sources that were previously published as OHMs have been omitted from this catalog. Below, we discuss these notable exceptions:

- **IRAS 05189-2524.** Upper limits of OH emission in this source are reported in Staveley-Smith et al. (1987) and Norris et al. (1989). These upper limits only constrain the OH luminosity to $L_{OH} < 10^{2.71}$ $L_\odot$ and do not exclude this source from being an OHM. However, these upper limits have been reported as measurements in subsequent studies, leading to this source being incorrectly reported as an OHM, such as in Yu (2003), Chen et al. (2007), and Zhang et al. (2014). Therefore, we omit it from our catalog.

- **IRAS 09320+6134.** As first discussed in Darling & Giovanelli (2002a), this source was first reported as an OHM in Martin et al. (1989), but observations from Baan et al. (1992b) measured an upper limit on the OH luminosity that is much lower than the reported values. These values limit the OH luminosity to $L_{OH} < 10^{-0.37}$ $L_\odot$, excluding this source from being an OHM.

- **IRAS 13097-1531.** Also first noted in Darling & Giovanelli (2002a), this source is presented as an OHM in Martin et al. (1989) and Henkel & Wilson (1990) where the reported OH detection occurs at 1630 MHz, corresponding to a redshift of $z = 0.023$. However, the redshift of this galaxy has been measured to be $z = 0.0099$ (Wegner et al. 2003); therefore, we omit this source from our catalog.

---

[1] https://github.com/astropy/astroquery

- **IRAS 16145+4231.** Again, noted in Darling & Giovanelli (2002a), Bottinelli et al. (1990) reports a detection of an OHM at a luminosity distance of 375 Mpc. However, the optical spectroscopic redshift of this source ($z = 0.227$) places it at a luminosity distance of 99 Mpc. This significant discrepancy indicates that this detection is unlikely to be real.

The purpose of this catalog is to standardize the values and equations used to investigate OHMs as a population. For this reason, while OH line widths are provided in Table B.1, any analysis that includes the line widths has been omitted from this work due to the complete lack of consistency between studies of how it is measured and reported. In some cases, no line width is reported at all, but instead the width has been visually estimated from the published spectrum; these cases are noted in the table notes. This is further complicated by the highly irregular line profiles observed in OHMs due to Doppler broadening from microturbulence. Omitting line widths from this analysis is non-ideal for numerous reasons. OHMs can produce masing lines that span a wide range of widths ($\sim 50 - 1000+$ km s^{-1}) and these line widths may be indicative of important underlying properties in the OHM host galaxy. Darling & Giovanelli (2002a) showed that the most luminous OHMs tend to produce the broadest lines and Darling & Giovanelli (2006) identified a tentative relation between the presence of LINER and Seyfert nuclei and broad OH lines. However, irregularities between reported line widths would result in a flawed analysis, preventing further inspections than those presented in Darling & Giovanelli (2002a) and Darling & Giovanelli (2006).

Figure 6.1 shows the OH luminosity versus redshift for these sources, as well as the OH non-detections from the Arecibo Observatory OH Megamaser Survey (Darling & Giovanelli 2000, 2001, 2002a). These sources were included to illustrate the boundary between masing and non-masing (U)LIRGs. The most luminous OHM has an OH luminosity of $\mathrm{L_{OH}} = 10^{4.2}$ $\mathrm{L_{\odot}}$ and the recently discovered most distant OHM is at a redshift of $z = 0.5225$ (Glowacki et al. 2022), with the next most distant OHM only at a redshift of $z = 0.265$.

Notably, IRAS 23327+2913 was originally observed in Darling & Giovanelli (2001) and was determined to be an OH non-detection with a maximum OH luminosity of $\mathrm{L_{OH}} < 10^{1.77}$ $\mathrm{L_{\odot}}$ at a

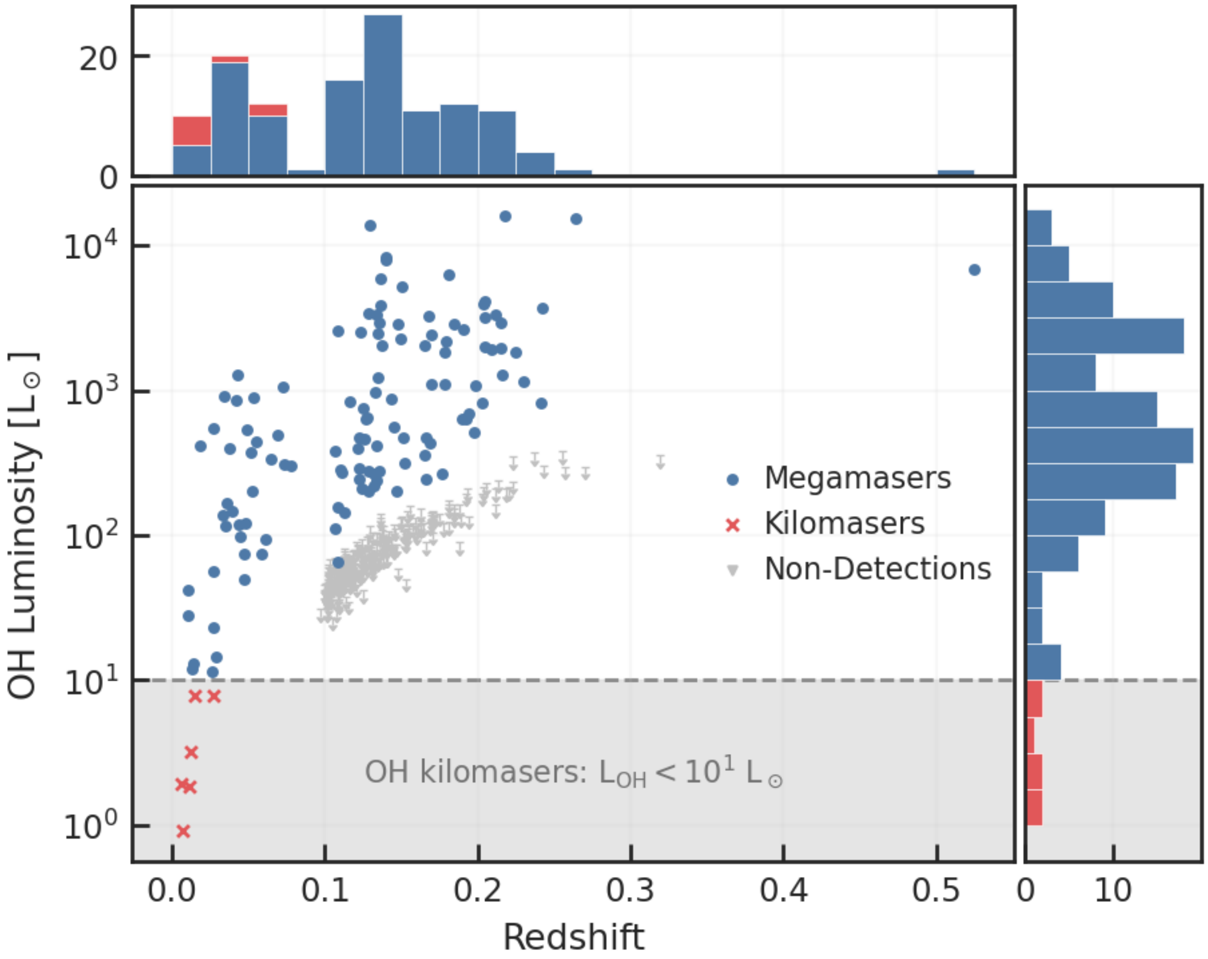

Figure 6.1 Distribution of OH luminosity vs. redshift for known OHMs (blue circles), OH kilomasers (red x's), and OH non-detections from the Arecibo Observatory OH Megamaser Survey (Darling & Giovanelli 2000, 2001, 2002a; gray arrows indicating upper limits in OH luminosity). The distribution in redshift is shown in the histogram above the scatter plot, and the distribution in OH luminosity is shown in the histogram on the right. The non-detections are omitted from these histograms.

redshift of $z = 0.1070$. This upper limit puts this source below the expected OH luminosity based on its far-IR luminosity. However, Fernandez et al. (2010) reobserved this source for OH emission with an integration time nearly three times longer than Darling & Giovanelli (2001), lowering the RMS noise level from 0.68 to 0.19 mJy, measuring OH emission at a luminosity of $L_{OH} = 10^{2.05}\ L_\odot$, confirming that this source is an OHM.

Table 6.1 Column descriptions of the OHM catalog presented in Appendix B

Table	Column	Description
All Tables	Common Name	Commonly used or abbreviated name for the OHM host galaxy; can be used to join all tables
Table B.1	RA, Dec	Optical position of the OHM host galaxy
	z	Redshift
	$\log L_{OH}$	Isotropic OH luminosity; see table footer for note descriptions
	ΔV	OH line width when available; see table footer for note description
	Ref.	References for initial OH detection or confirming validity of the detection; see table footer for each reference
	Type	Spectral type of each host galaxy; see table footer for abbreviation meanings
	Type Ref.	References for spectral types; see table footer for each reference
Table B.2	IRAS	Source designation in IRAS FSC or PSC (Beichman et al. 1988)
	$\log L_{IR}$	IR luminosity calculated using the formulation presented in Sanders & Mirabel (1996)
	$\log L_{FIR}$	Far-IR luminosity calculated using the formulation presented in Sanders & Mirabel (1996)
	$f_{12,25,60,100\mu m}$	Flux densities for each IRAS band
Table B.3	WISE Designation	Name in AllWISE catalog (Cutri et al. 2021)
	α_{WISE}	Spectral index across WISE bands
	$f_{W1,W2,W3,W4}$	Flux densities for each WISE band, K-corrected using the formulation presented in Wright et al. (2010)
Table B.4	NVSS	Source name from NVSS catalog (Condon & Kaplan 1998)
	f_{NVSS}	Flux density from NVSS; see table footer for note descriptions
	FIRST	Source name from FIRST catalog (Helfand et al. 2015)
	f_{FIRST}	Integrated flux density from FIRST survey

6.3 Spectral Classification

Table B.1 includes spectral classification information about OHM hosts when available. This expands on the work done by Darling & Giovanelli (2006) and, previously, Baan et al. (1998).

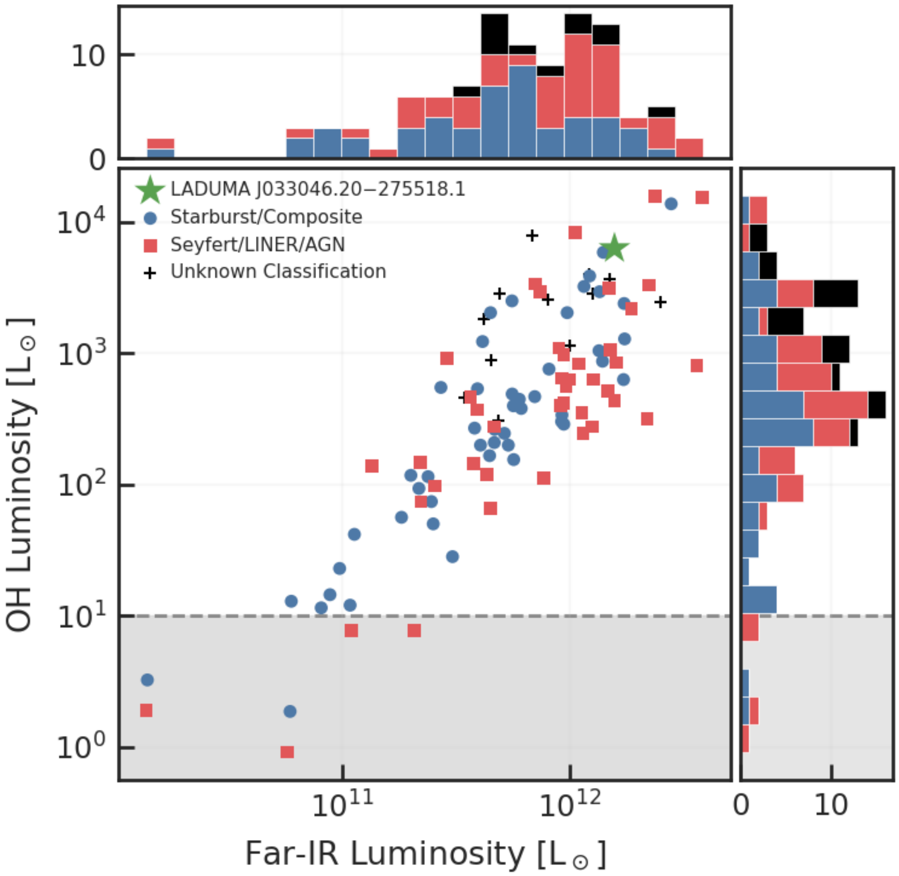

Figure 6.2 OH luminosity versus far-IR luminosity for known OHM and OH kilomasers with designated spectral classifications from the literature. The histogram of the far-IR luminosity distribution by type is shown on the top, and the histogram of the OH luminosity distribution is shown on the right. All data and references can be found in Table B.1. LADUMA J033046.20-275518.1, the highest redshift OHM presented in Glowacki et al. (2022), is denoted by a green star, but no classification of the host galaxy has been determined.

Darling & Giovanelli (2006) compared spectral classifications of 77 (U)LIRGs – 43 of which are OHM hosts – and determined that optical classification reveals little about the nuclear environment that describes OHM hosts. Using these data, as well as measurements from the literature, Table B.1 presents spectral classifications for 91 OHM hosts. Figure 6.2 presents the OH luminosity versus the far-IR luminosity for OHMs where spectral classification is designated by color and marker type. Since OHM hosts are heavily obscured, we classify them into two broad categories: AGN-dominated or starburst/composite (i.e. having signatures of both AGN and starburst activity). With this expanded sample of OHM hosts, there remains no distinction between nuclear type and

OH distribution.

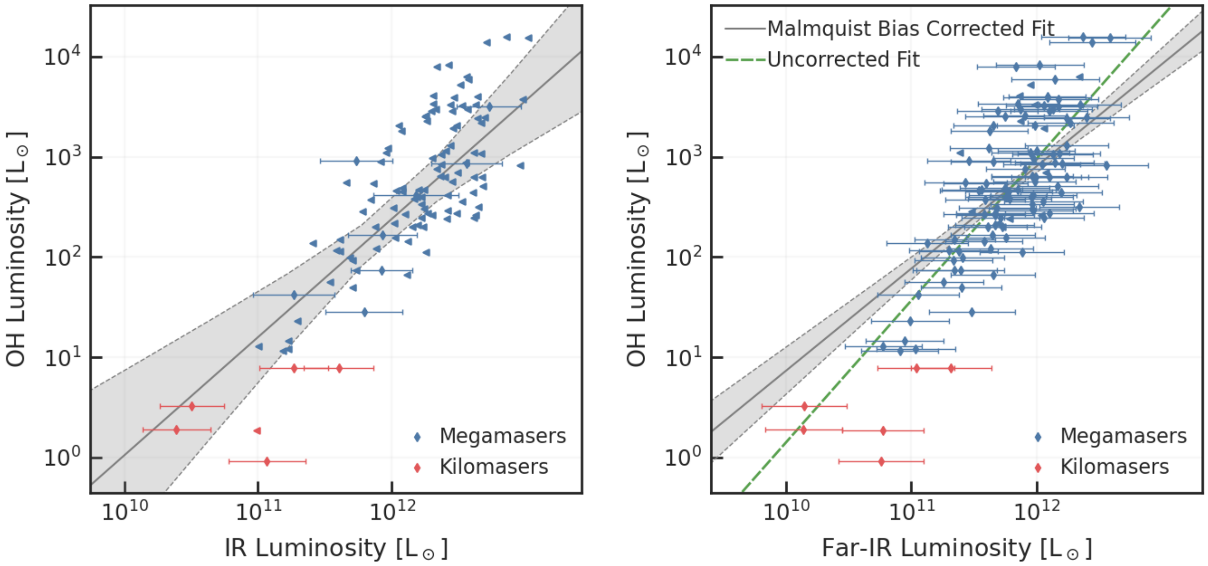

Figure 6.3 OH luminosity versus IR luminosity (left) and far-IR luminosity (right). Points without error bars represent upper limits in IR/far-IR luminosity. The IR luminosity plot shows a fit between IR luminosity and OH luminosity; however, this relation is unlikely to describe anything of relevance and is presented for demonstration purposes only. The far-IR luminosity plot shows two fits between far-IR and OH luminosity – the green dashed line is uncorrected for Malmquist bias while the gray shaded line is corrected.

6.4 Infrared and Radio Properties of OHM Hosts

Table B.2 presents the IRAS properties of OHM hosts. When all four IRAS bands are available for a given source, the IR luminosity is calculated while the far-IR luminosity is provided for sources where the 60 μm and 100 μm bands are available. Otherwise, upper limits are calculated. Following the form presented in Sanders & Mirabel (1996), the IR luminosity is calculated as

$$L_{\mathrm{IR}} = 4\pi D_L^2 (1+z)^{-1} \left(1.8 \times 10^{-14} \left(13.48 f_{12} + 5.16 f_{25} + 2.58 f_{60} + f_{100}\right)\right) \; [L_\odot] \,, \tag{6.1}$$

where D_L is the luminosity distance, z is the redshift of the source, and f is the flux density in Jy for each respective band. Similarly, the far-IR luminosity is calculated as

$$L_{\mathrm{FIR}} = 4\pi D_L^2 (1+z)^{-1} \left(1.26 \times 10^{-14} \left(2.58 f_{60} + f_{100}\right)\right) \; [L_\odot] \,. \tag{6.2}$$

OH luminosity is plotted against IR and far-IR luminosity in Figure 6.3 for OHM hosts and OH kilomasers. However, the $L_{\rm OH} - L_{\rm FIR}$ relation has been examined numerous times in previous work (e.g., Baan 1989; Kandalian 1996; Darling & Giovanelli 2002a) and strong correlations have been identified. This is unsurprising since OHMs are pumped through far-IR radiation (Lockett & Elitzur 2008), but the exact relation between far-IR and OH luminosity depends on the degree of saturation in a given OHM host. The theoretical relation between OH and far-IR luminosity is given by $\log L_{\rm OH} \propto \gamma \log L_{\rm FIR}$ where $1 \leq \gamma \leq 2$ with $\gamma = 1$ indicating high-gain saturated emission and $\gamma = 2$ indicating low-gain unsaturated emission (Baan 1985; Darling & Giovanelli 2002a). As OHMs are ensembles of masing regions with varying degrees of saturation, this value will differ from system-to-system and spatially within a given source (e.g. Diamond et al. 1999; Momjian et al. 2006).

We evaluate the empirical relation between OH and IR/far-IR luminosity using a weighted least-squares fit while omitting kilomasers and sources with only upper limits. With only eight OHMs that have all four IRAS bands, the $\rm L_{OH}$-$\rm L_{IR}$ relation is presented for demonstration purposes only and no conclusions should be drawn based on the data. However, using the available data, the measured fit between OH and IR luminosity is

$$\log L_{\rm OH} = (1.18 \pm 0.41) \log L_{\rm IR} - (11.76 \pm 4.93), \tag{6.3}$$

where $L_{\rm OH}$ and $L_{\rm IR}$ are in units of solar luminosities. This relation and its confidence intervals are shown in the left panel of Figure 6.3.

The relation between OH and far-IR luminosity can be much better constrained as it only requires the 60 and 100 μm bands, yielding an available sample size of 97 sources, omitting kilomasers and sources only with upper limits. However, this larger sample size requires consideration of Malmquist bias. The relation between OH and far-IR luminosity, uncorrected for Malmquist bias, is

$$\log L_{\rm OH,uncorrected} = (1.41 \pm 0.12) \log L_{\rm FIR} - (13.99 \pm 1.43). \tag{6.4}$$

This is shown as the green dashed line in the right panel of Figure 6.3. Accounting for Malmquist bias using the prescription presented in Kandalian (1996), this relation becomes

$$\log L_{\rm OH} = (1.02 \pm 0.13) \log L_{\rm FIR} - (9.32 \pm 1.51), \tag{6.5}$$

which is shown as the gray line with confidence intervals in the right panel of Figure 6.3. This is much shallower than the uncorrected fit and fits performed in previous studies. Darling & Giovanelli (2002a) obtained a fit of $\log L_{\rm OH} \propto 1.24 \log L_{\rm FIR}$ and Kandalian (1996) had previously reported a fit of $\log L_{\rm OH} \propto 1.38 \log L_{\rm FIR}$ – both of which also account for Malmquist bias. The best explanation for this discrepancy is the changing landscape of known OHM hosts. Previous studies evaluated these relationships in a much sparser and more homogeneous population. As more OHMs are discovered, the parameter space occupied by these sources is becoming better understood. As shown in Figure 6.4, early years of OHM discoveries were biased towards nearby IR-bright host galaxies. However, with next-generation radio surveys currently underway, the serendipitous detection of new OHMs will likely bias toward OH-luminous sources rather than IR-luminous hosts. More importantly, any observed correlation between luminosities requires additional scrutiny due to the universal dependence on distance. The correlation coefficient between far-IR and OH luminosity accounting for their mutual dependence on distance yields a value of $R = 0.40$, indicating this is only a weak correlation. A much more detailed discussed is presented in Section 6.6.

In addition to IR properties from IRAS, K-corrected AllWISE (Wright et al. 2010) flux densities are presented in Table B.3. For each source, the spectral index ($\alpha_{\rm WISE}$, also included in Table B.3) is calculated across the available bands and the flux densities are K-corrected using the prescription presented in Wright et al. (2010). The WISE W3 (12 μm) and W4 (22 μm) bands are ~5,000 times more sensitive than the IRAS 12 μm and 25 μm bands. Cluver et al. (2017) showed that for ULIRGs, the W3 band is underluminous compared to the total IR luminosity, while the W4 band is overluminous. This makes these bands particularly helpful for constraining the total IR luminosity in ULIRGs lacking the shorter wavelength IRAS bands.

Lastly, 21 cm/1.4 GHz flux densities are included from NVSS (Condon & Kaplan 1998) and FIRST (Helfand et al. 2015). A more diverse set of radio continuum measurements is presented in

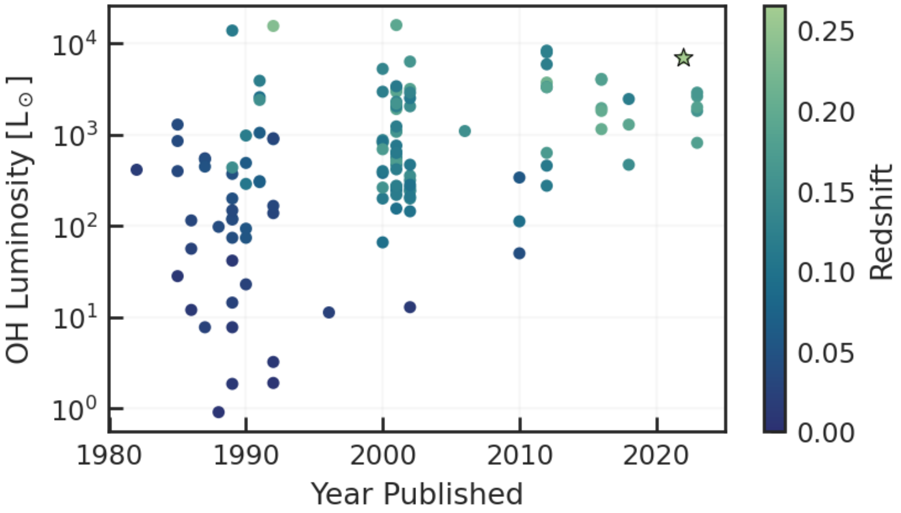

Figure 6.4 OH luminosity versus year the OHM detection was first published for the sources presented in the OHM catalog in Section B. The redshift of the source is designated by the color of each marker, except for the star that designates the notable redshift outlier at $z = 0.52$ (Glowacki et al. 2022).

Sotnikova et al. (2022). However, the four OHMs omitted from this catalog due to likelihood of being spurious detections are presented as OHM detections in the Sotnikova et al. (2022) catalog, so caution is advised when comparing properties of OHMs and non-masing host galaxies.

6.5 IR Excesses and Spectral Indices

To further investigate the underlying OHM host galaxy population, a helpful parameter examined in previous studies such as Darling & Giovanelli (2002a) and Sotnikova et al. (2022) is the q-parameter, or the logarithm ratio of far-IR to radio flux density in a source (Helou et al. 1985; Condon et al. 2002):

$$q = \log\left(\frac{2.58 f_{60} + f_{100}}{2.98 \times 10^{26}}\right) - \log\left(f_{21\mathrm{cm}}\right), \tag{6.6}$$

where f_{60} and f_{100} are the 60 μm and 100 μm flux densities from IRAS in Jy and $f_{21\mathrm{cm}}$ is the 21cm/1.4 GHz flux density from NVSS or FIRST, also in Jy. To calculate the q-parameter, we use flux densities from FIRST when available, since FIRST's sensitivity limit is a factor of ∼2 better and angular resolution is nearly 10 times better, allowing for much better characterization of bright compact radio sources. Flux densities from NVSS were used when measurements from FIRST were not available. A cutoff value of $q = 1.8$ is often implemented to distinguish between star-forming galaxies ($q \gtrsim 1.8$) and radio-loud AGN ($q \lesssim 1.8$) (Yun et al. 2001; Condon et al. 2002; Mauch & Sadler 2007). For the OHM catalog presented here, the mean value of the q-parameter is 2.51 (rms=0.35, N=91) with only three sources falling below the q<1.8 nominal cutoff for AGN distinction. Calculating the q-parameter for the OH non-detections discussed previously, a mean value of 2.37 (rms=0.26, N=136) is obtained with, again, three sources falling below the AGN cut-off point. The histogram of these q-parameter values are shown in the upper panel of Figure 6.6. Yun et al. (2001) identified a set of galaxies that have unusually high IR emission compared to their radio flux (q>3.0). These IR-excess galaxies are marked by dense, compact star-forming regions (Condon et al. 1991) – properties that are synonymous with OHM hosts (e.g. Darling 2007; Willett et al. 2011b; Hekatelyne et al. 2018). Five (5.5%) OHMs from our catalog have a measured q-parameter in this IR-excess region, where as only two (1.5%) of the non-detections are in this region. Surprisingly, two of the six kilomasers in the catalog are also in this region.

It should be noted that this comparison between OHMs and these non-detections is flawed. The non-detections were part of a flux-limited survey at redshifts $z \geq 0.1$, while this OHM catalog is a collection of all known and verifiable OHMs. There is no standardization of flux limits or redshift range. However, these comparisons can still offer helpful insights into the underlying population of OHM host galaxies. Furthermore, our results are consistent with those presented in Darling & Giovanelli (2002a) using a proper flux-limited sample for both populations. Performing an Anderson-Darling 2-sample test on the q-parameter values of OHM host and non-detection galaxies yields a result that strongly rejects the null hypothesis that masing and non-masing hosts are drawn from the same distribution (p<0.001) – remaining consistent with results from Darling & Giovanelli (2002a) and Sotnikova et al. (2022).

In addition to the q-parameter, another helpful metric for assessing the properties of OHM host galaxies is the far-IR spectral index between 25 μm and 60 μm, which is typically designated

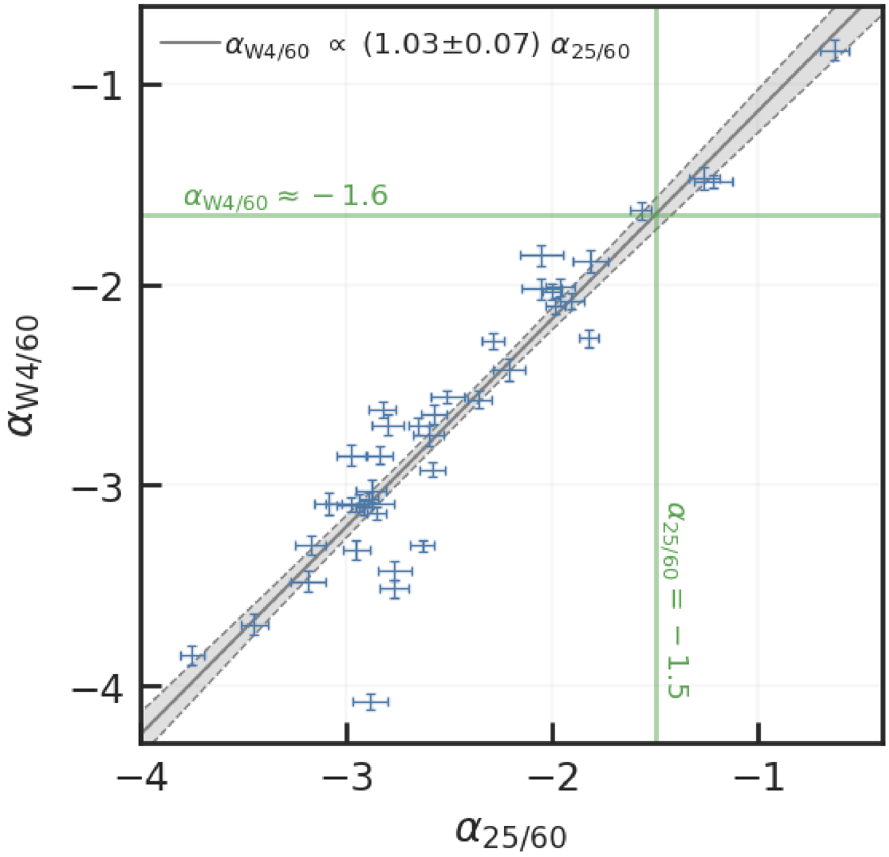

Figure 6.5 Comparison of $\alpha_{W4/60}$ vs. $\alpha_{25/60}$ for OHM hosts. A simple fit finds these to be linearly related, shown as the gray line with shaded confidence intervals. Using this relation, an approximate conversion of the dust temperature barrier value of $\alpha_{25/60} = -1.5$ can be calculated as $\alpha_{W4/60} \approx -1.6$.

as α_{FIR}, but we will refer to this specific form as $\alpha_{25/60}$:

$$\alpha_{25/60} \coloneqq \alpha_{\rm FIR} = \frac{\log\left(f_{25}/f_{60}\right)}{\log(60/25)}, \tag{6.7}$$

where f_{25} and f_{60} are in units of Jy. The far-IR spectral index is a useful measure for dust temperature, where $\alpha_{25/60} < -1.5$ is associated with star-forming galaxies with dust temperatures of T $<$ 50K and $\alpha_{25/60} > -1.5$ is associated with AGN or galaxies that have recently undergone a merger, resulting in higher dust temperatures of T $>$ 100K (Armus et al. 1990; de Grijp et al. 1992; Kewley et al. 2001). Of the 110 OHM hosts that have 60 μm measurements presented in Table B.2, only 41 hosts also have 25 μm flux density measurements, excluding sources with only upper

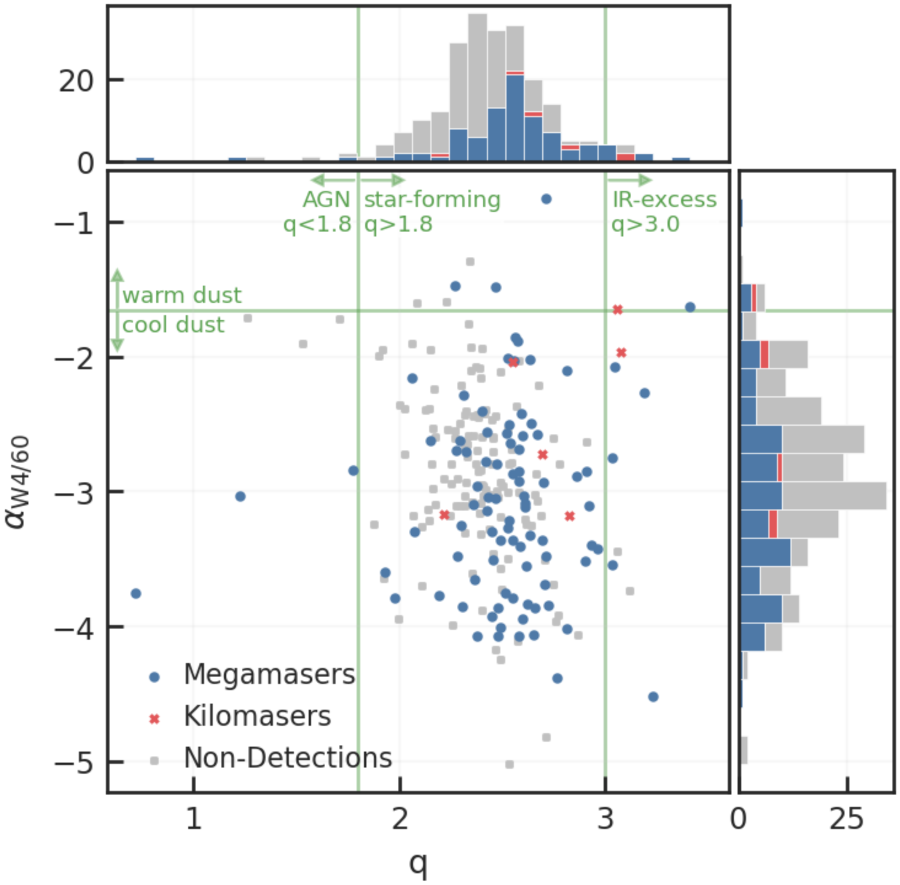

Figure 6.6 Scatter plot of $\alpha_{\mathrm{W4/60}}$ vs. q-parameter for OHM hosts (blue circles), kilomaser hosts (red x's), and non-detections (gray squares). The boundaries describing host galaxy properties, as discussed in Section 6.5, are shown as green lines with arrows indicating their relevant regions. Histograms of the q-parameter and spectral indices are shown above and to the right of the scatter plot.

limits. However, as shown in Table B.3, 103 OHM hosts have W4 (22 μm) measurements available. Accordingly, a far-IR spectral index that makes use of the WISE W4 band is significantly more powerful, which we calculate as

$$\alpha_{\mathrm{W4/60}} = \frac{\log\left(f_{22}/f_{60}\right)}{\log(60/22)}. \tag{6.8}$$

To compare these forms of spectral indices, we plot this new form vs. the original form in Figure 6.5 for the 49 OHM hosts that have available 25 μm measurements from IRAS. A fit to these measurements reveals a tight linear correlation and is plotted as the line with shaded confidence intervals. The approximate translation of $\alpha_{25/60} = -1.5$ into this basis gives $\alpha_{\mathrm{W4/60}} \approx -1.6$. Figure

6.6 plots this adapted spectral index value vs. the q parameter, including the boundaries discussed previously that describe the host galaxies. Only four OHMs and three non-detections have far-IR spectral index values greater than $\alpha_{\mathrm{W4/60}} > -1.6$.

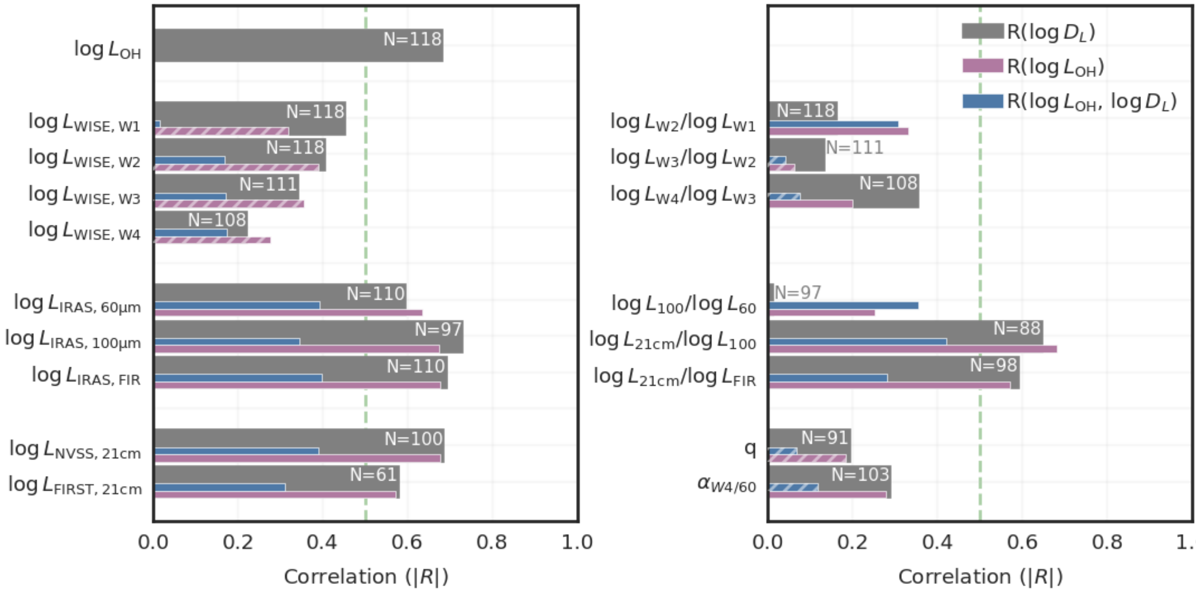

Figure 6.7 Absolute correlation comparisons for many of the metrics discussed in this work. The left panel shows correlation tests between luminosities, while the right panel shows correlation tests between more complex parameters. For each parameter, its correlation with distance is shown by the gray bar, its correlation with OH luminosity, uncorrected for mutual correlation with distance, is shown by the purple bar, and the partial correlation, accounting for mutual correlation, is shown by the blue bar. The bars with hatches indicate cases where the resulting p-value is greater than 0.05. The green dashed line indicates where $|R| = 0.5$, above which values are considered moderately correlated.

6.6 OH Luminosity Correlations – or Lack Thereof

The empirical relationships describing OHMs and their host galaxies are discussed in previous sections. However, testing the physical validity of these correlations requires consideration of the mutual dependence on distance. For each set of parameters, we calculate their partial correlation, which measures the degree of association while controlling for the effects of a third variable, in this case, distance. The partial correlation is calculated as

$$R_{\mathrm{XY,Z}} = \frac{R_{\mathrm{XY}} - R_{\mathrm{XZ}} R_{\mathrm{YZ}}}{\sqrt{\left(1 - R_{\mathrm{XZ}}^2\right)\left(1 - R_{\mathrm{YZ}}^2\right)}}, \tag{6.9}$$

where R_{AB} can be either the standard Pearson or Spearman correlation coefficient. We opt to use the Spearman correlation coefficient for this work because of its sensitivity to monotonic relationships rather than strictly linear trends. However, this choice is inconsequential to the final results – partial Pearson correlation coefficients were calculated as well, and no significant deviations were found between the two methods.

Figure 6.7 and Table 6.2 illustrate the importance of considering the underlying correlations for all parameters. While we showed in Section 6.4 that a linear fit to OH luminosity versus far-IR luminosity yields a slope of $\gamma = 1.02 \pm 0.13$ when accounting for Malmquist bias, this still ignores the strong correlation that OH and far-IR luminosity have with distance. As shown in Table 6.2, the correlation coefficient with luminosity distance, $R(\log D_L)$ indicated by the gray bar in Figure 6.7, is 0.68 for OH luminosity and 0.69 for far-IR luminosity. A naive calculation of the correlation with OH luminosity $R(\log L_{\mathrm{OH}})$, ignoring this mutual dependence, would yield a value of 0.68. However, the partial correlation coefficient, $R(\log L_{\mathrm{OH}}, D_L)$, yields a value of 0.40, indicating that OH luminosity and far-IR luminosity are only weakly correlated. In addition, this value is lower than the correlation between far-IR luminosity and distance, indicating that OH luminosity is no more correlated with far-IR luminosity than the redshift of the host galaxy. This is consistent with the underpinning theoretical relation discussed in Section 6.4: The relationship between OH and far-IR (logarithmic) luminosity is not a linear relation, but rather a measure of the degree of masing saturation. The fit value of $\gamma = 1.02 \pm 0.13$ suggests that the current known population of OHMs tends towards being completely saturated. Whether this is a global property of OHMs or an indication of detection bias towards these sources is inextricable with this current population of known OHMs.

Extending this analysis for the other measurable parameters, none discussed in this work survive our significance test of achieving partial correlation with OH luminosity above a moderately

Table 6.2. Full and partial correlations for the parameters discussed in this work

Parameter	N	R($\log D_L$)	R($\log L_{\rm OH}$)	R($\log L_{\rm OH}$, $\log D_L$)
$\log L_{\rm OH}$	118	0.68 ($p<0.001$)	…	…
$\log L_{\rm WISE,W1}$	118	0.45 ($p<0.001$)	0.32 ($p<0.001$)	0.02 ($p=0.863$)
$\log L_{\rm WISE,W2}$	118	0.41 ($p<0.001$)	0.39 ($p<0.001$)	0.17 ($p=0.069$)
$\log L_{\rm WISE,W3}$	111	0.34 ($p<0.001$)	0.35 ($p<0.001$)	0.17 ($p=0.073$)
$\log L_{\rm WISE,W4}$	108	0.22 ($p=0.021$)	0.28 ($p=0.004$)	0.17 ($p=0.073$)
$\log L_{{\rm IRAS},25\mu{\rm m}}$	41	0.77 ($p<0.001$)	0.69 ($p<0.001$)	0.44 ($p=0.004$)
$\log L_{{\rm IRAS},60\mu{\rm m}}$	110	0.59 ($p<0.001$)	0.63 ($p<0.001$)	0.39 ($p<0.001$)
$\log L_{{\rm IRAS},100\mu{\rm m}}$	97	0.73 ($p<0.001$)	0.67 ($p<0.001$)	0.35 ($p<0.001$)
$\log L_{\rm IRAS,FIR}$	110	0.69 ($p<0.001$)	0.68 ($p<0.001$)	0.40 ($p<0.001$)
$\log L_{\rm NVSS,21cm}$	100	0.68 ($p<0.001$)	0.68 ($p<0.001$)	0.39 ($p<0.001$)
$\log L_{\rm FIRST,21cm}$	61	0.58 ($p<0.001$)	0.57 ($p<0.001$)	0.31 ($p=0.016$)
$\log L_{\rm W2}/\log L_{\rm W1}$	118	0.16 ($p=0.082$)	0.33 ($p<0.001$)	0.31 ($p<0.001$)
$\log L_{\rm W3}/\log L_{\rm W2}$	111	-0.13 ($p=0.168$)	-0.06 ($p=0.515$)	0.04 ($p=0.665$)
$\log L_{\rm W4}/\log L_{\rm W3}$	108	-0.36 ($p<0.001$)	-0.20 ($p=0.039$)	0.07 ($p=0.450$)
$\log L_{100}/\log L_{60}$	97	0.01 ($p=0.914$)	-0.25 ($p=0.013$)	-0.35 ($p<0.001$)
$\log L_{\rm 21cm}/\log L_{100}$	88	0.65 ($p<0.001$)	0.68 ($p<0.001$)	0.42 ($p<0.001$)
$\log L_{\rm 21cm}/\log L_{\rm FIR}$	98	0.59 ($p<0.001$)	0.57 ($p<0.001$)	0.28 ($p=0.005$)
q	91	-0.19 ($p=0.067$)	-0.18 ($p=0.082$)	-0.07 ($p=0.526$)
$\alpha_{W4/60}$	103	-0.29 ($p=0.003$)	-0.28 ($p=0.004$)	-0.12 ($p=0.240$)

correlated level of $|R| \geq 0.5$ and higher than the underlying correlation with distance. A few notable cases do appear for the complex parameter correlations shown in the right panel of Figure 6.7. Consistent with the results in Darling & Giovanelli (2002a), even though OHMs are found to favor hosts with IR-excess ($q \geq 3.0$), there is no correlation between OH luminosity and the q-parameter, likely the result of these parameters probing physical conditions at vastly different scales. In addition, no correlation is found between the far IR spectral index between 25(22)-60 μm ($\alpha_{\mathrm{W4/60}}$) with OH luminosity. However, the only two parameters that retained partial correlations, albeit weak, above the distance-correlation level are $\log L_{\mathrm{W2}}/\log L_{\mathrm{W1}}$ and $\log L_{100}/\log L_{60}$. These measurements are similar to $\alpha_{\mathrm{W4/60}}$, except at shorter and longer wavelengths, respectively. This suggests that while $\alpha_{22/60}/\alpha_{\mathrm{W4/60}}$ may be useful for identifying composite host galaxies in larger surveys, spectral indices at shorter/longer wavelengths may be sensitive to the smaller physical scales that influence the OH luminosity.

6.7 Conclusion

In this work, we presented an updated and standardized catalog of OHMs and their host galaxies. This catalog will serve as an important baseline before an era of new OHM detections brought on by next-generation H I surveys. Using the data presented in these catalog, we reconsider previously examined relationships between OHMs and their host galaxies. This work has shown that there lacks a clear distinction at the historical boundary between OH kilomasers and megamasers. Further, properly accounting for Malmquist bias, the relationship between far-IR and OH luminosity is only weakly correlated and related as $\log L_{\mathrm{OH}} \propto (1.02 \pm 0.13) \log L_{\mathrm{FIR}}$, in contrast to other studies that have found slopes greater than one. Further, examination of correlation between OH luminosity and other properties of OHM hosts shows no significant relationships between the parameters examined in this work for the current known population. The results of this work emphasize the need for an increase in the OHM population and detailed studies of these sources in order to truly understand the unifying properties in this population.

Acknowledgements

This work has been supported by the National Science Foundation through grant AST-1814648, as well as the National Radio Astronomy Observatory. This research has made use of the NASA/IPAC Extragalactic Database (NED), which is funded by the National Aeronautics and Space Administration and operated by the California Institute of Technology.

Chapter 7

Conclusions

In this thesis, I have laid the foundations for the future of new OHM detections in H I surveys and the subsequent novel science that will be made possible through these sources. Chapter 1 presented a brief history and overview of OHMs and their host galaxies spanning the 40 years since their discovery. Forecasts for the number of OHMs that will be discovered in next-generation H I surveys is presented in Chapter 2. Further, I present machine learning methods for flagging potential OHM hosts interloping in untargeted H I data that utilize near- to mid-IR photometry available for a large number of sources. These methods are tested using both H I data from archival and preliminary surveys in Chapter 3. This led to refinements of the initial algorithms from Chapter 2 and the identification of five new OHMs that were previously interloping in existing H I survey data. As an exciting preview of the future of OHM science forecasted throughout this thesis, Chapter 4 presents two new detections from next-generation H I surveys. Section 4.1 presents the detection by Apertif of one of the most luminous OHMs ever discovered, yielding high-quality measurements of both the 1667 and 1665 MHz lines. Further, upper limits are placed on the 1612 MHz satellite line and predictions for the number of satellite line detections in Apertif is presented. In Section 4.2, the record-shattering detection of an OHM at a redshift of $z = 0.52$ after just one night of observing with LADUMA is presented. Using the WISE photometry of the host galaxy, this detection is shown to be properly flagged in the methods presented in Chapter 2 as a potential OHM host.

Understanding the underlying conditions necessary in the production of OHMs is particularly important in the upcoming era of discovery. As such, Chapter 5 reconsiders the dense gas fraction hypothesis, demonstrating that this fails to separate OHMs from non-masing (U)LIRGs when considering a broad population of OHMs. Further, tests for spatial coincidence of dense gas fraction and masing regions are presented. This work, however, is still underway and the final results depend on pending data from GBT and the IRAM 30m. Finally, in Chapter 6, a catalog of all known OHM and their host galaxies is compiled and standardized, including their IR and radio properties. This chapter also presents a careful treatment of previously studied relations between OHMs and their host galaxies. This work is presented as a baseline for this exciting future of OHM detections.

At this moment, the field of OHM discovery is on the cusp of a brand new era full of revolutionary detections, both in number and quality. After decades of searches yielding small numbers of OHMs, next-generation radio telescopes will be revealing *thousands* of new sources in the next few years and fundamentally changing the landscape of what we know about OHMs and their host galaxies. Leveraging these freshly discovered major galaxy mergers will allow exploration and mapping of some of the most important mechanisms for driving galaxy evolution.

However, understanding the relationship between OHM hosts and non-masing (U)LIRGs is necessary to achieve this. Fortunately, we will soon be equipped with a large number of local OHMs, primarily found by Apertif and WALLABY, that will offer us a chance to re-evaluate what physical conditions are associated with a diverse OHM sample. While it is unlikely there is any *one* property that can be used to isolate OHM hosts from non-masing (U)LIRGs, being certain of any set of criteria is nearly impossible with small sample sizes and sparsely populated parameter spaces. With an order of magnitude new detections, however, a much more robust analysis of OHMs and their host galaxy properties can be done.

Further, understanding the origins and evolution of galaxies is one of the key scientific challenges presented in the most recent decadal survey (Astro2020). While there are many approaches to a topic this broad, OHMs offer a unique viewpoint. Every OHM detection is a discovery of a galaxy undergoing a major gas-rich merger resulting in extreme star formation, making these objects rich sources for probing what role star formation, strong far-IR radiation, and gas density play in galaxy evolution. While most galaxy merger identification methods require spatially resolved images, which become increasingly more difficult to obtain at high redshifts, detecting the luminous OH masing line indicates a merger, making them powerful tools in identifying high-redshift major galaxy mergers.

This exciting future of OHM discovery is just around the corner. Using the groundwork laid out in this thesis, we will be able to anticipate, identify, and characterize these upcoming detections, leading to a new era of OHM science.

Bibliography

Aalto, S., Polatidis, A. G., Hüttemeister, S., & Curran, S. J. 2002, A&A, 381, 783, doi: 10.1051/0004-6361:20011514

Abdalla, F. B., Bull, P., Camera, S., et al. 2015, in Advancing Astrophysics with the Square Kilometre Array (AASKA14), 17, doi: 10.22323/1.215.0017

Almeida, A., Anderson, S. F., Argudo-Fernández, M., et al. 2023, arXiv, arXiv:2301.07688, doi: 10.48550/arXiv.2301.07688

Altman, N. S. 1992, American Statistician, 46, 175, doi: 10.1080/00031305.1992.10475879

Armus, L., Heckman, T. M., & Miley, G. K. 1990, ApJ, 364, 471, doi: 10.1086/169431

Baan, W. A. 1985, Natur, 315, 26, doi: 10.1038/315026a0

—. 1989, ApJ, 338, 804, doi: 10.1086/167237

—. 1993, in Astrophysical Masers, ed. A. W. Clegg & G. E. Nedoluha, Vol. 412, 73–82, doi: 10.1007/3-540-56343-1_216

Baan, W. A., Guesten, R., & Haschick, A. D. 1986, ApJ, 305, 830, doi: 10.1086/164297

Baan, W. A., Haschick, A., & Henkel, C. 1992a, AJ, 103, 728, doi: 10.1086/116097

Baan, W. A., Haschick, A. D., & Henkel, C. 1989, ApJ, 346, 680, doi: 10.1086/168050

Baan, W. A., Henkel, C., Loenen, A. F., Baudry, A., & Wiklind, T. 2008, A&A, 477, 747, doi: 10.1051/0004-6361:20077203

Baan, W. A., Rhoads, J., Fisher, K., Altschuler, D. R., & Haschick, A. 1992b, ApJL, 396, L99, doi: 10.1086/186526

Baan, W. A., Salzer, J. J., & LeWinter, R. D. 1998, ApJ, 509, 633, doi: 10.1086/306504

Baan, W. A., Wood, P. A. D., & Haschick, A. D. 1982, ApJL, 260, L49, doi: 10.1086/183868

Ball, J. A., Gottlieb, C. A., Lilley, A. E., & Radford, H. E. 1970, ApJL, 162, L203, doi: 10.1086/180654

Beichman, C. A., Neugebauer, G., Habing, H. J., Clegg, P. E., & Chester, T. J., eds. 1988, Infrared Astronomical Satellite (IRAS) Catalogs and Atlases.Volume 1: Explanatory Supplement., Vol. 1

Blyth, S., Baker, A. J., Holwerda, B., et al. 2016, in MeerKAT Science: On the Pathway to the SKA, 4, doi: 10.22323/1.277.0004

Bottinelli, L., Fraix-Burnet, D., Gouguenheim, L., et al. 1985a, A&A, 151, L7

Bottinelli, L., Gouguenheim, L., Le Squeren, A. M., et al. 1989, IAUC, 4928, 2

—. 1990, IAUC, 4977, 2

Bottinelli, L., Gouguenheim, L., Le Squeren, A. M., Dennefeld, M., & Paturel, G. 1985b, IAUC, 4106, 2

Bottinelli, L., Gouguenheim, L., Le Squeren, A. M., et al. 1986, IAUC, 4231, 2

—. 1987, IAUC, 4357, 3

Braun, R., Bonaldi, A., Bourke, T., Keane, E., & Wagg, J. 2019, arXiv, arXiv:1912.12699, doi: 10.48550/arXiv.1912.12699

Briggs, F. H. 1998, A&A, 336, 815, doi: 10.48550/arXiv.astro-ph/9710143

Brown, M. J. I., Moustakas, J., Smith, J. D. T., et al. 2014, ApJS, 212, 18, doi: 10.1088/0067-0049/212/2/18

Casoli, F., Dupraz, C., & Combes, F. 1992, A&A, 264, 55

Chambers, K. C., Magnier, E. A., Metcalfe, N., et al. 2016, arXiv, arXiv:1612.05560, doi: 10.48550/arXiv.1612.05560

Chen, P. S., Shan, H. G., & Gao, Y. F. 2007, AJ, 133, 496, doi: 10.1086/510130

Cheung, A. C., Rank, D. M., Townes, C. H., Thornton, D. D., & Welch, W. J. 1969, Natur, 221, 626, doi: 10.1038/221626a0

Chung, A., Narayanan, G., Yun, M. S., Heyer, M., & Erickson, N. R. 2009, AJ, 138, 858, doi: 10.1088/0004-6256/138/3/858

Churchwell, E., Witzel, A., Huchtmeier, W., et al. 1977, A&A, 54, 969

Cluver, M. E., Jarrett, T. H., Dale, D. A., et al. 2017, ApJ, 850, 68, doi: 10.3847/1538-4357/aa92c7

Coil, A. L., Blanton, M. R., Burles, S. M., et al. 2011, ApJ, 741, 8, doi: 10.1088/0004-637X/741/1/8

Condon, J. J., Anderson, M. L., & Helou, G. 1991, ApJ, 376, 95, doi: 10.1086/170258

Condon, J. J., Cotton, W. D., & Broderick, J. J. 2002, AJ, 124, 675, doi: 10.1086/341650

Condon, J. J., & Kaplan, D. L. 1998, ApJS, 117, 361, doi: 10.1086/313128

Cutri, R. M., Wright, E. L., Conrow, T., et al. 2021, yCat, II/328

da Cunha, E., Charlot, S., & Elbaz, D. 2008, MNRAS, 388, 1595, doi: 10.1111/j.1365-2966.2008.13535.x

Darling, J. 2005, in Astronomical Society of the Pacific Conference Series, Vol. 340, Future Directions in High Resolution Astronomy, ed. J. Romney & M. Reid, 216

Darling, J. 2007, ApJL, 669, L9, doi: 10.1086/523756

Darling, J., & Giovanelli, R. 2000, AJ, 119, 3003, doi: 10.1086/301403

—. 2001, AJ, 121, 1278, doi: 10.1086/319413

—. 2002a, ApJ, 572, 810, doi: 10.1086/340372

—. 2002b, AJ, 124, 100, doi: 10.1086/341166

—. 2006, AJ, 132, 2596, doi: 10.1086/508513

de Grijp, M. H. K., Keel, W. C., Miley, G. K., Goudfrooij, P., & Lub, J. 1992, A&AS, 96, 389

Diamond, P. J., Lonsdale, C. J., Lonsdale, C. J., & Smith, H. E. 1999, ApJ, 511, 178, doi: 10.1086/306681

Dickey, J. M., Planesas, P., Mirabel, I. F., & Kazes, I. 1990, AJ, 100, 1457, doi: 10.1086/115610

Driver, S. P., Liske, J., Davies, L. J. M., et al. 2019, Msngr, 175, 46, doi: 10.18727/0722-6691/5126

Du, W., Wu, H., Lam, M. I., et al. 2015, AJ, 149, 199, doi: 10.1088/0004-6256/149/6/199

Duc, P. A., Mirabel, I. F., & Maza, J. 1997, A&AS, 124, 533, doi: 10.1051/aas:1997205

Duffy, A. R., Meyer, M. J., Staveley-Smith, L., et al. 2012, MNRAS, 426, 3385, doi: 10.1111/j.1365-2966.2012.21987.x

Duncan, K., Conselice, C. J., Mundy, C., et al. 2019, ApJ, 876, 110, doi: 10.3847/1538-4357/ab148a

Elitzur, M. 1992, Astronomical masers, Vol. 170, doi: 10.1007/978-94-011-2394-5

Evans, A. S., Solomon, P. M., Tacconi, L. J., Vavilkin, T., & Downes, D. 2006, AJ, 132, 2398, doi: 10.1086/508416

Falstad, N., Aalto, S., König, S., et al. 2021, A&A, 649, A105, doi: 10.1051/0004-6361/202039291

Fernandez, M. X., Momjian, E., Salter, C. J., & Ghosh, T. 2010, AJ, 139, 2066, doi: 10.1088/0004-6256/139/5/2066

Fernández, X., van Gorkom, J. H., Hess, K. M., et al. 2013, ApJL, 770, L29, doi: 10.1088/2041-8205/770/2/L29

Fernández, X., Gim, H. B., van Gorkom, J. H., et al. 2016, ApJL, 824, L1, doi: 10.3847/2041-8205/824/1/L1

Ferreira, L., Conselice, C. J., Duncan, K., et al. 2020, ApJ, 895, 115, doi: 10.3847/1538-4357/ab8f9b

Foreman-Mackey, D., Hogg, D. W., Lang, D., & Goodman, J. 2013, PASP, 125, 306, doi: 10.1086/670067

Frogel, J. A., Gillett, F. C., Terndrup, D. M., & Vader, J. P. 1989, ApJ, 343, 672, doi: 10.1086/167738

Gallagher, M. J., Leroy, A. K., Bigiel, F., et al. 2018, ApJ, 858, 90, doi: 10.3847/1538-4357/aabad8

Gao, Y., & Solomon, P. M. 2004a, ApJS, 152, 63, doi: 10.1086/383003

—. 2004b, ApJ, 606, 271, doi: 10.1086/382999

García-Burillo, S., Usero, A., Alonso-Herrero, A., et al. 2012, A&A, 539, A8, doi: 10.1051/0004-6361/201117838

Ginsburg, A., & Goddi, C. 2019, AJ, 158, 208, doi: 10.3847/1538-3881/ab4790

Ginsburg, A., Sipőcz, B. M., Brasseur, C. E., et al. 2019, AJ, 157, 98, doi: 10.3847/1538-3881/aafc33

Giovanelli, R., Haynes, M. P., Kent, B. R., et al. 2005, AJ, 130, 2598, doi: 10.1086/497431

Glikman, E., Lacy, M., LaMassa, S., et al. 2018, ApJ, 861, 37, doi: 10.3847/1538-4357/aac5d8

Glowacki, M., Collier, J. D., Kazemi-Moridani, A., et al. 2022, ApJL, 931, L7, doi: 10.3847/2041-8213/ac63b0

Goldberger, J., Roweis, S., Hinton, G., & Salakhutdinov, R. 2005, Advances in Neural Information Processing Systems, 17, 513, doi: 10.1109/TCSVT.2013.2242640

Gordon, J. P., Zeiger, H. J., & Townes, C. H. 1955, PhRv, 99, 1264, doi: 10.1103/PhysRev.99.1264

Gowardhan, A., Spoon, H., Riechers, D. A., et al. 2018, ApJ, 859, 35, doi: 10.3847/1538-4357/aabccc

Gray, M. 2012, Maser Sources in Astrophysics

Haynes, M. P., Giovanelli, R., Kent, B. R., et al. 2018, ApJ, 861, 49, doi: 10.3847/1538-4357/aac956

Hekatelyne, C., Riffel, R. A., Storchi-Bergmann, T., et al. 2020, MNRAS, 498, 2632, doi: 10.1093/mnras/staa2479

Hekatelyne, C., Riffel, R. A., Sales, D., et al. 2018, MNRAS, 479, 3966, doi: 10.1093/mnras/sty1606

Helfand, D. J., White, R. L., & Becker, R. H. 2015, ApJ, 801, 26, doi: 10.1088/0004-637X/801/1/26

Helou, G., Soifer, B. T., & Rowan-Robinson, M. 1985, ApJL, 298, L7, doi: 10.1086/184556

Henkel, C., & Wilson, T. L. 1990, A&A, 229, 431

Herrero-Illana, R., Privon, G. C., Evans, A. S., et al. 2019, A&A, 628, A71, doi: 10.1051/0004-6361/201834088

Hess, K. M., Roberts, H., Dénes, H., et al. 2021, A&A, 647, A193, doi: 10.1051/0004-6361/202040019

Hodges-Kluck, E. J., Gallo, E., Seth, A., Greene, J., & Baldassare, V. 2020, ApJ, 898, 106, doi: 10.3847/1538-4357/ab9ffa

Hogg, D. W. 1999, arXiv, astro, doi: 10.48550/arXiv.astro-ph/9905116

Horellou, C., Casoli, F., Combes, F., & Dupraz, C. 1995, A&A, 298, 743

Imanishi, M., Baba, S., Nakanishi, K., & Izumi, T. 2023, arXiv, arXiv:2303.08178, doi: 10.48550/arXiv.2303.08178

Impey, C., & Bothun, G. 1997, ARA&A, 35, 267, doi: 10.1146/annurev.astro.35.1.267

Kandalian, R. A. 1996, Ap, 39, 237, doi: 10.1007/BF02071997

Kazes, I., & Baan, W. A. 1991, A&A, 248, L15

Kazes, I., Mirabel, I. F., & Combes, F. 1988, IAUC, 4629, 2

—. 1989, IAUC, 4856, 2

Kessler, M. F., Steinz, J. A., Anderegg, M. E., et al. 1996, A&A, 315, L27

Kewley, L. J., Heisler, C. A., Dopita, M. A., & Lumsden, S. 2001, ApJS, 132, 37, doi: 10.1086/318944

Kim, D. C., & Sanders, D. B. 1998, ApJS, 119, 41, doi: 10.1086/313148

Lee, J. C., Hwang, H. S., Lee, M. G., Kim, M., & Kim, S. C. 2011, MNRAS, 414, 702, doi: 10.1111/j.1365-2966.2011.18437.x

Litvak, M. M., McWhorter, A. L., Meeks, M. L., & Zeiger, H. J. 1966, PhRvL, 17, 821, doi: 10.1103/PhysRevLett.17.821

Lo, K. Y. 2005, ARA&A, 43, 625, doi: 10.1146/annurev.astro.41.011802.094927

Lockett, P., & Elitzur, M. 2008, ApJ, 677, 985, doi: 10.1086/533429

Lonsdale, C. J. 2002, in Cosmic Masers: From Proto-Stars to Black Holes, ed. V. Migenes & M. J. Reid, Vol. 206, 413

Lotz, J. M., Jonsson, P., Cox, T. J., et al. 2011, ApJ, 742, 103, doi: 10.1088/0004-637X/742/2/103

Mantha, K. B., McIntosh, D. H., Brennan, R., et al. 2018, MNRAS, 475, 1549, doi: 10.1093/mnras/stx3260

Martin, D. C., Fanson, J., Schiminovich, D., et al. 2005, ApJL, 619, L1, doi: 10.1086/426387

Martin, J. M., Bottinelli, L., Dennefeld, M., Gouguenheim, L., & Le Squeren, A. M. 1988, A&A, 201, L13

Martin, J.-M., Bottinelli, L., Gouguenheim, L., Le Squeren, A.-M., & Dennefeld, M. 1989, CRASM, 308, 287

Mauch, T., & Sadler, E. M. 2007, MNRAS, 375, 931, doi: 10.1111/j.1365-2966.2006.11353.x

Mauersberger, R., Wilson, T. L., & Henkel, C. 1986, A&A, 160, L13

McBride, J., Heiles, C., & Elitzur, M. 2013, ApJ, 774, 35, doi: 10.1088/0004-637X/774/1/35

McBride, J., Quataert, E., Heiles, C., & Bauermeister, A. 2014, ApJ, 780, 182, doi: 10.1088/0004-637X/780/2/182

McKellar, A. 1940, PASP, 52, 187, doi: 10.1086/125159

Mirabel, I. F., & Sanders, D. B. 1987, ApJ, 322, 688, doi: 10.1086/165764

Momjian, E., Romney, J. D., Carilli, C. L., & Troland, T. H. 2006, ApJ, 653, 1172, doi: 10.1086/508699

Morganti, R., de Zeeuw, P. T., Oosterloo, T. A., et al. 2006, MNRAS, 371, 157, doi: 10.1111/j.1365-2966.2006.10681.x

Mundy, C. J., Conselice, C. J., Duncan, K. J., et al. 2017, MNRAS, 470, 3507, doi: 10.1093/mnras/stx1238

National Academies of Sciences, Engineering, and Medicine (Astro2020). 2021, Pathways to Discovery in Astronomy and Astrophysics for the 2020s (Washington, DC: The National Academies Press), doi: 10.17226/26141

Norris, R. P., Gardner, F. F., Whiteoak, J. B., Allen, D. A., & Roche, P. F. 1989, MNRAS, 237, 673, doi: 10.1093/mnras/237.3.673

Obreschkow, D., Klöckner, H. R., Heywood, I., Levrier, F., & Rawlings, S. 2009, ApJ, 703, 1890, doi: 10.1088/0004-637X/703/2/1890

O'Leary, J. A., Moster, B. P., Naab, T., & Somerville, R. S. 2021, MNRAS, 501, 3215, doi: 10.1093/mnras/staa3746

Paglione, T. A. D., Wall, W. F., Young, J. S., et al. 2001, ApJS, 135, 183, doi: 10.1086/321785

Parra, R., Conway, J. E., Elitzur, M., & Pihlström, Y. M. 2005, A&A, 443, 383, doi: 10.1051/0004-6361:20052971

Perkins, F., Gold, T., & Salpeter, E. E. 1966, ApJ, 145, 361, doi: 10.1086/148775

Pihlström, Y. M., Conway, J. E., Booth, R. S., Diamond, P. J., & Polatidis, A. G. 2001, A&A, 377, 413, doi: 10.1051/0004-6361:20011107

Privon, G. C., Herrero-Illana, R., Evans, A. S., et al. 2015, ApJ, 814, 39, doi: 10.1088/0004-637X/814/1/39

Rifkin, R., & Klautau, A. 2004, Journal Of Machine Learning Research, 5, 101

Roberts, H., Darling, J., & Baker, A. J. 2021, ApJ, 911, 38, doi: 10.3847/1538-4357/abe944

Roberts, H., Darling, J., Hess, K., & Baker, A. J. in prep.

Robishaw, T., Quataert, E., & Heiles, C. 2008, ApJ, 680, 981, doi: 10.1086/588031

Rodriguez-Gomez, V., Genel, S., Vogelsberger, M., et al. 2015, MNRAS, 449, 49, doi: 10.1093/mnras/stv264

Rovilos, E., Diamond, P. J., Lonsdale, C. J., Lonsdale, C. J., & Smith, H. E. 2003, MNRAS, 342, 373, doi: 10.1046/j.1365-8711.2003.06566.x

Rybicki, G. B., & Lightman, A. P. 1979, Radiative processes in astrophysics

Sammut, C., & Webb, G. I. 2011, Encyclopedia of Machine Learning (Springer)

Samsonyan, A., Weedman, D., Lebouteiller, V., Barry, D., & Sargsyan, L. 2016, ApJS, 226, 11, doi: 10.3847/0067-0049/226/1/11

Sanders, D. B., Mazzarella, J. M., Kim, D. C., Surace, J. A., & Soifer, B. T. 2003, AJ, 126, 1607, doi: 10.1086/376841

Sanders, D. B., & Mirabel, I. F. 1996, ARA&A, 34, 749, doi: 10.1146/annurev.astro.34.1.749

Sanders, D. B., Soifer, B. T., Elias, J. H., Neugebauer, G., & Matthews, K. 1988, ApJL, 328, L35, doi: 10.1086/185155

Schawlow, A. L., & Townes, C. H. 1958, PhRv, 112, 1940, doi: 10.1103/PhysRev.112.1940

Shirley, Y. L. 2015, PASP, 127, 299, doi: 10.1086/680342

Skrutskie, M. F., Cutri, R. M., Stiening, R., et al. 2006, AJ, 131, 1163, doi: 10.1086/498708

Smith, H. E., Lonsdale, C. J., & Lonsdale, C. J. 1998, ApJ, 492, 137, doi: 10.1086/305020

Snyder, L. E., & Buhl, D. 1974, ApJL, 189, L31, doi: 10.1086/181457

Solomon, P. M., Downes, D., & Radford, S. J. E. 1992, ApJL, 387, L55, doi: 10.1086/186304

Solomon, P. M., Downes, D., Radford, S. J. E., & Barrett, J. W. 1997, ApJ, 478, 144, doi: 10.1086/303765

Sotnikova, Y. V., Wu, Z., Mufakharov, T. V., et al. 2022, MNRAS, 510, 2495, doi: 10.1093/mnras/stab3542

Staveley-Smith, L., Allen, D. A., Chapman, J. M., Norris, R. P., & Whiteoak, J. B. 1989, Natur, 337, 625, doi: 10.1038/337625a0

Staveley-Smith, L., Cohen, R. J., Chapman, J. M., Pointon, L., & Unger, S. W. 1987, MNRAS, 226, 689, doi: 10.1093/mnras/226.3.689

Staveley-Smith, L., Norris, R. P., Chapman, J. M., et al. 1992, MNRAS, 258, 725, doi: 10.1093/mnras/258.4.725

Staveley-Smith, L., & Oosterloo, T. 2015, in Advancing Astrophysics with the Square Kilometre Array (AASKA14), 167, doi: 10.22323/1.215.0167

Staveley-Smith, L., Unger, S. W., Cohen, R. J., Chapman, J. M., & Pointon, L. 1986, IAUC, 4248, 2

Stern, D., Eisenhardt, P., Gorjian, V., et al. 2005, ApJ, 631, 163, doi: 10.1086/432523

Stoughton, C., Lupton, R. H., Bernardi, M., et al. 2002, AJ, 123, 485, doi: 10.1086/324741

Strauss, M. A., & Huchra, J. 1988, AJ, 95, 1602, doi: 10.1086/114757

Suess, K. A., Darling, J., Haynes, M. P., & Giovanelli, R. 2016, MNRAS, 459, 220, doi: 10.1093/mnras/stw666

Taylor, N. 2007, Laser: The Inventor, the Nobel Laureate, the Thirty-year Patent War (iUniverse). https://books.google.com/books?id=1CKCPwAACAAJ

Toba, Y., Oyabu, S., Matsuhara, H., et al. 2014, ApJ, 788, 45, doi: 10.1088/0004-637X/788/1/45

van Cappellen, W. A., Oosterloo, T. A., Verheijen, M. A. W., et al. 2022, A&A, 658, A146, doi: 10.1051/0004-6361/202141739

Veilleux, S., Kim, D. C., & Sanders, D. B. 1999, ApJ, 522, 113, doi: 10.1086/307634

Veilleux, S., Kim, D. C., Sanders, D. B., Mazzarella, J. M., & Soifer, B. T. 1995, ApJS, 98, 171, doi: 10.1086/192158

Weaver, H., Williams, D. R. W., Dieter, N. H., & Lum, W. T. 1965, Natur, 208, 29, doi: 10.1038/208029a0

Wegner, G., Bernardi, M., Willmer, C. N. A., et al. 2003, AJ, 126, 2268, doi: 10.1086/378959

Weinreb, S., Meeks, M. L., & Carter, J. C. 1965, Natur, 208, 440, doi: 10.1038/208440a0

Werner, M. W. 2005, AdSpR, 36, 1048, doi: 10.1016/j.asr.2005.04.012

Whiteoak, J. B., & Gardner, F. F. 1974, ApL, 15, 211

Whiteoak, J. B., Gardner, F. F., & Hoglund, B. 1980, MNRAS, 190, 17P, doi: 10.1093/mnras/190.1.17P

Willett, K. W. 2011, PhD thesis, University of Colorado, Boulder

Willett, K. W. 2012, in Cosmic Masers - from OH to H0, ed. R. S. Booth, W. H. T. Vlemmings, & E. M. L. Humphreys, Vol. 287, 345–349, doi: 10.1017/S1743921312007284

Willett, K. W., Darling, J., Spoon, H. W. W., Charmandaris, V., & Armus, L. 2011a, ApJS, 193, 18, doi: 10.1088/0067-0049/193/1/18

—. 2011b, ApJ, 730, 56, doi: 10.1088/0004-637X/730/1/56

Wright, E. L., Eisenhardt, P. R. M., Mainzer, A. K., et al. 2010, AJ, 140, 1868, doi: 10.1088/0004-6256/140/6/1868

Yu, Z.-y. 2003, MNRAS, 338, 745, doi: 10.1046/j.1365-8711.2003.06085.x

Yun, M. S., Reddy, N. A., & Condon, J. J. 2001, ApJ, 554, 803, doi: 10.1086/323145

Zhang, J. S., Wang, J. Z., Di, G. X., et al. 2014, A&A, 570, A110, doi: 10.1051/0004-6361/201423556

Appendix A

Results of Optical Redshift Observing Campaign

We present the full results from the optical redshift observing campaigns as detailed in Chapter 3. Table A.1 presents the sources that were confirmed to be H I optical counterparts. Table A.2 presents the optical sources that either no redshift measurements was able to be made or the redshift measurement that was made did not match either the assumed redshift based on the OH or H I lines. Lastly, Table A.3 presents all emission lines measured for optical sources were a redshift determination was made. The measurements presented here are the observed central wavelengths for each lines and the errors on those fits.

Table A.1. H I confirmations from observing campaign

Radio Position (J2000)	AGC	z_{HI}	z_{OH}	Optical Position (J2000)	z_{opt}
001137.3+253334.0	102682	0.03494	0.21487	001137.3+253334.0	0.03475
001231.0+183339.0	104713	0.02445	0.20256	001231.0+183339.0	0.02462
001306.1+090959.0	103613	0.03562	0.21567	001306.1+090959.0	0.03561
001723.2+155705.0	101185	0.02566	0.20398	001723.2+155705.0	0.02574
003054.1+102432.0	105317	0.03656	0.21678	003054.1+102432.0	0.03666
004946.7+193032.0	104724	0.04215	0.22334	004946.7+193032.0	0.04250
010248.1+290358.0	114033	0.02800	0.20673	010248.1+290358.0	0.02797
012613.2+320808.0	...	0.01409	0.19040	012613.2+320808.0	0.01420
013016.0+101347.0	116371	0.01723	0.19408	013016.0+101347.0	0.01727
013748.8+121910.0	116176	0.03502	0.21497	013748.8+121910.0	0.03524
014258.9+311223.0	...	0.03529	0.21528	014258.9+311239.2	0.03530
014610.3+095824.0	114778	0.01737	0.19425	014610.3+095824.0	0.01730
015516.2+305005.0	...	0.02484	0.20302	015516.2+305005.0	0.02509
015855.7+352223.0	...	0.01428	0.19062	015855.6+352215.9	0.01442
015959.0+355223.0	...	0.04852	0.23082	015959.0+355223.0	0.04873
020037.3+325019.0	...	0.01513	0.19162	020037.3+325019.0	0.01541
020433.8+071705.0	124238	0.02485	0.20303	020433.8+071705.0	0.02500
023516.9+221140.0	123893	0.04864	0.23095	023516.9+221140.0	0.04867
024052.3+023624.0	125732	0.02215	0.19986	024052.3+023624.0	0.02222
024312.1+214152.0	125129	0.03179	0.21117	024312.1+214152.0	0.03193
025621.7+324703.0	124970	0.03943	0.22015	025621.7+324703.0	0.03950
025635.6+204548.0	125148	0.03326	0.21290	025635.6+204548.0	0.03318
074814.6+152724.0	171486	0.03922	0.21990	074814.6+152724.0	0.03896
080731.9+043137.0	188948	0.03112	0.21039	080731.9+043137.0	0.03184
080929.6+271416.0	749270	0.03689	0.21716	080929.6+271416.0	0.03708
084504.5+301012.0	189328	0.05129	0.23407	084504.5+301012.0	0.05148

Table A.1 (cont'd)

Radio Position (J2000)	AGC	z_{HI}	z_{OH}	Optical Position (J2000)	z_{opt}
092244.8+333157.0	198815	0.02545	0.20374	092244.8+333157.0	0.02532
094550.1+034011.0	198547	0.02405	0.20210	094550.1+034011.0	0.02423
094656.2+080538.0	198342	0.03163	0.21099	094656.2+080538.0	0.03204
101311.3+275505.0	749310	0.05346	0.23662	101311.3+275505.0	0.05357
103006.4+190937.0	208700	0.03362	0.21333	103006.4+190937.0	0.03352
103349.4+315925.0	208893	0.02462	0.20277	103349.4+315925.0	0.02478
104018.5+073705.0	208310	0.03259	0.21212	104018.5+073705.0	0.03308
105837.6+241458.0	749420	0.02265	0.20045	105837.6+241458.0	0.02303
110556.5+200012.0	219618	0.01925	0.19645	110556.5+200012.0	0.01959
111313.3+050916.0	219196	0.02730	0.20591	111313.3+050916.0	0.02697
112015.5+144336.0	215288	0.03998	0.22079	112015.5+144336.0	0.04031
115650.8+220839.0	219802	0.02277	0.20059	115650.8+220839.0	0.02292
120134.8+185945.0	229345	0.05053	0.23317	120134.8+185945.0	0.05059
122235.8+120927.0	220456	0.00003	0.17390	122400.0+121200.0	0.00028
125839.8+590715.0		0.02812	0.20688	125840.5+590726.9	0.02826
130923.6+334327.0	239240	0.01580	0.19240	130923.6+334327.0	0.01603
131140.5+283354.0	...	0.03873	0.21932	131140.8+283400.7	0.03852
131740.2+551731.0	...	0.02381	0.20181	131739.3+551717.5	0.02378
132016.1+312815.0	...	0.01577	0.19237	132016.6+312811.3	0.01583
134049.7+024903.0	238980	0.02325	0.20115	134049.7+024903.0	0.02309
134340.2+300749.0	239043	0.03920	0.21987	134341.1+300750.9	0.03943
141157.0+041810.0	249254	0.02436	0.20245	141157.0+041810.0	0.02476
141757.3+532841.0	...	0.01150	0.18736	141757.3+532841.0	0.01130
142933.3+010615.0	249427	0.02977	0.20881	142933.3+010615.0	0.03025
143947.5+113830.0	249187	0.05024	0.23283	143947.5+113830.0	0.05074
144455.2+243443.0	749484	0.03612	0.21626	144455.2+243443.0	0.03652

Table A.1 (cont'd)

Radio Position (J2000)	AGC	z_{HI}	z_{OH}	Optical Position (J2000)	z_{opt}
155242.0+174417.0	720264	0.05485	0.23825	155242.0+174417.0	0.05472
155637.5+160224.0	257961	0.01514	0.19163	155637.5+160224.0	0.01542
160631.8+153148.0	267962	0.03854	0.21910	160631.8+153148.0	0.03870
162315.3+154833.0	262411	0.03369	0.21341	162315.3+154833.0	0.03322
162934.0+040228.0	268208	0.05422	0.23751	162934.0+040228.0	0.05398
162942.5+055505.0	268223	0.03291	0.21249	162942.5+055505.0	0.03284
163220.1+064053.0	268227	0.04464	0.22626	163220.1+064053.0	0.04477
215307.9+134016.0	311380	0.03770	0.21811	215307.9+134016.0	0.03762
215450.0+454144.0	...	0.00114	0.17520	215450.0+454144.0	0.00118
220521.9+375529.0	...	0.04381	0.22529	220521.9+375522.3	0.04377
221308.3+375331.0	...	0.01632	0.19302	221308.3+375331.0	0.01657
221322.3+471236.0	...	0.03325	0.21289	221322.3+471236.0	0.03317
221329.7+452917.0	...	0.00362	0.17811	221329.7+452919.6	0.00360
221920.5+332122.0	...	0.01571	0.19231	221920.5+332122.0	0.01587
222217.8+444255.0	...	0.05443	0.23775	222218.7+444251.7	0.05455
222739.8+355608.0	...	0.02152	0.19912	222739.8+355608.0	0.02141
223610.4+335729.0	...	0.02208	0.19978	223610.4+335720.3	0.02001
224127.6+330405.0	...	0.02128	0.19884	224127.6+330405.0	0.02150
224312.1+321550.0	...	0.02971	0.20873	224312.2+321546.7	0.02993
224530.7+101213.0	320349	0.02583	0.20418	224530.7+101213.0	0.02623
224630.3+103845.0	323474	0.03732	0.21766	224630.3+103845.0	0.03743
225901.7+392936.0	...	0.02020	0.19757	225901.7+392936.0	0.02023
230037.4+305737.0	...	0.02308	0.20095	230037.5+305737.9	0.02328
230102.3+105407.0	336735	0.03871	0.21930	230102.3+105407.0	0.03912
232825.6+203641.0	335985	0.04603	0.22790	232825.6+203641.0	0.04605
232931.5+321635.0	...	0.01940	0.19663	232931.5+321635.0	0.01965

Table A.2. Ambiguous sources from observing campaign

Radio Position (J2000)	AGC	z_{HI}	z_{OH}	Optical Position (J2000)	z_{opt}	Category
001137.3+253334.0	102682	0.03494	0.21487	001133.2+253343.5	···	No Lines
002041.5+102030.0	105307	0.03767	0.21808	002041.5+102030.0	···	No Lines
002709.0+130915.0	105120	0.02151	0.19912	002709.0+130915.0	···	No Lines
002936.3+270147.0	102289	0.02313	0.20101	002936.3+270147.0	0.15303	Neither
002936.3+270147.0	102289	0.02313	0.20101	002934.9+270140.1	···	No Lines
003927.8+260429.0	102299	0.01758	0.19450	003927.8+260429.0	0.08306	Neither
004550.2+011916.0	103454	0.03633	0.21650	004550.2+011916.0	0.10667	Neither[a]
005040.4+030544.0	103359	0.04153	0.22261	005040.4+030544.0	···	No Lines
005141.2+193831.0	105024	0.04441	0.22599	005141.2+193831.0	···	No Lines
010440.5+341023.0	115327	0.03545	0.21548	010440.5+341023.0	···	No Lines
010440.5+341023.0	115327	0.03545	0.21548	010440.3+341029.9	···	No Lines
011604.4+110138.0	116345	0.02644	0.20490	011604.4+110138.0	0.02599	Neither[b]
013747.7+243212.0	113854	0.03417	0.21397	013747.7+243212.0	···	No Lines
014419.1+082446.0	114773	0.01833	0.19538	014421.5+082447.1	···	No Lines
014807.7+072950.0	114945	0.04765	0.22980	014807.7+072950.0	···	No Lines
014807.7+072950.0	114945	0.04765	0.22980	014806.3+072939.2	···	No Lines
015148.1+030450.0	116503	0.01157	0.18745	015148.1+030450.0	0.17067	Neither
020433.8+071705.0	124238	0.02485	0.20303	020432.0+071711.9	0.23808	Neither
020652.3+191326.0	125315	0.03525	0.21524	020652.3+191326.0	0.07634	Neither
091201.4+100025.0	198349	0.04947	0.23193	091201.4+100025.0	···	No Lines
091606.5+104259.0	198352	0.04805	0.23026	091606.5+104259.0	···	No Lines
092244.8+333157.0	198815	0.02545	0.20374	092244.2+333206.1	···	No Lines
094552.3+102156.0	198478	0.04012	0.22095	094552.3+102156.0	···	No Lines
094552.3+102156.0	198478	0.04012	0.22095	094552.3+102156.0	0.16081	Neither
100400.2+151501.0	205107	0.01348	0.18969	100400.2+151501.0	···	No Lines
101101.1+274012.0	749309	0.01445	0.19082	101101.1+274012.0	···	No Lines

Table A.2 (cont'd)

Radio Position (J2000)	AGC	$z_{\rm HI}$	$z_{\rm OH}$	Optical Position (J2000)	$z_{\rm opt}$	Category
101101.1+274012.0	749309	0.01445	0.19082	101101.1+273949.3	⋯	No Lines
101101.1+274012.0	749309	0.01445	0.19082	101100.3+274036.0	⋯	No Lines
103006.4+190937.0	208700	0.03362	0.21333	103008.3+190937.5	0.13789	Neither
113034.2+322208.0	219835	0.02149	0.19909	113033.9+322144.4	⋯	No Lines
113034.2+322208.0	219835	0.02149	0.19909	113032.8+322148.4	⋯	No Lines
113034.2+322208.0	219835	0.02149	0.19909	113032.6+322127.6	⋯	No Lines
115250.6+113024.0	213364	0.04302	0.22436	115250.6+113024.0	⋯	No Lines
115634.9+234630.0	219806	0.01683	0.19362	115634.9+234630.0	⋯	No Lines
120134.8+185945.0	229345	0.05053	0.23317	120136.5+185915.4	0.05070	Neither[b]
122843.2+145957.0	7602	0.00556	0.18039	131122.5+291506.3	⋯	No Lines
123657.0+341532.0	229366	0.02250	0.20027	123657.0+341532.0	⋯	No Lines
124119.2+013253.0	229183	0.00562	0.18046	124119.2+013253.0	⋯	No Lines
124119.2+013253.0	229183	0.00562	0.18046	124118.1+013135.1	⋯	No Lines
131122.5+291455.0	⋯	0.00887	0.18427	131122.2+291451.5	⋯	No Lines
131250.8+291122.0	⋯	0.05773	0.24163	131251.3+291115.2	⋯	No Lines
132016.2+552349.0	⋯	0.02646	0.20493	132016.2+552349.0	⋯	No Lines
133207.1+283320.0	⋯	0.06057	0.24496	133207.1+283320.0	0.27881	Neither
133207.1+283320.0	⋯	0.06057	0.24496	133208.0+283322.9	⋯	No Lines
133449.2+284813.0	⋯	0.06371	0.24865	133450.8+284835.4	⋯	No Lines
133829.5+291103.0	⋯	0.05964	0.24387	133829.3+291112.6	⋯	No Lines
133829.5+291103.0	⋯	0.05964	0.24387	133827.9+291107.7	0.03706	Neither
134144.0+283108.0	⋯	0.05828	0.24227	134144.0+283108.0	⋯	No Lines
134737.8+154423.0	238608	0.03693	0.21721	134737.8+154423.0	0.11854	Neither
153426.0+173747.0	746831	0.05869	0.24275	153426.0+173747.0	⋯	No Lines
155449.3+155615.0	257954	0.01711	0.19395	155449.3+155615.0	⋯	No Lines
215307.9+134016.0	311380	0.03770	0.21811	215306.9+134016.9	0.28649	Neither[a]

Table A.2 (cont'd)

Radio Position (J2000)	AGC	z_{HI}	z_{OH}	Optical Position (J2000)	z_{opt}	Category
215307.9+134016.0	311380	0.03770	0.21811	215308.1+134049.1	···	No Lines
215307.9+134016.0	311380	0.03770	0.21811	215305.9+133957.7	···	No Lines
220916.8+161348.0	323280	0.02540	0.20367	220916.8+161348.0	0.17877	Neither
223118.8+132027.0	323368	0.04883	0.23118	223118.8+132027.0	0.15109	Neither[a]
223502.0+103825.0	323447	0.04032	0.22119	223502.0+103825.0	···	No Lines
223502.0+103825.0	323447	0.04032	0.22119	223501.7+103826.7	···	No Lines
230012.4+311805.0	333348	0.02244	0.20020	230012.4+311805.0	0.12096	Neither
230032.3+304212.0	···	0.00268	0.17701	230032.3+304212.0	···	No Lines

[a] While optical redshifts are provided for these sources, we note that the redshift is only calculated from only one emission line, resulting in a large uncertainty.

[b] While these redshifts were close to the expected redshift, other sources were found closer to the radio source and with better matched redshifts. These sources may possibly be contributing to the radio signal but are not expected to be the primary emitters.

Note. — Ambiguous sources were categorized into two groups: those whose optical spectra showed no identifiable emission lines to determine a redshift (No Lines) and those where a redshift could be determined but it matched neither the expected OH or H 1 redshift (Neither).

Table A.3. Optical emission line center measurements for candidate OHMs

Optical Position (J2000)	NII (6549 Å)	Hα (6563 Å)	NII (6583 Å)	SII (6717 Å)	SII (6731 Å)
001137.3+253334.0	⋯	6790.836±0.027	⋯	6949.352±0.068	⋯
001231.0+183339.0	⋯	6724.385±0.003	6745.107±0.018	6882.014±0.013	6895.573±0.029
001306.1+090959.0	⋯	6796.524±0.018	⋯	6954.956±0.054	⋯
001723.2+155705.0	⋯	6731.734±0.040	⋯	⋯	⋯
002936.3+270147.0	⋯	7567.133±0.011	7589.448±0.027	⋯	⋯
003054.1+102432.0	6788.425±0.008	6803.397±0.001	6824.705±0.002	6962.511±0.005	6977.297±0.006
003927.8+260429.0	⋯	7107.937±0.006	7130.587±0.034	7278.687±0.092	⋯
003924.7+260414.4	⋯	7895.696±0.028	7921.047±0.051	8076.975±0.463	⋯
004550.2+011916.0	⋯	7262.858±0.018	⋯	⋯	⋯
004946.7+193032.0	⋯	6841.702±0.006	6861.413±0.063	7000.906±0.023	7015.523±0.040
010248.1+290358.0	⋯	6746.346±0.095	⋯	⋯	⋯
011604.4+110138.0	⋯	6733.361±0.091	⋯	⋯	⋯
011604.0+110136.6	7875.832±0.280	7908.789±0.069	⋯	8075.733±0.319	⋯
012613.2+320808.0	⋯	6656.006±0.017	⋯	⋯	⋯
013016.0+101347.0	⋯	6676.147±0.001	6697.166±0.017	6832.314±0.011	6847.000±0.012
013748.8+121910.0	6777.917±0.091	6794.051±0.002	6814.966±0.018	6952.851±0.012	6967.504±0.014
014258.9+311239.2	6778.899±0.092	6794.477±0.018	6815.479±0.089	6953.802±0.079	6968.930±0.062

Table A.3 (cont'd)

Optical Position (J2000)	NII (6549 Å)	Hα (6563 Å)	NII (6583 Å)	SII (6717 Å)	SII (6731 Å)
014610.3+095824.0	···	6676.339±0.002	6697.582±0.019	6832.953±0.008	6847.298±0.015
015148.1+030450.0	···	7682.908±0.037	7708.580±0.051	···	···
015516.2+305005.0	···	6727.454±0.005	6748.271±0.026	6884.555±0.016	6899.422±0.028
015855.6+352215.9	6642.735±0.014	6657.416±0.001	6678.258±0.006	6813.321±0.005	6827.599±0.006
015959.0+355223.0	6865.174±0.018	6882.631±0.002	6904.510±0.013	7043.333±0.009	7058.378±0.018
020037.3+325019.0	···	6663.928±0.004	···	6820.359±0.028	6833.503±0.066
020433.8+071705.0	···	6726.907±0.081	···	···	···
020432.0+071711.9	···	8125.265±0.059	8151.177±0.235	···	···
020652.3+191326.0	···	7063.794±0.022	7086.572±0.098	7227.024±0.116	7246.205±0.096
023516.9+221140.0	···	6882.219±0.018	···	7043.601±0.105	7058.906±0.208
024052.3+023624.0	···	6708.606±0.059	···	···	···
024312.1+214152.0	···	6772.316±0.004	6792.926±0.014	6931.810±0.018	6944.346±0.016
025621.7+324703.0	6806.108±0.033	6822.035±0.005	6843.129±0.018	6983.090±0.021	6996.468±0.024
025635.6+204548.0	···	6780.541±0.002	6802.523±0.028	6940.459±0.017	6955.266±0.018
074814.6+152724.0	6803.375±0.004	6818.478±0.000	6839.983±0.001	6978.281±0.003	6993.111±0.003
080731.9+043137.0	···	6771.727±0.012	···	···	···
080929.6+271416.0	···	6806.135±0.048	···	···	···

Table A.3 (cont'd)

Optical Position (J2000)	NII (6549 Å)	Hα (6563 Å)	NII (6583 Å)	SII (6717 Å)	SII (6731 Å)
084504.5+301012.0	···	6900.662±0.035	···	7064.679±0.174	···
092244.8+333157.0	···	6728.937±0.030	···	···	···
094550.1+034011.0	···	6721.788±0.029	···	···	···
094552.3+102156.0	···	7618.168±0.015	7642.750±0.081	7795.641±0.038	···
094656.2+080538.0	···	6773.062±0.016	···	···	···
101311.3+275505.0	···	6914.341±0.058	···	···	···
103006.4+190937.0	···	6782.767±0.075	···	···	···
103008.3+190937.5	···	7467.775±0.031	7491.264±0.055	···	···
103349.4+315925.0	6710.042±0.046	6725.417±0.001	6745.991±0.014	6882.964±0.024	6896.845±0.033
104018.5+073705.0	···	6779.890±0.011	···	6938.972±0.062	6953.837±0.065
105837.6+241458.0	···	6713.913±0.064	···	···	···
110556.5+200012.0	···	6691.348±0.051	···	···	···
111313.3+050916.0	···	6739.780±0.069	···	···	···
112015.5+144336.0	···	6827.379±0.016	6848.803±0.157	6988.137±0.134	7003.229±0.115
115650.8+220839.0	···	6713.207±0.042	6733.521±0.172	···	···
120134.8+185945.0	6880.231±0.013	6894.832±0.002	6916.682±0.004	7056.008±0.010	7073.131±0.026
120136.5+185915.4	···	6895.558±0.028	6916.699±0.037	7056.479±0.042	···

Table A.3 (cont'd)

Optical Position (J2000)	NII (6549 Å)	Hα (6563 Å)	NII (6583 Å)	SII (6717 Å)	SII (6731 Å)
122400.0+121200.0	···	6564.638±0.000	6585.001±0.006	6718.040±0.003	6732.348±0.004
125840.5+590726.9	···	6748.291±0.008	···	6906.483±0.055	6920.257±0.064
130923.6+334327.0	···	6667.982±0.018	···	···	···
131140.8+283400.7	···	6815.576±0.057	···	6974.350±0.136	6987.888±0.104
131739.3+551717.5	···	6718.889±0.048	···	···	···
132016.6+312811.3	···	6666.679±0.032	···	···	···
133207.1+283320.0	···	8392.604±0.122	8418.508±0.308	8594.756±0.533	···
133827.9+291107.7	···	6806.020±0.092	···	7074.575±0.251	···
134049.7+024903.0	6698.220±0.028	6714.325±0.001	6735.729±0.012	6872.069±0.013	6886.726±0.013
134341.1+300750.9	···	6821.605±0.073	···	···	···
134737.8+154423.0	···	7340.745±0.011	7364.118±0.042	7512.767±0.057	7530.442±0.074
140340.3+295456.0	···	7735.033±0.051	7761.521±0.053	7917.977±0.110	7935.040±0.159
141157.0+041810.0	6710.227±0.010	6725.270±0.001	6746.386±0.003	6883.198±0.009	6897.520±0.013
141757.3+532841.0	···	6636.946±0.058	···	···	···
142933.3+010615.0	···	6761.330±0.002	6782.592±0.015	6919.177±0.010	6934.478±0.013
143947.5+113830.0	···	6895.811±0.018	···	···	···
144455.2+243443.0	···	6802.500±0.012	···	6961.410±0.058	6976.700±0.049

Table A.3 (cont'd)

Optical Position (J2000)	NII (6549 Å)	Hα (6563 Å)	NII (6583 Å)	SII (6717 Å)	SII (6731 Å)
155242.0+174417.0	6906.518±0.008	6921.940±0.000	6944.419±0.003	7084.664±0.004	7099.453±0.005
155637.5+160224.0	⋯	6664.022±0.001	6685.038±0.014	6820.373±0.009	6835.213±0.014
160631.8+153148.0	⋯	6816.757±0.014	⋯	⋯	⋯
162315.3+154833.0	6765.345±0.025	6780.816±0.001	6802.155±0.010	6939.541±0.007	6954.636±0.010
162934.0+040228.0	⋯	6917.050±0.001	6939.019±0.010	7080.537±0.007	7094.123±0.011
162942.5+055505.0	6762.892±0.015	6778.313±0.000	6799.643±0.005	6936.725±0.004	6951.632±0.006
163220.1+064053.0	⋯	6856.622±0.007	⋯	7016.584±0.040	7032.606±0.046
215307.9+134016.0	6793.868±0.023	6809.704±0.003	6831.446±0.020	6968.809±0.012	6984.000±0.016
215306.9+134016.9	⋯	8443.002±0.057	⋯	⋯	⋯
215450.0+454144.0	⋯	6570.564±0.003	⋯	6724.313±0.042	6739.662±0.025
220521.9+375522.3	⋯	6850.049±0.011	⋯	7009.893±0.030	7025.752±0.062
220916.8+161348.0	⋯	7736.046±0.019	7759.919±0.064	7918.257±0.061	⋯
221306.3+011627.0	7748.909±0.353	7772.673±0.072	⋯	⋯	⋯
221308.3+375331.0	⋯	6671.551±0.041	⋯	⋯	⋯
221322.3+471236.0	⋯	6780.503±0.004	6802.188±0.012	6939.168±0.017	6952.054±0.027
221329.7+452919.6	⋯	6586.395±0.022	⋯	⋯	⋯
221920.5+332122.0	6651.900±0.023	6666.954±0.001	6687.641±0.010	6822.963±0.007	6837.575±0.008

Table A.3 (cont'd)

Optical Position (J2000)	NII (6549 Å)	Hα (6563 Å)	NII (6583 Å)	SII (6717 Å)	SII (6731 Å)
222218.7+444251.7	···	6920.797±0.003	6943.053±0.025	7082.750±0.015	7098.470±0.021
222739.8+355608.0	6687.500±0.035	6703.319±0.003	6724.715±0.016	6860.928±0.010	6875.335±0.019
223118.8+132027.0	···	7554.371±0.032	···	···	···
223610.4+335720.3	6674.840±0.005	6694.147±0.004	···	···	···
224127.6+330405.0	···	6703.909±0.006	···	6862.002±0.016	···
224312.2+321546.7	···	6759.213±0.004	6780.420±0.018	6917.239±0.020	6931.881±0.026
224530.7+101213.0	6722.558±0.008	6734.917±0.001	6755.632±0.001	6892.834±0.007	6907.249±0.006
224630.3+103845.0	···	6808.431±0.030	···	6969.128±0.190	···
225901.7+392936.0	···	6695.558±0.000	6716.301±0.008	6852.433±0.003	6866.617±0.004
230012.4+311805.0	···	7356.626±0.022	7379.455±0.070	7529.320±0.062	7544.968±0.104
230037.5+305737.9	···	6715.547±0.031	···	···	···
230102.3+105407.0	···	6819.522±0.029	···	···	···
232825.6+203641.0	6850.428±0.050	6865.049±0.010	6887.087±0.021	7026.292±0.049	7041.274±0.053
232931.5+321635.0	···	6691.774±0.002	6712.833±0.013	6848.049±0.009	6862.326±0.009

Appendix B

Full OHM Catalog

Below, the full compiled OHM catalog is presented in four tables. Table B.1 presents basic information about each OHM, including coordinates, redshift, OH luminosity, and spectral type. Tables B.3 and B.2 present crossmatched information from the AllWISE catalog (Cutri et al. 2021) and IRAS PSC and FSC catalogs (Beichman et al. 1988). Lastly, Table B.4 presents 21cm radio components from the NRAO VLA Sky Survey (NVSS; Condon & Kaplan 1998) and Faint Images of the Radio Sky at Twenty-Centimeters survey (FIRST; Helfand et al. 2015). A description of each table column can be found in Table 6.1.

Table B.1. OHM catalog of confirmed sources with general information

Common Name	RA (J2000)	Dec (J2000)	z	$\log L_{\rm OH}$ ($L_\odot$)	ΔV (km s^{-1})	Ref.	Type	Type Ref.
IRAS 00057+4021	00 08 20.44	+40 37 55.99	0.0447	$1.99^{\rm n}$	...	16, 25	Sy2	2
IRAS 00335-2732	00 36 00.37	−27 15 33.80	0.0693	$2.69^{\rm n}$	...	13, 16	C	2
AGC 102299	00 39 24.70	+26 04 14.41	0.2031	2.91	59	1		
IRAS 00461-0728	00 48 39.50	−07 12 20.99	0.2427	3.57	135	38		
UGC 00545	00 53 34.92	+12 41 35.92	0.0589	$1.87^{\rm n}$	...	13, 16	Sy1	11
AGC 116345	01 16 04.00	+11 01 36.59	0.2051	3.30	206	1		
IRAS 01298-0744	01 32 21.40	−07 29 08.02	0.1362	3.77	124	38	H	16
IRAS 01355-1814	01 37 57.40	−17 59 21.01	0.1920	2.80	52	38	H	16
IRAS 01364-1042	01 38 52.86	−10 27 11.59	0.0482	$2.08^{\rm n}$	...	12, 16	L	3, 15, 16
III Zw 035	01 44 30.54	+17 06 08.78	0.0274	2.74	270	16, 34	H, L, Sy2	2, 12, 15
IRAS F01472+2347	01 50 01.57	+24 02 35.81	0.2044	3.61	613	37		
IRAS 01562+2527	01 59 02.60	+25 42 36.79	0.1657	3.31	218	16	H	3
IRAS 01569-2939	01 59 13.80	−29 24 34.99	0.1400	3.92	287	38	Sy1	9
AGC 181310	02 26 57.65	+28 24 57.49	0.2148	3.29	46	37		
IRAS 02483+4302	02 51 35.83	+43 15 11.41	0.0514	$2.57^{\rm n}$	...	16, 26	L	2
IRAS 02524+2046	02 55 17.12	+20 58 57.68	0.1814	3.80	76	16	H	3
UGC 02553	03 08 30.73	+20 46 20.10	0.0274	$1.36^{\rm n}$	...	13, 16	H	2

Table B.1 (cont'd)

Common Name	RA (J2000)	Dec (J2000)	z	$\log L_{OH}$ ($L_\odot$)	ΔV (km s^{-1})	Ref.	Type	Type Ref.
IRAS 03158+4227	03 19 12.40	+42 38 28.00	0.1346	3.39	803	20		
IRAS 03260-1422	03 28 24.33	−14 12 06.80	0.0434	2.07^{n}	...	16, 26	H	2
Nkalakatha	03 30 46.27	−27 55 17.51	0.5245	3.84	459	19		
IRAS 03521+0028	03 54 42.22	+00 37 03.22	0.1519	2.50	59	16	L	3, 13
IRAS 03566+1647	03 59 28.49	+16 56 24.50	0.1335	2.38	48	16	Sy2	3
IRAS 04121+0223	04 14 47.10	+02 30 36.00	0.1224	2.39	209	15	H	3
UGC 03097	04 35 48.37	+02 15 28.98	0.0119	$0.51^{k,n}$	100	16, 36	H	2
ESO 203-IG 001	04 46 49.52	−48 33 29.99	0.0529	2.95	39	16, 36		
IRAS 05100-2425	05 12 09.18	−24 21 56.20	0.0335	2.14^{n}	117	16, 36	L	2
UGC 03351	05 45 47.88	+58 42 03.89	0.0149	$0.89^{k,n}$	...	16, 29	Sy2	2
IRAS 06206-3646	06 22 22.61	−36 47 45.10	0.1080	3.41	382	16, 27		
IRAS 06487+2208	06 51 45.74	+22 04 27.30	0.1433	2.94	211	14	H	3
IRAS 07163+0817	07 19 05.50	+08 12 06.98	0.1110	2.43	24	15	H	3
IRAS F07556+2859	07 58 45.90	+28 51 33.01	0.1260	2.66	63	38		
IRAS 07572+0533	07 59 59.75	+05 24 51.30	0.1900	2.80	156	15	L	3
IRAS 08071+0509	08 09 47.21	+05 01 09.01	0.0522	2.30^{n}	...	12, 16	C	2
IRAS 08201+2801	08 23 12.61	+27 51 39.89	0.1678	3.51	205	15	H, L	1, 3, 5

Table B.1 (cont'd)

Common Name	RA (J2000)	Dec (J2000)	z	$\log L_{\rm OH}$ ($L_\odot$)	ΔV (km s^{-1})	Ref.	Type	Type Ref.
IRAS 08279+0956	08 30 39.32	+09 46 36.91	0.2086	3.28	207	15	L	3
IRAS 08449+2332	08 47 50.22	+23 21 10.19	0.1515	2.67	97	15	H	3
IRAS 08474+1813	08 50 18.34	+18 02 01.21	0.1454	2.75	409	15	Sy2	3
IRAS 09039+0503	09 06 34.04	+04 51 27.61	0.1248	2.88	212	15	H, L	1, 3, 13
AGC 193884	09 32 38.30	+16 11 57.23	0.1910	3.42	387	1, 21		
IRAS 09531+1430	09 55 49.98	+14 16 06.71	0.2151	3.47	256	15	H, Sy2	3
IRAS 09539+0857	09 56 34.34	+08 43 06.20	0.1289	3.53	317	15	L, Sy2	3, 13
ESO 374-IG 032	10 06 04.61	−33 53 06.00	0.0342	2.96	63	16, 36	A	10
IRAS 10036+2740	10 06 26.36	+27 25 46.88	0.1655	2.55	65	16	A	1
IRAS 10173+0828	10 20 00.21	+08 13 33.89	0.0491	2.73	39	16, 30	A, H	10
IRAS 10339+1548	10 36 37.97	+15 32 41.50	0.1972	2.71	40	15	Sy2	3
IRAS 10378+1109	10 40 29.18	+10 53 17.99	0.1363	3.59	188	16, 27	H, L, Sy1	1, 3, 13, 16
IRAS 10485-1447	10 51 03.07	−15 03 21.82	0.1330	2.99^{n}	...	13, 16	L	16
IRAS 10597+5926	11 02 47.40	+59 10 43.00	0.1402	3.90	138	23, 38		
ARP 148	11 03 53.85	+40 51 00.11	0.0345	2.06	...	10, 16	C	2
IRAS 11029+3130	11 05 37.54	+31 14 32.10	0.1986	3.03	89	15	L	3, 5
IRAS 11069+2711	11 09 38.89	+26 54 56.02	0.0703	nan0^{n}	...	7, 16	H	2

Table B.1 (cont'd)

Common Name	RA (J2000)	Dec (J2000)	z	$\log L_{\rm OH}$ ($L_\odot$)	ΔV (km s^{-1})	Ref.	Type	Type Ref.
AGC 219215	11 11 25.06	+05 20 46.00	0.2252	3.26	45	37		
IRAS 11180+1623	11 20 41.78	+16 06 56.59	0.1660	2.39	127	16	L	16
NGC 3690	11 28 32.20	+58 33 51.01	0.0104	1.45	$210^{\rm e}$	3, 16	A, H	2
ESO 320-G 030	11 53 11.70	−39 07 49.01	0.0108	1.62	87	16, 32, 36	H	7
IRAS 11524+1058	11 55 05.14	+10 41 22.81	0.1787	3.04	279	15	L	3
AGC 219828	11 55 14.71	+31 30 02.88	0.2160	$3.11^{\rm n}$	216	21		
IRAS 12005+0009	12 03 04.43	−00 07 27.70	0.1222	2.67	82	16	L	14
IRAS 12018+1941	12 04 24.55	+19 25 09.98	0.1686	2.64	352	16, 29	L, Sy2	1, 2
IRAS 12032+1707	12 05 47.74	+16 51 08.21	0.2178	4.20	853	15	L	3, 13
IRAS 12071-0444	12 09 45.10	−05 01 14.02	0.1284	2.44	95	38	Sy2	16
IRAS F12072+3054	12 09 48.20	+30 37 47.50	0.1700	3.04	123	21, 31		
IRAS 12112+0305	12 13 45.98	+02 48 40.10	0.0730	3.02	315	16, 27	H, L	1, 2, 8
AGC 229487	12 15 48.81	+35 10 59.59	0.1661	$2.67^{\rm n}$	35	21		
IRAS 12162+1047	12 18 47.77	+10 31 14.09	0.1465	2.30	105	16	Sy2	14
NGC 4355	12 26 54.62	−00 52 39.40	0.0073	$-0.04^{\rm k}$	70	16, 28	Sy2	2
MRK 0231	12 56 14.23	+56 52 25.21	0.0422	2.93	$300^{\rm e}$	3, 16	Sy1	2, 8
IRAS 12548+2403	12 57 20.03	+23 47 46.28	0.1317	2.42	102	16	C	14

Table B.1 (cont'd)

Common Name	RA (J2000)	Dec (J2000)	z	$\log L_{\rm OH}$ ($L_\odot$)	ΔV (km s^{-1})	Ref.	Type	Type Ref.
IRAS 13126+2452	13 15 03.53	+24 37 07.93	0.0112	$0.27^{k,n}$	...	4, 16	H, L	1, 2
IRAS F13218+0552	13 24 19.89	+05 37 04.58	0.2051	3.50	314	16	Sy2	1
IRAS 13254+4754	13 27 32.72	+47 39 03.49	0.0609	1.97^{n}	...	16, 22	C, H	1, 2
MRK 0273	13 44 42.08	+55 53 12.98	0.0378	2.60	100^{e}	9, 16	Sy2	2, 8
IRAS 13451+1232	13 47 33.41	+12 17 24.11	0.1224	2.46	300^{e}	16, 17	H, Sy2	1, 2, 8
IRAS F14014+3009	14 03 40.35	+29 54 56.41	0.1786	3.26	216	1, 21		
IRAS 14043+0624	14 06 49.82	+06 10 36.01	0.1132	2.16	54	16	Sy1	16
IRAS 14059+2000	14 08 18.73	+19 46 22.69	0.1237	3.40	161	16	A, H	1, 14
IRAS 14070+0525	14 09 31.26	+05 11 31.42	0.2644	4.19	...	5, 16	Sy2	8
IRAS 14531+0636	14 55 37.39	+06 24 37.40	0.2300	3.06	83	37		
IRAS 14553+1245	14 57 42.46	+12 33 21.10	0.1245	2.32	77	16	H	1, 14
IRAS 14586+1431	15 01 02.22	+14 20 02.94	0.1477	3.46	369	16		
NGC 5861	15 09 16.09	−11 19 18.01	0.0063	0.28^{k}	75^{e}	6, 16	Sy2	2
CGCG 049-057	15 13 13.09	+07 13 32.02	0.0130	1.08^{n}	142	10, 16	H	1, 2
IRAS 15179+3956	15 19 47.11	+39 45 37.19	0.0476	1.87^{n}	...	12, 16	H	2
IRAS 15224+1033	15 24 51.13	+10 22 49.01	0.1346	3.09	31	15	H, L	1, 3
IRAS 15233+0533	15 25 49.55	+05 22 48.61	0.0540	$\mathrm{nan}0^{n}$	...	7, 16	L	2

Table B.1 (cont'd)

Common Name	RA (J2000)	Dec (J2000)	z	$\log L_{OH}$ ($L_\odot$)	ΔV (km s^{-1})	Ref.	Type	Type Ref.
IRAS 15250+3609	15 26 59.41	+35 58 37.31	0.0552	2.65	...	11, 16	H, L	1, 2, 15
IRAS 15247-0945	15 27 27.73	−09 55 42.10	0.0396	2.17^{n}	...	16, 26	L	2
Arp 220	15 34 57.24	+23 30 11.41	0.0181	2.62	108	2, 16	L, Sy2	2, 8, 15
AGC 257959	15 55 37.94	+14 39 05.62	0.2036	3.60	206	37		
IRAS 15587+1609	16 01 02.88	+16 01 02.39	0.1372	3.31	176	15	H	3
IRAS 16090-0139	16 11 40.40	−01 47 07.01	0.1336	3.52	493	38	L	16
IRAS 16100+2528	16 12 05.39	+25 20 23.32	0.1324	2.34	46	15	L	3
IRAS 16255+2801	16 27 33.71	+27 54 33.52	0.1336	2.62	79	15	H	3
IRAS 16300+1558	16 32 21.41	+15 51 45.79	0.2417	2.91	131	14	L, Sy2	3, 5
IRAS 16399-0937	16 42 40.12	−09 43 13.30	0.0270	1.75^{n}	...	16, 33	H, L	2
IRAS 17160+2006	17 18 14.39	+20 03 08.50	0.1098	2.45	76	16		
IRAS 17208-0014	17 23 21.96	−00 17 00.82	0.0428	3.11	175^{e}	8, 16	H, L	2, 4, 8
UGC 11035	17 54 29.41	+32 53 14.21	0.0260	1.06^{n}	...	16, 24	H	2
IRAS 17540+2935	17 55 56.11	+29 35 26.41	0.1081	1.82	161	14	L	3
IRAS 18368+3549	18 38 35.41	+35 52 19.99	0.1162	2.92	421	14	Sy2	3
IRAS 18544-3718	18 57 52.62	−37 14 40.31	0.0734	2.49	22	16, 27		
IRAS 18588+3517	19 00 41.17	+35 21 26.32	0.1067	2.58	64	14	H	3

Table B.1 (cont'd)

Common Name	RA (J2000)	Dec (J2000)	z	$\log L_{\rm OH}$ ($L_\odot$)	ΔV (km s^{-1})	Ref.	Type	Type Ref.
IRAS 20100-4156	20 13 29.56	−41 47 35.09	0.1296	4.14	106	16, 27, 35	A, H	4
IRAS 20248+1734	20 27 08.12	+17 44 21.70	0.1218	2.60	177	14	H	3
IRAS 20286+1846	20 30 54.48	+18 56 37.61	0.1358	3.47	224	14	L	3
IRAS 20450+2140	20 47 14.34	+21 51 12.49	0.1284	2.30	144	14	H	3
UGC 11643	20 51 25.92	+18 58 04.30	0.0291	$1.16^{\rm n}$	...	12, 16	H	2
II Zw 096	20 57 23.63	+17 07 44.18	0.0355	2.22	112	16, 36	H	2
IRAS 21077+3358	21 09 47.27	+34 10 25.72	0.1767	2.42	243	14	L	3
IRAS 21272+2514	21 29 29.40	+25 27 54.40	0.1508	3.72	263	14	Sy2	3
UGC 11898	22 04 36.13	+42 19 38.21	0.0143	1.11	420	16	C	2
IRAS 22055+3024	22 07 49.67	+30 39 39.71	0.1269	2.80	92	15	L	3
IRAS F22088-1831W	22 11 33.81	−18 17 06.50	0.1700	3.38	102	16, 27	H	4, 16
AGC 322050	22 13 06.30	+01 16 26.47	0.1844	3.46	373	1		
IRAS 22116+0437	22 14 10.42	+04 52 26.29	0.1938	2.84	121	14	H	3
IRAS 22135+0043	22 16 02.70	+00 58 10.99	0.2120	3.52	52	38	A	6
IRAS 22491-1808	22 51 49.28	−17 52 24.10	0.0776	2.48	47	16, 27	H	12, 15
IRAS F23019+3405	23 04 21.20	+34 21 47.48	0.1080	2.19	57	15	H, Sy2	3
IRAS F23028+0725	23 05 19.88	+07 41 43.01	0.1494	3.36	219	15	L	3

Table B.1 (cont'd)

Common Name	RA (J2000)	Dec (J2000)	z	$\log L_{OH}$ ($L_\odot$)	ΔV (km s^{-1})	Ref.	Type	Type Ref.
IRAS 23050+0359	23 07 35.77	+04 16 02.21	0.0474	1.70	197	18	H	2
IRAS 23129+2548	23 15 21.40	+26 04 32.30	0.1789	3.34	376	15	L	3, 13
IRAS 23135+2516	23 16 00.70	+25 33 24.08	0.0273	0.89^{k}	52	16, 30	Sy2	2, 15
IRAS 23199+0122	23 22 31.61	+01 39 28.12	0.1357	2.44	139	15	Sy2	3
IRAS 23234+0946	23 25 56.14	+10 02 49.49	0.1279	2.81	266	15	L	3, 13
IRAS 23327+2913	23 35 11.90	+29 30 00.00	0.1070	2.05	204	18	L	16
IRAS 23365+3604	23 39 01.27	+36 21 08.60	0.0645	2.53	256	18	C, L	2, 15

[k] kilomaser

[n] No OH spectrum exists in literature

[e] Line width is visually estimated from published spectrum

Note. — Spectral type classifications: S1 – Seyfert 1; S2 – Seyfert 2; L – LINER; H – HII region; A – AGN; and C – composite AGN and starburst

References. — OH detections and measurements were obtained from (1) This work; (2) Baan et al. 1982; (3) Baan 1985; (4) Baan 1989; (5) Baan et al. 1992b; (6) Baan et al. 1992a; (7) Baan et al. 1998; (8) Bottinelli et al. 1985a; (9) Bottinelli et al. 1985b; (10) Bottinelli et al. 1986; (11) Bottinelli et al. 1987; (12) Bottinelli et al. 1989; (13) Bottinelli et al. 1990; (14) Darling & Giovanelli 2000; (15) Darling & Giovanelli 2001; (16) Darling & Giovanelli 2002a; (17) Dickey et al. 1990; (18) Fernandez et al. 2010; (19) Glowacki et al. 2022; (20) Gowardhan et al. 2018; (21) Haynes et al. 2018; (22) Henkel & Wilson 1990; (23) Hess et al. 2021; (24) Kandalian 1996; (25) Kazes et al. 1988; (26) Kazes et al. 1989; (27) Kazes & Baan 1991; (28) Martin et al. 1988; (29) Martin et al. 1989; (30) Mirabel & Sanders 1987; (31) Morganti et al. 2006; (32) Norris et al. 1989; (33) Staveley-Smith et al. 1986; (34) Staveley-Smith et al. 1987; (35) Staveley-Smith et al. 1989; (36) Staveley-Smith et al. 1992; (37) Suess et al. 2016; (38) Willett 2012. Spectral classifications were obtained from (1) Almeida et al. 2023; (2) Baan et al. 1998; (3) Darling & Giovanelli 2006; (4) Duc et al. 1997; (5) Frogel et al. 1989; (6) Glikman et al. 2018; (7) Hekatelyne et al. 2020; (8) Kim & Sanders 1998; (9) Lee et al. 2011; (10) Samsonyan et al. 2016; (11) Sanders et al. 1988; (12) Smith et al. 1998; (13) Strauss & Huchra 1988; (14) Toba et al. 2014; (15) Veilleux et al. 1995; (16) Veilleux et al. 1999

Table B.2. IR properties of OHMs from IRAS catalog

Common Name	IRAS	$\log L_{\rm IR}$ ($L_\odot$)	$\log L_{\rm FIR}$ ($L_\odot$)	$f_{12\mu m}$ (Jy)	$f_{25\mu m}$ (Jy)	$f_{60\mu m}$ (Jy)	$f_{100\mu m}$ (Jy)
IRAS 00057+4021	00057+4021	≤11.68	11.41±0.33	≤0.25	0.38±0.04	4.58±0.46	4.82±0.48
IRAS 00335-2732	00335−2732	≤12.08	11.75±0.36	≤0.25	0.73±0.14	4.42±0.53	3.17±0.35
IRAS 00461-0728	00461−0728	≤12.98	12.18±0.32	≤0.45	≤0.55	0.63±0.08	0.95±0.13
UGC 00545	00509+1225	11.93±0.23	11.35±0.34	0.52±0.05	1.25±0.14	2.17±0.26	2.53±0.25
IRAS 01298-0744	01298−0744	≤12.58	12.15±0.35	≤0.39	≤0.45	2.50±0.33	2.23±0.24
IRAS 01355-1814	01355−1814	≤12.68	12.24±0.33	≤0.25	≤0.25	1.33±0.15	1.57±0.16
IRAS 01364-1042	01364−1042	≤11.88	11.64±0.34	≤0.25	0.41±0.06	6.74±0.81	6.59±0.79
III Zw 035	01417+1651	≤11.66	11.43±0.33	≤0.25	1.07±0.12	13.30±1.73	13.80±1.93
IRAS F01472+2347	01472+2347	≤12.31	≤11.86	≤0.10	≤0.09	0.30±0.05	≤1.06
IRAS 01562+2527	01562+2527	≤12.48	11.99±0.31	≤0.25	≤0.25	0.80±0.06	1.85±0.15
IRAS 01569-2939	01569−2939	≤12.43	12.03±0.35	≤0.25	≤0.25	1.92±0.19	1.21±0.14
IRAS 02483+4302	02483+4302	≤11.84	11.59±0.32	≤0.25	≤0.25	4.45±0.40	7.47±0.60
IRAS 02524+2046	02524+2046	≤12.56	≤12.34	≤0.06	≤0.08	0.96±0.08	≤4.79
UGC 02553	03056+2034	≤11.30	10.99±0.31	≤0.25	0.76±0.09	4.20±0.42	6.38±0.77
IRAS 03158+4227	03158+4227	≤12.69	12.40±0.34	≤0.25	0.48±0.04	4.39±0.40	4.62±0.37
IRAS 03260-1422	03260−1422	≤11.58	11.30±0.32	≤0.25	≤0.25	3.42±0.31	5.03±0.45
IRAS 03521+0028	03521+0028	≤12.65	12.34±0.32	≤0.25	0.23±0.03	2.64±0.24	3.83±0.34

Table B.2 (cont'd)

Common Name	IRAS	$\log L_{\rm IR}$ ($L_\odot$)	$\log L_{\rm FIR}$ ($L_\odot$)	$f_{12\mu\rm m}$ (Jy)	$f_{25\mu\rm m}$ (Jy)	$f_{60\mu\rm m}$ (Jy)	$f_{100\mu\rm m}$ (Jy)
IRAS 03566+1647	03566+1647	≤12.41	≤11.79	≤0.42	≤0.40	0.80±0.06	≤1.85
IRAS 04121+0223	04121+0223	≤12.22	11.71±0.31	≤0.28	≤0.25	0.93±0.06	1.62±0.13
UGC 03097	04332+0209	10.51±0.24	10.14±0.34	0.22±0.02	0.99±0.08	3.66±0.33	3.94±0.32
ESO 203-IG 001	04454−4838	≤11.92	11.66±0.34	≤0.25	0.47±0.03	5.93±0.47	5.39±0.43
IRAS 05100-2425	05100−2425	≤11.41	11.13±0.33	≤0.25	0.34±0.03	4.16±0.29	5.08±0.36
UGC 03351	05414+5840	11.27±0.26	11.04±0.31	0.56±0.09	0.81±0.07	14.20±1.28	30.30±3.64
IRAS 06206-3646	06206−3646	≤12.26	11.91±0.34	≤0.25	≤0.25	2.21±0.20	2.51±0.20
IRAS 06487+2208	06487+2208	≤12.55	12.15±0.32	≤0.25	≤0.52	2.07±0.17	2.36±0.26
IRAS 07163+0817	07163+0817	≤12.10	11.58±0.33	≤0.25	≤0.27	0.89±0.09	1.37±0.11
IRAS F07556+2859	07556+2859	≤12.03	11.54±0.31	≤0.14	≤0.22	0.62±0.05	0.93±0.18
IRAS 07572+0533	07572+0533	≤12.61	12.10±0.31	≤0.25	≤0.26	0.95±0.08	1.30±0.20
IRAS 08071+0509	08071+0509	≤11.87	11.61±0.32	≤0.25	0.41±0.06	4.77±0.57	6.78±0.88
IRAS 08201+2801	08201+2801	≤12.53	12.06±0.31	≤0.25	≤0.25	1.13±0.09	1.60±0.18
IRAS 08279+0956	08279+0956	≤12.46	≤12.06	≤0.08	≤0.19	0.59±0.06	≤1.26
IRAS 08449+2332	08449+2332	≤12.24	11.85±0.31	≤0.13	≤0.15	0.87±0.07	1.20±0.17
IRAS 08474+1813	08474+1813	≤12.45	11.98±0.33	≤0.25	≤0.40	1.36±0.12	1.65±0.13
IRAS 09039+0503	09039+0503	≤12.34	11.91±0.31	≤0.25	≤0.37	1.47±0.13	2.26±0.23

Table B.2 (cont'd)

Common Name	IRAS	$\log L_{\rm IR}$ ($L_\odot$)	$\log L_{\rm FIR}$ ($L_\odot$)	$f_{12\mu m}$ (Jy)	$f_{25\mu m}$ (Jy)	$f_{60\mu m}$ (Jy)	$f_{100\mu m}$ (Jy)
IRAS 09531+1430	09531+1430	≤12.57	12.13±0.31	≤0.14	≤0.17	0.78±0.06	1.04±0.14
IRAS 09539+0857	09539+0857	≤12.31	11.85±0.32	≤0.25	≤0.33	1.39±0.12	1.33±0.19
ESO 374-IG 032	10039−3338	11.73±0.27	11.46±0.33	0.29±0.03	1.17±0.10	9.20±0.92	8.81±0.97
IRAS 10036+2740	10035+2740	≤12.52	12.05±0.32	≤0.25	≤0.29	1.19±0.13	1.49±0.21
IRAS 10173+0828	10173+0829	≤11.86	11.60±0.34	≤0.25	0.53±0.08	5.95±0.59	5.68±0.57
IRAS 10339+1548	10339+1548	≤12.68	12.17±0.32	≤0.25	≤0.33	0.99±0.09	1.47±0.12
IRAS 10378+1109	10378+1109	≤12.47	12.09±0.35	≤0.25	≤0.34	2.21±0.24	1.84±0.18
IRAS 10485-1447	10485−1447	≤12.30	11.97±0.32	≤0.11	≤0.30	1.73±0.23	1.66±0.30
IRAS 10597+5926	10597+5926	≤12.34	11.84±0.31	≤0.25	≤0.29	1.02±0.08	1.33±0.17
ARP 148	11011+4107	≤11.61	11.38±0.32	≤0.25	0.38±0.05	6.06±0.61	10.70±0.96
IRAS 11029+3130	11028+3130	≤12.67	12.18±0.33	≤0.25	≤0.25	1.04±0.09	1.38±0.11
IRAS 11069+2711	11069+2711	≤11.91	11.58±0.31	≤0.25	≤0.25	2.14±0.19	4.18±0.42
IRAS 11180+1623	11180+1623	≤12.61	12.06±0.32	≤0.40	≤0.29	1.20±0.13	1.49±0.19
NGC 3690	11257+5850	11.79±0.29	11.49±0.34	3.71±0.19	21.50±1.07	106.00±10.60	111.00±8.88
ESO 320-G 030	11506−3851	11.27±0.30	11.05±0.33	0.57±0.04	2.29±0.16	34.20±4.45	44.50±5.34
IRAS 11524+1058	11524+1058	≤12.61	11.95±0.31	≤0.39	≤0.29	0.73±0.07	1.17±0.13
IRAS 12005+0009	12005+0009	≤12.20	11.56±0.32	≤0.29	≤0.36	0.74±0.15	0.93±0.20

Table B.2 (cont'd)

Common Name	IRAS	$\log\mathrm{L}_{\mathrm{IR}}$ ($\mathrm{L}_\odot$)	$\log\mathrm{L}_{\mathrm{FIR}}$ ($\mathrm{L}_\odot$)	$f_{12\mu\mathrm{m}}$ (Jy)	$f_{25\mu\mathrm{m}}$ (Jy)	$f_{60\mu\mathrm{m}}$ (Jy)	$f_{100\mu\mathrm{m}}$ (Jy)
IRAS 12018+1941	12018+1941	≤12.60	12.20±0.33	≤0.25	0.27±0.06	1.64±0.18	1.86±0.22
IRAS 12032+1707	12032+1707	≤12.86	12.37±0.34	≤0.25	≤0.49	1.43±0.17	1.48±0.16
IRAS 12071-0444	12071−0444	≤12.48	12.10±0.35	≤0.25	0.53±0.08	2.58±0.31	2.19±0.22
IRAS F12072+3054	12072+3054	≤11.96	≤11.39	≤0.06	≤0.14	0.23±0.04	≤0.35
IRAS 12112+0305	12112+0305	≤12.37	12.13±0.32	≤0.25	0.63±0.07	8.36±0.92	9.91±1.19
IRAS 12162+1047	12162+1047	≤12.16	≤11.73	≤0.11	≤0.19	0.72±0.06	≤0.95
NGC 4355	12243−0036	11.07±0.29	10.76±0.34	0.94±0.07	9.57±0.77	43.90±6.58	33.80±6.08
MRK 0231	12540+5708	12.56±0.27	12.21±0.34	1.81±0.09	8.52±0.51	33.60±3.36	30.90±3.40
IRAS 12548+2403	12549+2403	≤12.30	11.67±0.31	≤0.37	≤0.25	0.77±0.08	1.11±0.27
IRAS 13126+2452	13126+2453	≤10.99	10.77±0.32	≤0.25	1.27±0.11	17.60±1.94	18.70±2.43
IRAS F13218+0552	13218+0552	12.73±0.24	12.17±0.31	0.26±0.04	0.40±0.09	1.17±0.08	0.71±0.14
IRAS 13254+4754	13254+4754	≤11.70	11.34±0.31	≤0.25	≤0.25	1.81±0.18	2.75±0.33
MRK 0273	13428+5608	≤12.19	11.96±0.33	≤0.31	2.33±0.14	23.70±2.37	22.30±2.45
IRAS 13451+1232	13451+1232	≤12.41	11.97±0.31	≤0.25	0.67±0.08	2.01±0.24	2.14±0.41
IRAS F14014+3009	14014+3009	≤12.07	11.62±0.31	≤0.07	≤0.09	0.29±0.04	0.70±0.14
IRAS 14043+0624	14043+0624	≤12.12	11.58±0.31	≤0.27	≤0.26	0.80±0.08	1.43±0.16
IRAS 14059+2000	14059+2000	≤12.25	11.75±0.31	≤0.25	≤0.35	0.94±0.10	1.82±0.18

Table B.2 (cont'd)

Common Name	IRAS	$\log L_{\rm IR}$ ($L_\odot$)	$\log L_{\rm FIR}$ ($L_\odot$)	$f_{12\mu{\rm m}}$ (Jy)	$f_{25\mu{\rm m}}$ (Jy)	$f_{60\mu{\rm m}}$ (Jy)	$f_{100\mu{\rm m}}$ (Jy)
IRAS 14070+0525	14070+0525	≤13.02	12.58±0.33	≤0.25	≤0.31	1.43±0.14	1.72±0.15
IRAS 14531+0636	14531+0636	≤12.40	12.00±0.31	≤0.07	≤0.11	0.49±0.04	0.68±0.14
IRAS 14553+1245	14553+1245	≤12.19	11.67±0.31	≤0.25	≤0.25	0.93±0.07	1.10±0.12
IRAS 14586+1431	14586+1431	≤12.30	11.69±0.32	≤0.25	≤0.25	0.61±0.08	0.97±0.11
NGC 5861	15065−1107	10.39±0.25	10.14±0.31	0.43±0.06	1.16±0.09	10.40±0.94	20.80±2.50
CGCG 049-057	15107+0724	≤11.23	11.04±0.32	≤0.25	0.81±0.07	21.60±2.38	31.40±3.77
IRAS 15179+3956	15179+3956	≤11.73	11.39±0.35	≤0.25	0.80±0.08	4.26±0.38	3.08±0.28
IRAS 15224+1033	15224+1033	≤11.97	11.62±0.31	≤0.07	≤0.12	0.74±0.07	0.72±0.15
IRAS 15233+0533	15233+0533	≤11.78	11.47±0.34	≤0.25	0.36±0.06	3.60±0.36	3.73±0.34
IRAS 15250+3609	15250+3609	≤12.08	11.78±0.35	≤0.25	1.32±0.09	7.50±0.68	5.86±0.53
IRAS 15247-0945	15247−0945	≤11.61	11.35±0.32	≤0.25	0.38±0.06	4.68±0.42	6.38±0.57
Arp 220	15327+2340	12.18±0.32	11.97±0.34	0.47±0.03	8.11±0.41	104.00±8.32	118.00±7.08
AGC 257959	15533+1447	≤12.64	12.09±0.31	≤0.25	≤0.25	0.74±0.06	1.19±0.15
IRAS 15587+1609	15587+1609	≤12.05	11.65±0.31	≤0.12	≤0.10	0.74±0.05	0.82±0.21
IRAS 16090-0139	16090−0139	≤12.63	12.35±0.32	≤0.25	0.27±0.04	3.72±0.26	4.72±0.33
IRAS 16100+2528	16100+2527	≤12.02	≤11.69	≤0.08	≤0.08	0.71±0.05	≤1.38
IRAS 16255+2801	16255+2801	≤12.42	11.77±0.31	≤0.50	≤0.25	0.90±0.07	1.46±0.13

Table B.2 (cont'd)

Common Name	IRAS	$\log L_{\rm IR}$ ($L_\odot$)	$\log L_{\rm FIR}$ ($L_\odot$)	$f_{12\mu{\rm m}}$ (Jy)	$f_{25\mu{\rm m}}$ (Jy)	$f_{60\mu{\rm m}}$ (Jy)	$f_{100\mu{\rm m}}$ (Jy)
IRAS 16300+1558	16300+1558	≤12.96	12.56±0.33	≤0.25	≤0.27	1.63±0.13	2.05±0.14
IRAS 16399-0937	16399−0937	≤11.54	11.26±0.31	≤0.36	1.10±0.10	8.16±0.73	12.20±1.34
IRAS 17160+2006	17160+2006	≤11.78	≤11.49	≤0.04	≤0.10	0.63±0.04	≤1.37
IRAS 17208-0014	17208−0014	≤12.44	12.24±0.33	≤0.25	1.67±0.13	34.10±4.09	35.70±4.28
UGC 11035	17526+3253	≤11.19	10.91±0.31	≤0.25	0.34±0.04	3.44±0.21	7.07±0.49
IRAS 17540+2935	17539+2935	≤12.11	11.65±0.34	≤0.25	≤0.25	1.21±0.09	1.44±0.09
IRAS 18368+3549	18368+3549	≤12.37	12.04±0.31	≤0.25	≤0.25	2.23±0.13	3.83±0.27
IRAS 18544-3718	18544−3718	≤12.01	11.69±0.31	≤0.28	≤0.33	2.84±0.26	3.90±0.66
IRAS 18588+3517	18588+3517	≤12.17	11.79±0.33	≤0.25	0.19±0.02	1.80±0.14	1.75±0.16
IRAS 20100-4156	20100−4156	≤12.71	12.45±0.34	≤0.25	0.42±0.15	5.43±0.54	5.20±0.47
IRAS 20248+1734	20248+1734	≤12.22	11.75±0.32	≤0.25	≤0.25	0.74±0.08	2.53±0.38
IRAS 20286+1846	20286+1846	≤12.33	11.87±0.31	≤0.25	≤0.25	0.93±0.07	2.24±0.16
IRAS 20450+2140	20450+2140	≤12.24	11.73±0.31	≤0.25	≤0.25	0.72±0.05	1.90±0.15
UGC 11643	20491+1846	≤11.23	10.95±0.31	≤0.26	0.24±0.03	2.81±0.23	6.56±0.53
II Zw 096	20550+1656	11.93±0.26	11.65±0.34	0.29±0.06	2.32±0.14	13.40±1.21	11.90±1.19
IRAS 21077+3358	21077+3358	≤12.63	≤12.04	≤0.39	≤0.25	0.89±0.09	≤1.55
IRAS 21272+2514	21272+2514	≤12.51	≤11.95	≤0.36	≤0.39	1.08±0.12	≤1.63

Table B.2 (cont'd)

Common Name	IRAS	$\log L_{\mathrm{IR}}$ ($L_\odot$)	$\log L_{\mathrm{FIR}}$ ($L_\odot$)	$f_{12\mu\mathrm{m}}$ (Jy)	$f_{25\mu\mathrm{m}}$ (Jy)	$f_{60\mu\mathrm{m}}$ (Jy)	$f_{100\mu\mathrm{m}}$ (Jy)
UGC 11898	22025+4204	≤ 11.00	10.78 ± 0.31	≤ 0.25	0.72 ± 0.08	9.72 ± 1.17	14.50 ± 2.46
IRAS 22055+3024	22055+3024	≤ 12.40	12.00 ± 0.36	≤ 0.31	≤ 0.25	1.87 ± 0.35	2.32 ± 0.23
IRAS F22088-1831W	22088−1831	≤ 12.64	12.24 ± 0.35	≤ 0.25	≤ 0.31	1.88 ± 0.21	1.74 ± 0.16
AGC 322050	22105+0101	≤ 12.45	12.10 ± 0.31	≤ 0.13	≤ 0.11	0.99 ± 0.08	1.45 ± 0.20
IRAS 22116+0437	22116+0437	≤ 12.49	≤ 12.08	≤ 0.09	≤ 0.31	0.92 ± 0.07	≤ 1.03
IRAS 22135+0043	22135+0043	≤ 12.44	≤ 11.99	≤ 0.12	≤ 0.12	0.49 ± 0.05	≤ 1.01
IRAS 22491-1808	22491−1808	≤ 12.24	11.97 ± 0.34	≤ 0.25	0.57 ± 0.07	5.54 ± 0.67	4.64 ± 0.56
IRAS F23019+3405	23019+3405	≤ 12.03	11.75 ± 0.31	≤ 0.07	0.16 ± 0.03	1.42 ± 0.10	2.11 ± 0.38
IRAS F23028+0725	23028+0725	≤ 12.26	≤ 11.87	≤ 0.09	≤ 0.29	0.91 ± 0.10	≤ 1.37
IRAS 23050+0359	23050+0359	≤ 11.71	11.40 ± 0.32	≤ 0.25	0.53 ± 0.07	3.66 ± 0.44	5.01 ± 0.60
IRAS 23129+2548	23129+2548	≤ 12.67	12.27 ± 0.34	≤ 0.25	≤ 0.25	1.80 ± 0.20	1.70 ± 0.17
IRAS 23135+2516	23135+2517	11.60 ± 0.26	11.32 ± 0.32	0.31 ± 0.03	1.72 ± 0.17	9.63 ± 1.16	12.10 ± 1.57
IRAS 23199+0122	23199+0123	≤ 12.27	11.67 ± 0.31	≤ 0.25	≤ 0.35	0.71 ± 0.08	1.05 ± 0.15
IRAS 23234+0946	23234+0946	≤ 12.36	11.97 ± 0.33	≤ 0.25	≤ 0.28	1.65 ± 0.17	2.26 ± 0.20
IRAS 23327+2913	23327+2913	≤ 12.26	11.88 ± 0.34	≤ 0.25	≤ 0.34	2.08 ± 0.21	2.59 ± 0.21
IRAS 23365+3604	23365+3604	≤ 12.22	11.97 ± 0.33	≤ 0.25	0.81 ± 0.08	7.69 ± 0.85	8.19 ± 0.90

Table B.3. Near- to mid-IR properties of OHM from AllWISE

Common Name	WISE Designation	$\alpha_{\rm WISE}$	$f_{\rm W1}$ (mJy)	$f_{\rm W2}$ (mJy)	$f_{\rm W3}$ (mJy)	$f_{\rm W4}$ (mJy)
IRAS 00057+4021	J000820.63+403755.4	-2.6	2.49±0.08	1.72±0.05	17.88±0.36	262.51±6.04
IRAS 00335-2732	J003600.37−271533.8	-2.8	3.36±0.07	5.28±0.11	73.87±1.02	581.78±7.49
AGC 102299	J003924.69+260414.4	-1.1	0.45±0.01	0.38±0.01	1.46±0.13	. . .
IRAS 00461-0728	J004839.49−071221.4	-2.0	0.27±0.01	0.38±0.02	3.34±0.17	10.65±1.21
UGC 00545	J005334.93+124135.9	-1.2	87.93±1.86	129.10±2.26	387.35±4.99	939.44±18.15
AGC 116345	J011604.02+110136.6	-1.2	0.61±0.02	0.55±0.02	2.29±0.18	5.31±1.07
IRAS 01298-0744	J013221.41−072908.3	-2.8	0.62±0.02	1.57±0.03	27.23±0.45	110.84±2.45
IRAS 01355-1814	J013757.45−175921.0	-2.6	0.40±0.01	0.70±0.02	8.41±0.21	51.78±1.95
IRAS 01364-1042	J013852.86−102711.7	-2.3	2.70±0.06	3.37±0.07	24.60±0.41	205.50±4.92
III Zw 035	J014430.54+170608.5	-2.4	7.58±0.16	7.50±0.14	65.42±0.90	636.95±9.96
IRAS F01472+2347	J015001.56+240236.0	-1.6	0.61±0.02	0.62±0.02	3.75±0.16	9.05±0.80
IRAS 01562+2527	J015902.53+254236.4	-1.5	0.82±0.02	0.69±0.02	4.28±0.19	. . .
IRAS 01569-2939	J015913.78−292435.0	-2.6	0.86±0.02	1.13±0.03	16.48±0.30	91.85±2.37
AGC 181310	J022657.66+282457.4	-1.1	1.29±0.03	1.58±0.04	5.25±0.17	10.04±1.08
IRAS 02483+4302	J025135.89+431511.4	-1.3	9.83±0.53	5.28±0.10	17.92±0.36	102.79±2.55
IRAS 02524+2046	J025517.10+205857.2	-1.9	0.60±0.02	0.76±0.02	6.00±0.24	20.14±1.46
UGC 02553	J030830.71+204620.2	-2.4	8.73±0.18	7.05±0.14	86.23±1.27	556.51±9.73

Table B.3 (cont'd)

Common Name	WISE Designation	$\alpha_{\rm WISE}$	$f_{\rm W1}$ (mJy)	$f_{\rm W2}$ (mJy)	$f_{\rm W3}$ (mJy)	$f_{\rm W4}$ (mJy)
IRAS 03158+4227	J031912.54+423828.7	-2.1	1.85±0.05	0.98±0.03	...	...
IRAS 03260-1422	J032824.34−141206.8	-1.8	2.86±0.06	2.11±0.04	12.92±0.32	72.87±2.15
Nkalakatha	J033046.26−275518.3	-2.1	0.12±0.00	0.08±0.01	0.90±0.08	4.16±0.65
IRAS 03521+0028	J035442.21+003703.2	-2.4	0.99±0.09	1.07±0.03	11.87±0.31	77.57±2.21
IRAS 03566+1647	J035928.48+165624.7	-2.1	4.02±0.08	11.10±0.21	65.79±0.91	229.09±4.64
IRAS 04121+0223	J041447.21+023038.7	-2.0	0.50±0.02	0.42±0.03	3.77±0.27	15.83±2.11
UGC 03097	J043548.46+021529.6	-2.5	5.97±0.13	13.68±0.25	120.25±1.66	697.90±14.13
ESO 203-IG 001	J044649.52−483330.1	-2.8	1.70±0.08	2.71±0.05	38.89±0.54	272.94±4.77
IRAS 05100-2425	J051209.18−242156.1	-1.9	6.05±0.13	4.55±0.09	31.05±0.46	178.33±4.76
UGC 03351	J054548.01+584203.5	-1.5	45.32±0.92	38.27±0.70	291.24±3.48	588.98±9.75
IRAS 06206-3646	J062222.59−364745.0	-2.1	1.20±0.03	1.32±0.03	8.20±0.18	59.86±1.87
IRAS 06487+2208	J065145.73+220427.3	-2.5	1.89±0.04	3.34±0.07	35.54±0.56	185.81±3.76
IRAS 07163+0817	J071905.48+081206.3	-2.1	0.74±0.02	0.70±0.02	7.22±0.22	29.35±1.48
IRAS F07556+2859	J075845.95+285132.7	-1.8	0.75±0.02	0.71±0.02	7.58±0.21	15.80±1.37
IRAS 07572+0533	J075959.76+052452.0	-2.4	1.29±0.03	2.00±0.04	19.83±0.36	109.37±3.02
IRAS 08071+0509	J080947.23+050108.8	-2.2	7.00±0.14	6.21±0.12	72.95±1.07	318.02±7.02
IRAS 08201+2801	J082312.60+275139.9	-2.7	0.64±0.02	0.87±0.02	13.71±0.32	81.43±2.32

Table B.3 (cont'd)

Common Name	WISE Designation	$\alpha_{\rm WISE}$	$f_{\rm W1}$ (mJy)	$f_{\rm W2}$ (mJy)	$f_{\rm W3}$ (mJy)	$f_{\rm W4}$ (mJy)
IRAS 08279+0956	J083039.35+094636.5	-2.0	0.43±0.01	0.44±0.02	3.33±0.25	15.43±1.45
IRAS 08449+2332	J084750.22+232109.9	-1.9	1.82±0.04	1.73±0.04	13.17±0.30	48.54±2.46
IRAS 08474+1813	J085018.33+180201.0	-2.3	0.41±0.01	0.52±0.02	3.97±0.20	28.33±2.24
IRAS 09039+0503	J090634.03+045127.6	-2.0	1.22±0.03	1.25±0.03	11.59±0.26	41.56±1.76
AGC 193884	J093238.29+161157.4	-1.1	1.15±0.03	1.00±0.03	2.46±0.17	9.39±1.28
IRAS 09531+1430	J095549.90+141606.8	-0.6	0.58±0.02	0.46±0.02	1.08±0.18	...
IRAS 09539+0857	J095634.32+084306.3	-2.4	0.63±0.02	0.92±0.03	13.34±0.28	47.52±2.01
ESO 374-IG 032	J100604.61−335305.6	-1.6	19.99±0.42	114.56±2.00	242.39±3.12	695.00±12.79
IRAS 10036+2740	J100626.34+272546.0	-1.6	1.15±0.03	1.09±0.03	5.06±0.17	23.18±1.32
IRAS 10173+0828	J102000.23+081333.7	-2.5	1.91±0.07	1.49±0.05	13.64±0.43	191.30±7.57
IRAS 10339+1548	J103637.97+153240.8	-2.1	0.72±0.02	0.64±0.02	5.04±0.20	29.41±1.49
IRAS 10378+1109	J104029.17+105318.1	-2.4	1.31±0.03	2.51±0.06	16.00±0.31	133.58±3.20
IRAS 10485-1447	J105103.07−150321.6	-2.4	0.91±0.03	1.82±0.04	14.55±0.31	91.13±3.10
IRAS 10597+5926	J110247.08+591036.2	-2.0	0.50±0.01	0.55±0.02	4.80±0.16	17.17±1.11
ARP 148	J110353.94+405100.1	-1.8	10.76±0.23	9.46±0.17	87.75±1.29	221.50±5.50
IRAS 11029+3130	J110537.51+311432.0	-2.2	0.26±0.01	0.23±0.01	2.18±0.12	12.85±1.04
IRAS 11069+2711	J110938.91+265456.1	-1.8	1.29±0.03	1.00±0.03	10.99±0.25	23.13±1.28

Table B.3 (cont'd)

Common Name	WISE Designation	$\alpha_{\rm WISE}$	$f_{\rm W1}$ (mJy)	$f_{\rm W2}$ (mJy)	$f_{\rm W3}$ (mJy)	$f_{\rm W4}$ (mJy)
AGC 219215	J111125.06+052045.9	-1.8	0.27±0.01	0.47±0.02	3.32±0.17	7.28±1.13
IRAS 11180+1623	J112041.75+160656.7	-2.3	0.53±0.01	0.61±0.02	7.10±0.21	34.45±1.52
NGC 3690	J112833.58+583346.4	-2.8	57.81±1.12	82.94±1.53	1041.08±14.37	10871.59±210.04
ESO 320-G 030	J115311.71−390748.9	-1.9	55.63±1.18	42.59±0.82	430.51±5.54	1541.63±24.11
IRAS 11524+1058	J115505.14+104123.7	-1.9	0.52±0.02	0.57±0.02	4.47±0.23	14.01±1.55
AGC 219828	J115514.70+313002.8	-1.2	0.49±0.01	0.35±0.01	...	...
IRAS 12005+0009	J120304.42−000727.4	-1.8	1.50±0.03	1.87±0.04	9.83±0.27	45.72±1.89
IRAS 12018+1941	J120424.54+192509.8	-3.0	1.05±0.02	2.20±0.05	38.17±0.60	254.55±5.39
IRAS 12032+1707	J120547.71+165107.9	-2.6	0.72±0.02	0.97±0.03	16.39±0.32	82.50±2.05
IRAS 12071-0444	J120945.11−050113.4	-2.3	4.65±0.10	8.85±0.17	70.06±1.10	388.99±8.95
IRAS F12072+3054	J120948.28+303749.5	-2.3	0.15±0.01	0.39±0.02	3.74±0.15	11.61±0.99
IRAS 12112+0305	J121345.99+024840.2	-2.4	3.83±0.08	4.46±0.09	51.20±0.80	297.92±6.03
AGC 229487	J121548.81+351059.5	-1.2	0.90±0.02	0.62±0.02	...	...
IRAS 12162+1047	J121847.76+103113.6	-2.0	0.73±0.02	0.81±0.02	7.00±0.21	25.98±1.63
NGC 4355	J122654.60−005239.2	-3.3	14.82±0.31	26.36±0.49	766.83±10.58	6119.12±67.56
MRK 0231	J125614.23+565225.3	-1.5	339.09±9.67	517.18±11.42	1659.84±15.27	6518.16±65.96
IRAS 12548+2403	J125719.99+234746.3	-1.5	1.17±0.03	0.96±0.03	4.88±0.25	16.13±1.97

Table B.3 (cont'd)

Common Name	WISE Designation	$\alpha_{\rm WISE}$	$f_{\rm W1}$ (mJy)	$f_{\rm W2}$ (mJy)	$f_{\rm W3}$ (mJy)	$f_{\rm W4}$ (mJy)
IRAS 13126+2452	J131503.50+243707.7	-2.2	12.48±0.25	7.85±0.14	48.04±0.71	722.42±15.29
IRAS F13218+0552	J132419.88+053704.7	-0.9	42.37±0.86	86.48±1.51	171.66±2.37	263.94±5.58
IRAS 13254+4754	J132732.69+473903.4	-2.0	2.61±0.06	2.23±0.05	18.07±0.30	84.64±2.49
MRK 0273	J134442.09+555313.2	-2.3	20.92±0.42	34.56±0.64	219.82±3.03	1571.03±23.13
IRAS 13451+1232	J134733.34+121724.2	-2.2	7.55±0.20	14.00±0.32	93.42±1.38	458.49±9.70
IRAS F14014+3009	J140340.36+295456.6	-1.6	0.36±0.01	0.34±0.01	2.30±0.14	6.03±0.92
IRAS 14043+0624	J140649.81+061036.0	-1.4	1.71±0.04	1.34±0.03	6.39±0.18	17.89±1.07
IRAS 14059+2000	J140818.72+194622.7	-1.4	2.11±0.05	2.58±0.05	8.91±0.20	28.49±1.21
IRAS 14070+0525	J140931.24+051131.6	-2.2	0.62±0.02	0.83±0.02	9.80±0.21	33.01±1.21
IRAS 14531+0636	J145537.38+062437.5	-2.1	0.46±0.01	0.57±0.02	4.87±0.17	19.34±1.12
IRAS 14553+1245	J145742.45+123321.0	-2.2	1.26±0.03	1.39±0.03	15.46±0.28	62.86±2.14
IRAS 14586+1431	J150101.96+141947.8	-2.0	0.24±0.01	0.13±0.01	...	...
NGC 5861	J150916.09−111918.0	-2.1	13.20±0.28	23.44±0.43	169.49±2.18	676.61±8.71
CGCG 049-057	J151313.09+071331.6	-2.0	11.75±0.24	8.71±0.16	65.93±0.91	457.24±6.31
IRAS 15179+3956	J151947.04+394535.5	-2.7	2.77±0.06	7.82±0.14	59.96±0.72	528.61±6.81
IRAS 15224+1033	J152451.22+102248.7	-2.2	0.65±0.02	1.12±0.03	10.86±0.24	37.77±1.32
IRAS 15233+0533	J152549.54+052248.4	-2.3	4.11±0.08	3.64±0.07	35.73±0.49	273.89±5.04

Table B.3 (cont'd)

Common Name	WISE Designation	$\alpha_{\rm WISE}$	$f_{\rm W1}$ (mJy)	$f_{\rm W2}$ (mJy)	$f_{\rm W3}$ (mJy)	$f_{\rm W4}$ (mJy)
IRAS 15250+3609	J152659.42+355837.5	-3.0	3.50±0.01	7.78±0.01	115.71±0.10	906.52±1.01
IRAS 15247-0945	J152727.62−095542.3	-1.6	4.89±0.11	3.17±0.07	18.74±0.38	78.49±2.67
Arp 220	J153457.24+233011.4	-2.8	28.35±0.57	31.57±0.55	427.27±5.90	4588.07±33.77
AGC 257959	J155537.95+143905.3	-2.0	0.33±0.01	0.66±0.02	5.51±0.17	13.28±1.11
IRAS 15587+1609	J160102.79+160103.4	-1.9	0.86±0.02	1.01±0.03	6.81±0.20	24.60±1.18
IRAS 16090-0139	J161140.42−014706.2	-2.4	1.86±0.04	4.35±0.09	36.69±0.61	166.51±4.29
IRAS 16100+2528	J161205.40+252023.2	-2.3	0.42±0.01	0.37±0.01	4.55±0.16	25.17±1.34
IRAS 16255+2801	J162733.79+275431.9	-3.0	0.09±0.00	0.04±0.01	...	...
IRAS 16300+1558	J163221.41+155145.6	-2.0	1.04±0.02	1.50±0.03	11.76±0.28	36.41±1.54
IRAS 16399-0937	J164240.11−094314.8	-2.1	19.29±0.37	17.23±0.30	183.40±2.53	826.10±16.72
IRAS 17160+2006	J171814.38+200308.3	-1.8	1.14±0.03	0.66±0.02	...	...
IRAS 17208-0014	J172321.98−001700.6	-2.3	13.95±0.35	15.17±0.35	148.89±2.19	839.04±21.61
UGC 11035	J175429.47+325313.7	-1.6	9.90±0.24	8.10±0.16	68.76±1.08	125.45±3.23
IRAS 17540+2935	J175556.10+293526.3	-2.1	2.14±0.05	2.15±0.05	17.49±0.32	98.97±2.73
IRAS 18368+3549	J183835.40+355220.1	-1.7	2.57±0.05	2.42±0.05	18.50±0.32	50.61±1.63
IRAS 18544-3718	J185752.61−371440.0	-2.3	1.74±0.04	9.17±0.17	55.92±0.93	157.26±3.62
IRAS 18588+3517	J190041.14+352126.0	-2.3	1.39±0.03	2.44±0.05	23.94±0.37	95.78±2.03

Table B.3 (cont'd)

Common Name	WISE Designation	$\alpha_{\rm WISE}$	$f_{\rm W1}$ (mJy)	$f_{\rm W2}$ (mJy)	$f_{\rm W3}$ (mJy)	$f_{\rm W4}$ (mJy)
IRAS 20100-4156	J201329.54−414734.8	-2.5	1.94±0.04	4.35±0.08	39.20±0.61	244.82±4.50
IRAS 20248+1734	J202708.10+174421.9	-2.3	0.88±0.02	1.09±0.03	12.27±0.27	58.45±1.83
IRAS 20286+1846	J203054.45+185637.1	-2.0	0.67±0.02	0.67±0.02	5.74±0.22	22.26±1.62
IRAS 20450+2140	J204714.32+215112.1	-1.8	1.64±0.05	1.39±0.04	12.05±0.33	34.37±2.21
UGC 11643	J205125.89+185804.1	-1.6	16.91±0.36	11.97±0.22	114.93±1.48	202.15±4.09
II Zw 096	J205724.31+170738.3	-2.9	8.50±0.18	11.87±0.22	210.12±2.71	1740.80±20.82
IRAS 21077+3358	J210947.82+341028.6	-2.1	0.70±0.02	0.37±0.01	...	...
IRAS 21272+2514	J212929.41+252754.5	-2.2	0.71±0.02	0.94±0.02	7.90±0.23	40.07±1.44
UGC 11898	J220436.00+421939.5	-1.9	18.56±0.39	14.19±0.26	110.00±1.52	555.65±9.71
IRAS 22055+3024	J220749.67+303939.8	-2.6	1.24±0.03	1.86±0.04	20.62±0.30	139.18±3.20
IRAS F22088-1831W	J221133.81−181706.3	-2.5	0.80±0.02	0.79±0.02	9.43±0.24	64.38±2.07
AGC 322050	J221306.32+011626.9	-2.2	0.35±0.01	0.40±0.02	3.66±0.18	17.50±1.45
IRAS 22116+0437	J221410.41+045226.0	-2.6	0.68±0.02	0.99±0.03	18.55±0.36	69.92±1.93
IRAS 22135+0043	J221602.69+005811.0	-1.8	0.65±0.02	1.73±0.04	7.22±0.24	22.27±1.31
IRAS 22491-1808	J225149.29−175223.8	-2.7	2.63±0.06	2.31±0.05	38.08±0.56	349.76±5.79
IRAS F23019+3405	J230421.22+342147.6	-2.1	2.73±0.06	2.94±0.06	28.32±0.42	108.95±3.01
IRAS F23028+0725	J230519.90+074143.1	-2.9	0.77±0.05	0.93±0.03	16.04±0.32	150.52±3.46

Table B.3 (cont'd)

Common Name	WISE Designation	α_{WISE}	f_{W1} (mJy)	f_{W2} (mJy)	f_{W3} (mJy)	f_{W4} (mJy)
IRAS 23050+0359	J230735.77+041602.1	-2.2	7.15±0.15	5.67±0.11	57.97±0.85	321.02±6.50
IRAS 23129+2548	J231521.40+260432.3	-2.6	0.65±0.02	0.71±0.02	13.55±0.27	61.75±1.82
IRAS 23135+2516	J231600.68+253324.1	-2.2	19.74±0.40	35.39±0.65	221.27±2.85	1245.36±25.21
IRAS 23199+0122	J232231.62+013927.7	-1.7	1.47±0.04	1.56±0.05	12.98±0.50	26.91±2.97
IRAS 23234+0946	J232556.12+100249.4	-2.2	1.05±0.03	1.42±0.05	12.17±0.37	63.14±3.54
IRAS 23327+2913	J233511.92+293000.4	-2.3	2.31±0.05	2.81±0.06	21.48±0.36	168.91±3.42
IRAS 23365+3604	J233901.29+362108.4	-2.6	5.00±0.12	5.85±0.12	67.47±0.99	541.44±10.46

Table B.4. Radio properties of OHMs from FIRST and NVSS

Common Name	NVSS	$f_{\rm NVSS}$ (mJy)	FIRST	$f_{\rm FIRST}$ (mJy)
IRAS 00057+4021	000820+403755	6.9±0.4	...	...
IRAS 00335-2732	003600−271534	11.3±0.6	...	...
IRAS 00461-0728	004839−071222	4.9±0.5	J004839.5−071221	3.61±0.18
UGC 00545	005334+124133	8.3±0.5	J005334.9+124135	5.30±0.15
IRAS 01298-0744	013220−072920	4.1±0.6	J013221.4−072908	3.49±0.12
IRAS 01364-1042	013852−102711	15.8±0.7	J013852.8−102712	15.55±0.11
III Zw 035	014430+170608	40.1±1.3	...	...
IRAS 01562+2527	015903+254237	5.9±0.5	...	...
IRAS 01569-2939	015913−292435	123.5±3.7	...	...
IRAS 02483+4302	025134+431515	1224.9±36.7	...	...
IRAS 02524+2046	025517+205842	2.6±0.5	...	...
UGC 02553	030830+204620	17.1±1.0	...	...
IRAS 03260-1422	032824−141207	11.0±0.6	...	...
IRAS 03521+0028	035441+003704	6.1±0.5	J035442.2+003703	4.48±0.15
IRAS 03566+1647	035928+165613	3.2±0.4	...	...
IRAS 04121+0223	041447+023043	3.0±0.4	...	...
IRAS 05100-2425	051209−242156	19.9±0.8	...	...
IRAS 06206-3646	062222−364742	32.2±1.4	...	...
IRAS 06487+2208	065145+220427	10.3±0.5	...	...
IRAS 07163+0817	071905+081206	3.2±0.4	...	...
IRAS F07556+2859	075846+285129	3.5±0.4	J075845.9+285132	3.64±0.14
IRAS 07572+0533	080000+052509	11.0±1.1	...	...
IRAS 08071+0509	080947+050109	35.8±1.1	J080947.2+050109	33.77±0.16
IRAS 08201+2801	082313+275127	16.3±0.6	J082313.7+275120	10.66±0.14
IRAS 08279+0956	083039+094641	3.7±0.7[s]	J083039.3+094636	2.84±0.15
IRAS 08449+2332	084750+232111	5.8±0.5	J084750.2+232110	3.24±0.13

Table B.4 (cont'd)

Common Name	NVSS	$f_{\rm NVSS}$ (mJy)	FIRST	$f_{\rm FIRST}$ (mJy)
IRAS 08474+1813	085018+180156	3.8±0.5	J085018.3+180201	3.82±0.15
IRAS 09039+0503	090634+045125	6.2±0.5	J090634.0+045127	4.92±0.15
IRAS 09531+1430	095550+141558	2.5±0.4	J095550.2+141607	3.23±0.14
IRAS 09539+0857	095634+084303	8.5±1.0	J095634.3+084306	5.32±0.14
ESO 374-IG 032	100605−335317	23.4±1.5$^{\rm p}$	...	...
IRAS 10036+2740	100626+272543	5.8±0.5	J100626.3+272546	5.44±0.14
IRAS 10173+0828	102000+081335	9.9±0.9	J102000.1+081333	7.63±0.16
IRAS 10339+1548	103638+153239	4.7±0.5	J103637.9+153240	4.74±0.15
IRAS 10378+1109	104029+105320	8.4±0.5	J104029.1+105318	8.55±0.15
IRAS 10485-1447	105103−150321	4.1±0.6	...	...
IRAS 10597+5926	110246+591038	4.4±0.5	J110247.1+591036	4.43±0.15
ARP 148	110353+405059	36.4±1.2	J110353.9+405059	31.38±0.14
IRAS 11029+3130	...	...	J110537.5+311432	2.32±0.11
IRAS 11069+2711	110937+265514	23.3±0.8	J110938.8+265456	1.92±0.14
IRAS 11180+1623	112041+160703	4.2±0.5	J112041.1+160655	1.42±0.14
NGC 3690	112826+583418	9.2±0.5$^{\rm p}$	J112830.9+583340	83.49±0.15
ESO 320-G 030	115311−390748	109.4±3.9	...	...
IRAS 11524+1058	...	...	J115505.1+104122	2.59±0.14
IRAS 12005+0009	120304−000725	4.9±0.5	J120304.4−000727	3.64±0.14
IRAS 12018+1941	120424+192512	6.1±0.4	J120424.5+192509	5.55±0.14
IRAS 12032+1707	120547+165108	28.4±0.9	J120547.7+165108	29.31±0.15
IRAS 12071-0444	120944−050116	7.9±0.5	J120945.1−050113	7.86±0.14
IRAS 12112+0305	121345+024840	23.3±0.8	J121346.0+024841	24.64±0.14
IRAS 12162+1047	121847+103122	4.2±0.6	J121847.7+103114	1.96±0.15
MRK 0231	125614+565223	308.9±12.1$^{\rm s}$	J125614.2+565204	15.28±0.19
IRAS 12548+2403	125720+234750	3.6±0.4	J125720.0+234746	3.47±0.13

Table B.4 (cont'd)

Common Name	NVSS	$f_{\rm NVSS}$ (mJy)	FIRST	$f_{\rm FIRST}$ (mJy)
IRAS F13218+0552	132420+053709	4.9±0.5	J132419.9+053705	4.26±0.14
IRAS 13254+4754	132732+473906	7.3±0.4	J132732.7+473903	8.53±0.14
MRK 0273	134442+555313	144.7±5.1$^{\rm p}$	J134442.1+555313	132.02±0.13
IRAS 13451+1232	134733+121724	5397.2±161.9$^{\rm p}$	J134731.9+121630	13.09±0.85
IRAS 14043+0624	140649+061035	14.2±0.6	J140649.8+061036	12.27±0.15
IRAS 14059+2000	140818+194622	7.2±0.4	J140818.7+194622	7.45±0.14
IRAS 14070+0525	140931+051133	4.8±0.4	J140931.2+051131	5.53±0.14
IRAS 14553+1245	145742+123332	3.5±0.5	J145742.4+123321	3.06±0.15
IRAS 14586+1431	150102+142001	10.7±0.5	J150102.1+142002	11.19±0.15
CGCG 049-057	151313+071331	53.3±1.6	J151313.1+071331	55.00±0.14
IRAS 15179+3956	151946+394541	4.3±0.4	J151947.0+394535	4.25±0.14
IRAS 15224+1033	152451+102245	3.5±0.4	J152451.2+102249	3.66±0.15
IRAS 15233+0533	152549+052249	12.2±0.5	J152549.5+052248	13.14±0.14
IRAS 15250+3609	152659+355839	14.5±0.6	J152659.4+355837	13.06±0.14
IRAS 15247-0945	152727−095550	16.3±0.6	…	…
Arp 220	153457+233011	326.3±9.8	J153457.2+233011	316.13±0.14
IRAS 15587+1609	…	…	J160102.7+160103	1.06±0.15
IRAS 16090-0139	161140−014706	20.9±0.7	…	…
IRAS 16100+2528	…	…	J161205.4+252024	2.20±0.14
IRAS 16300+1558	163221+155147	7.5±0.5	J163221.4+155145	5.93±0.15
IRAS 16399-0937	164240−094315	54.7±1.7	…	…
IRAS 17160+2006	171816+200307	6.8±0.5	…	…
IRAS 17208-0014	172321−001702	81.8±2.5	…	…
IRAS 17540+2935	175555+293526	3.5±0.5	…	…
IRAS 18368+3549	183835+355220	20.6±0.7	…	…
IRAS 18544-3718	185754−371433	5.2±0.6	…	…

Table B.4 (cont'd)

Common Name	NVSS	f_{NVSS} (mJy)	FIRST	f_{FIRST} (mJy)
IRAS 18588+3517	190041+352125	5.6±0.4	...	...
IRAS 20450+2140	204714+215110	4.7±0.5	...	...
UGC 11643	205125+185805	23.4±1.1	...	...
II Zw 096	205724+170741	43.2±1.7	...	...
IRAS 21077+3358	210950+341031	8.7±0.9	...	...
IRAS 21272+2514	212929+252756	3.9±0.4	...	...
IRAS 22055+3024	220749+303942	6.0±0.5	...	...
IRAS F22088-1831W	221134−181704	6.2±0.5	...	...
IRAS 22116+0437	221410+045226	7.9±0.5	J221410.5+045225	0.98±0.13
IRAS 22135+0043	...	...	J221602.7+005810	1.31±0.13
IRAS 22491-1808	225149−175225	5.9±0.5	...	...
IRAS F23019+3405	230421+342149	7.3±0.5	...	...
IRAS F23028+0725	230520+074145	18.7±1.0	J230519.9+074143	14.91±0.14
IRAS 23050+0359	230735+041559	15.8±0.6	J230735.7+041601	12.31±0.08
IRAS 23129+2548	231521+260436	4.3±0.4	...	...
IRAS 23199+0122	232232+013926	2.9±0.4	J232231.7+013928	2.86±0.14
IRAS 23234+0946	232556+100248	10.9±0.9	...	...
IRAS 23327+2913	233511+293000	7.8±0.5	...	...
IRAS 23365+3604	233901+362109	27.2±0.9	...	...
IRAS F01472+2347	015001+240228	5.7±0.5	...	...
AGC 219215	...	...	J111125.0+052046	1.33±0.15
IRAS 14531+0636	145537+062438	3.1±0.4	J145537.3+062437	1.90±0.14
AGC 257959	155538+143907	3.2±0.5	J155537.9+143905	3.36±0.14
UGC 03097	043548+021534	3.9±0.5	...	...
UGC 03351	054548+584203	137.1±4.8	...	...
AGC 193884	093235+161219	183.0±6.3$^{\mathrm{s}}$	J093241.3+161135	18.49±0.13

Table B.4 (cont'd)

Common Name	NVSS	$f_{\rm NVSS}$ (mJy)	FIRST	$f_{\rm FIRST}$ (mJy)
NGC 4355	122654−005238	40.8±1.3	J122654.6−005239	41.19±0.14
IRAS 13126+2452	131503+243707	30.8±1.0	J131503.5+243707	32.33±0.13
IRAS F14014+3009	140341+295504	3.1±0.5	J140340.3+295456	2.40±0.14
NGC 5861	150916−111925	32.5±2.1	...	...
UGC 11035	175429+325312	45.3±1.7	...	...
IRAS 23135+2516	231600+253324	34.7±1.4	...	...
UGC 11898	220435+421940	34.8±1.4	...	...
IRAS 03158+4227	031912+423830	13.2±0.6	...	...
AGC 116345	011604+110141	6.0±0.5	J011603.9+110136	5.54±0.14
AGC 322050	221305+011641	6.4±1.1	J221306.3+011627	2.07±0.18

[p] From NVSS, peak flux density residual is high

[s] From NVSS, integrated flux density residual is high